Quantum correlations and light localization in disordered nanophotonic structures

Smolka, Stephan

Publication date:
2010

Document Version
Publisher's PDF, also known as Version of record

Quantum correlations and light localization in disordered nanophotonic structures

A dissertation
submitted to the Department of Photonics Engineering
at the Technical University of Denmark
in partial fulfillment of the requirements
for the degree of
philosophiæ doctor

Stephan Smolka

August 13, 2010

Kgs Lyngby, Denmark

Preface

This thesis presents work carried out in the Quantum Photonics Group under the supervision of associate professor Peter Lodahl at the Technical University of Denmark between July 2007 and August 2010. Part of the research was carried out during a six moth external research stay at the Institute for Atomic and Molecular Physics (AMOLF) in Amsterdam, the Netherlands. The work described in this thesis covers a broad range of multiple scattering experiments in the realm of quantum optics and can be naturally divided in two main topics; the experimental demonstration of spatial quantum correlations and light localization induced by multiple scattering in disordered nanophotonic structures.

When I started my Ph.D. studies, multiple scattering of light was not being actively studied at the institute. I am very thankful to my supervisor Peter Lodahl for introducing me into the topic, supporting me with very valuable discussions, ideas, and helping me to write scientific articles throughout my entire thesis. He, Allard P. Mosk and Ad Lagendijk proposed theoretically the existence of spatial quantum correlations which we demonstrated experimentally in the first part of this thesis. The studies on spatial quantum correlations have only been possible due to a very close collaboration with DTU Fysik. During that time we faced and solved many experimental challenges and I want especially thank my co-supervisor Ulrik L. Andersen and Alex for many motivating discussions. The samples for this experiments were provided from Elbert, Ivo, and Allard P. Mosk at the University Twente, the Netherlands, which I acknowledge gratefully.

Later in the project, I had the pleasure to visit the photon scattering group at AMOLF where I worked independently and could choose the focus of my research. This group has a large expertise on the fundamental properties of

multiple scattering media that helped me in furthering my project. In particular, I am very grateful to Prof. Ad Lagendijk and his group for their hospitality and many open discussions. My stay in Amsterdam was very stimulating and it was encouraging to experience this exiting research environment. I would like to thank Ramy, Sanli, Paolo, and Otto for a the insights of multiple scattering and many social events.

The last part of this thesis concerned the investigation of disordered photonic crystal waveguides. This would not have been possible without the fabrication of the samples carried out by Søren, which I would like to highlight and acknowledge. The good work environment among the many different people of the Quantum Photonics group involved in this project, allowed us to obtain good results. I would like to thank David for working together on the measurements of the localization length in passive photonic crystal waveguides. Luca and Henri for performing the experiments on quantum dots embedded in photonic crystal waveguides which have been used to investigate the statistical properties of Anderson localization. I would like to thank Peter Lodahl because he not only supervised us but also had many inspiring ideas that made the project on Anderson localization possible. With all people in the nano photonic cluster I had an uncountable number of interesting discussions about Anderson localization of light and I am very happy about that. I also appreciated the communication between experimentalists and theoreticians who always had an open door for me, in particular Johan and Philip. Both helped me to understand the theory behind the experiments and contributed to the calculations on spatial quantum correlations and the Green's function formalism. A special thank to Mads for a pleasant time while sharing the office, listen to my Danish attempts, and many good table soccer tournaments. Furthermore I would like to thank Serkan, Kristian, Jin, and Qin for the good atmosphere and collaboration.

I had a very pleasant time at DTU but also outside of my work environment, where Martin, Elaine, Alex, and Elizaveta became good friends of mine. Most importantly, I am grateful to Lena for the unique time in Denmark and the support, especially by distracting me from physics.

Stephan Smolka
August 2010

Abstract

This thesis reports results on quantum properties of light in multiple-scattering nano-structured materials.

Spatial quantum correlations of photons are demonstrated experimentally that are induced by multiple scattering of squeezed light and of purely quantum origin. By varying the quantum state of the light source, positive and negative spatial quantum correlations are observed. Angular-resolved measurements of multiply scattered photons show the infinite range of the correlation function in the diffusive regime. The multiply scattered light is characterized in frequency-resolved quantum noise measurements as well as in time-resolved photon-coincidence measurements and the experimental results are in excellent agreement with the quantum theory of multiple scattering. Probing the noise properties of light in the coherent backscattering cone reveals an enhancement factor of the multiply scattered photon fluctuations that is larger than the predicted enhancement of the backscattered light intensity. Characterizing the quantum properties of multiply scattered light forms the basis for studies of quantum interference and quantum entanglement in disordered media.

Anderson localization of light is demonstrated in disordered photonic crystal waveguides. Transmission measurements show that the localization length is strongly dispersive, allowing the control of one-dimensional Anderson localization of light. The statistical properties of Anderson localization are probed by embedding quantum dot light sources in disordered photonic crystal waveguides. From photoluminescence measurements, the spectral distribution of Anderson-localized modes is determined. Comparing the experimental data with one-dimensional analytical calculations provides a novel method to unambiguously distinguish Anderson localization from losses.

Resumé

Denne afhandling beskriver kvanteegenskaberne af lys, der undergår multipel spredning i nanostrukturerede medier.

Lysets rumlige kvantekorrelationer, der er forårsaget af multipel spredning af "squeezed" lys og derfor af ren kvantemekanisk oprindelse, er demonstreret eksperimentelt i denne afhandling. Positive og negative rumlige kvantekorrelationer er målt ved at varriere lyskildens kvantetilstand, og vinkelopløste målinger af multipel spredte fotoner viser kvantekorrelationernes ubegrænsede rækkevidde in det diffuserende regime. Det multipel spredte lys er karakteriseret gennem frekvensopløste målinger af kvantestøjen samt tidsopløste fotonkorrelations målinger, og de eksperimentelle data stemmer meget godt overens med kvanteteorien for multipel spredning. Målinger af lysets støjegenskaber i den kohærente bagspredningsregime afslører en forstærkning i de multipel spredte fotoners fluktuationer der er større end den forventede forstærkning af den bagspredte intensitet. Den eksperimentelle demonstration af rumlige kvantekorrelationer og karakteriseringen af kvantetilstanden af det multipel spredte lys danner basis for studierne af kvanteinteferens og kvantesammenfiltring i uordnede medier.

I denne afhandling demonstreres Anderson lokalisering af lys i uordnede fotonisk krystal bølgeledere eksperimentelt. Målinger af transmission viser, at lokaliseringslængden er stærkt dispersiv, hvilket muliggør kontrol over den en-dimensionelle Anderson lokalisering af lys. De statiske egenskaber af Anderson lokalisering er påvist ved at indlejre kvantepunkter i uordnede fotonisk krystal bølgeledere, og den spektrale distribution af Anderson lokaliserede tilstande er bestemt gennem målinger af fotoluminescensen. Sammenligning mellem eksperimentelle data og en-dimensionelle analytiske beregninger vises som en ny metode til utvetydigt at skelne mellem Anderson lokalisering og tab.

List of publications

Journal publications

J1 Stephan Smolka, Alexander Huck, Ulrik L. Andersen, Ad Lagendijk, and Peter Lodahl, *Observation of spatial quantum correlations induced by multiple scattering of nonclassical light*, Physical Review Letters **102**, 193901 (2009).

J2 Alexander Huck, Stephan Smolka, Peter Lodahl, Anders S. Sørensen, Alexandra Boltasseva, Jiri Janousek, and Ulrik L. Andersen, *Demonstration of Quadrature-Squeezed Surface Plasmons in a Gold Waveguide,* Physical Review Letters **102**, 246802 (2009).

J3 Luca Sapienza, Henri Thyrrestrup, Søren Stobbe, Pedro D. Garcia, Stephan Smolka, and Peter Lodahl, *Cavity Quantum Electrodynamics with Anderson-localized Modes,* Science, **327**, 1352 (2010).

J4 Pedro D. Garcia, Stephan Smolka, Søren Stobbe, and Peter Lodahl, *Density of states controls Anderson localization in disordered photonic crystal waveguides,* Physical Review B, **82**, 165103 (2010).

J5 Stephan Smolka, Otto L. Muskens, Ad Lagendijk, and Peter Lodahl, *Spatial photon-coincidence measurements in a multiple scattering medium,* arXiv:1004.1721v1, Submitted (2010).

Journal publications in preparation

J6 Stephan Smolka, Henri Thyrrestrup, Luca Sapienza, Tau B. Lehmann, Kristian R. Rix, Luis S. Froufe-Pérez, Philip T. Kristensen, Pedro D.

Garcia, and Peter Lodahl, *Probing statistical properties of Anderson localization with quantum emitters,* In preparation.

J7 Stephan Smolka, Johan R. Ott, Alexander Huck, Ulrik L. Andersen, and Peter Lodahl, *Controlling Spatial Quantum Correlations in a Multiple Scattering Medium*, In preparation.

J8 Henri Thyrrestrup, Stephan Smolka, Philip Trøst Kristensen, Luca Sapienza and Peter Lodahl, *Light-matter coupling of single emitters and Anderson-localized modes in one-dimensional disordered systems,* In preparation.

Book chapter

B1 H. Bartelt, *et al.*, *Preparation and application of functionalized photonic crystal fibers,* part of Nanophotonic Materials, ISBN 978-0-470-27803-1, Wiley-VCH Verlagsgesellschaft (2008).

B2 Stephan Smolka, Søren Stobbe, and Peter Lodahl *Quantum information on a chip: entangled photons, teleportation and the quantum computer*, part of Beyond optical horizons, today and tomorrow with photonics, 253-265, ISBN 87-92062-34-2, DTU Fotonik, (2009).

B3 Stephan Smolka, *I am fascinated with light*, part of: Beyond optical horizons, today and tomorrow with photonics, 266, ISBN 87-92062-34-2, DTU Fotonik, (2009).

Conference contributions (oral presentations)

C1 Stephan Smolka, Alexander Huck, Ulrik L. Andersen, and Peter Lodahl, *Quantum optics in multiple scattering random media* Danish Optical Society Annual Meeting, Risø, Denmark, 2007.

C2 Stephan Smolka, Michael Barth, and Oliver Benson, *Highly efficient fluorescence sensing with hollow core photonic crystal fibers*, IEEE/LEOS Summer Topical Meetings Conference, Acapulco, Mexico, 2008.

C3 Alexander Huck, Stephan Smolka, Peter Lodahl, Alexandra Boltasseva, and Ulrik L. Andersen, *Generation of Non-Classical Surface-Plasmon Polaritons*, Metamaterials 2008, Rochester, New York, USA, 2008.

C4 Alexander Huck, Stephan Smolka, Peter Lodahl, Alexandra Boltasseva, Jiri Janousek, and Ulrik L. Andersen, *Generation of Non-Classical Surface-Plasmon Polaritons*, Danish Optical Society annual meeting, Nyborg, Denmark, 2008.

C5 Alexander Huck, Ulrik L. Andersen, Stephan Smolka, Alexandra Boltasseva, and, Peter Lodahl, *Excitation and characterization of non-classical surface plasmon polaritons*, NANOMETA, Seefeld, Austria, 2009.

C6 Stephan Smolka, Alexander Huck, Ulrik L. Andersen, Ad Lagendijk, and Peter Lodahl, *Experimental demonstration of spatial quantum correlations in multiple scattering media*, CLEO/IQEC, Baltimore, Maryland, USA, 2009.

C7 Stephan Smolka, Alexander Huck, Ulrik L. Andersen, Ad Lagendijk, and Peter Lodahl, *Spatial quantum correlations generated by multiple scattering of squeezed light* ETOPIM8, Crete, Greece, 2009.

C8 Alexander Huck, Stephan Smolka, Leonid Krivitsky, Peter Lodahl, Anders S. Sørensen, Alexandra Boltasseva, and Ulrik L. Andersen, *Demonstration of quadrature squeezed surface-plasmons in a gold waveguide* CLEO/EQEC Europe, Munich, Germany, 2009.

C9 Pedro D. Garcia, Stephan Smolka, Søren Stobbe, and Peter Lodahl, *Controlling Anderson localization in disordered photonic crystal waveguides* META10, Cairo, Egypt, 2010.

C10 Stephan Smolka, Pedro D. Garcia, Søren Stobbe, and Peter Lodahl, *Controlling Anderson localization in disordered photonic crystal waveguides* CLEO/QELS, San Jose, California, USA, 2010.

C11 Stephan Smolka, Otto L. Muskens, Ad Lagendijk, and Peter Lodahl, *Spatial Photon Correlations in Multiple Scattering Media* CLEO/QELS, San Jose, California, USA, 2010.

C12 Luca Sapienza, Henri Thyrrestrup, Søren Stobbe, Pedro D. Garcia, Stephan Smolka, and Peter Lodahl, *Cavity Quantum Electrodynamics in the Anderson-localized Regime*, CLEO/QELS, San Jose, California, USA, 2010.

C13 Luca Sapienza, Henri Thyrrestrup, Søren Stobbe, Pedro D. Garcia, Stephan Smolka, and Peter Lodahl, *Spontaneous emission of quantum dots in disordered photonic crystal waveguides*, SPIE NanoScience + Engineering, California, USA, 2010.

C14 Luca Sapienza, Henri Thyrrestrup, Søren Stobbe, Pedro D. Garcia, Stephan Smolka, and Peter Lodahl, *Spontaneous emission of quantum dots in disordered photonic crystal waveguides*, International Conference on Physics of Semiconductors, Seoul, Korea, 2010.

C15 Peter Lodahl, Luca Sapienza, Henri Thyrrestrup, Søren Stobbe, Pedro D. Garcia, and Stephan Smolka, *Cavity Quantum Electrodynamics in Disordered Photonic Crystals*, PECS IX, Granada, Spain, 2010.

C16 Pedro D. Garcia, Stephan Smolka, Søren Stobbe, and Peter Lodahl, *Controlling Anderson localization in disordered photonic crystal waveguides* PECS IX, Granada, Spain, 2010.

Contributions to publications

The work described in this thesis has been carried out by many people and in the following I want to specify the contributions in detail.

Observation of spatial quantum correlations induced by multiple scattering of nonclassical light

This experimental research was conducted during my collaboration with Alexander Huck and Ulrik L. Anderson at DTU Fysik and initiated by Peter Lodahl. In particular, I measured the spatial quantum correlations together with Alexander Huck and we worked on the squeezed light source. Together with Peter Lodahl I wrote the paper.

Demonstration of quadrature-squeezed surface plasmons

This research was conducted during my collaboration with Alexander Huck and Ulrik L. Anderson at DTU Fysik. In particular, I contributed to the experimental part of these results.

Cavity Quantum Electrodynamics with Anderson-localized modes

L. Sapienza carried out the photoluminescence and time resolved experiments, analysed the data and contributed to writing the paper. H. Thyrrestrup carried out the spatial characterization of the modes and calculated the mode volume. S. Stobbe fabricated the samples. P.D. Garcia measured the localization length in passive disordered photonic crystal waveguides and was involved in fruitful discussions. S. Smolka studied intensity fluctuations and intensity probability distributions to confirm Anderson localization in disordered photonic crystal waveguides. Furthermore, he measured the localization length in passive disordered photonic crystal waveguides. P. Lodahl initiated and supervised the project and wrote the paper.

Density of states controls Anderson localization in disordered photonic crystal waveguides

P.D. Garcia carried out the measurements, analyzed the experimental data, contributed to the design of the experimental setup, developed a model to explain the dispersion in the extinction mean free path, and wrote the paper. S. Smolka designed and built the experimental setup and analyzed the experimental data. He characterized the measured transmission distributions and compared them with calculations based on the transfer matrix theory formalism. Furthermore, he contributed to writing the paper. S. Stobbe fabricated the samples. P. Lodahl initiated and supervised the project and contributed to writing the paper.

Highly efficient fluorescence sensing with hollow core photonic crystal fibers

These experimental and theoretical results were obtained during my studies at Humboldt University Berlin.

Contents

Chapter 1

Introduction

Multiple wave scattering in disordered systems has fundamental and practical importance in a diverse range of disciplines, such as optics [1, 2], microwaves [3], acoustics [4], and seismology [5]. In case of light, multiple scattering can be applied to, for example, increase the information capacity in optical communication [6, 7]. Furthermore, it plays an important role in quantum optics and quantum information science, where it is essential to enhance the interaction between single photons and quantum emitters [8]. Here, disorder is usually seen as a nuisance since it limits the performance of nanophotonic devices, that are inherently sensitive to fabrication imperfections [9, 10]. According to the common belief, disorder inhibits the observation of any quantum phenomena after averaging over an ensemble of disorder realizations. So far, all experiments concerning multiple scattering have been in the regime where a classical description suffices. Only recently, fundamentally new physics has been theoretically predicted in a quantum optical description of multiple scattering [11, 12, 13, 14], as will be experimentally shown during the course of this thesis.

The direction of propagation through a disordered nanostructure resembles a random walk, from which the medium becomes opaque. The intensity guided through the different trajectories of the medium interferes resulting in a complex intensity distribution. After averaging over all possible realizations of disorder, interference effects generally disappear and the light transport is

described by diffusion theory. Under conditions where multiple scattering is strong, light diffusion is modified leading to spatial intensity correlations [15]. Ultimately, localized modes are formed, turning disorder into an efficient resource for confining light in nanophotonic structures [16, 17].

The interaction between light and matter lies at the heart of quantum optics. Ground-breaking experiments on the interaction of individual quantum systems, such as quantum teleportation [18] and strong light-matter coupling [19], have advanced the fascinating prospects of quantum communication and quantum computing. During the past decades, tremendous progress has been made to enhance the light-matter interaction by, for example, confining light in highly engineered cavities [20]. Quite remarkably, an alternative route towards light confinement exploits multiple scattering as first proposed by P.W. Anderson [21]. Light propagation is inhibited and the envelope of the ensemble averaged intensity profile decays exponentially from the source on a typical length scale called localization length. Anderson localization is a universal interference phenomenon that has been observed for, e.g., light [22, 17, 3], sound waves [23], and matter waves [24]. Observing Anderson localization in completely disordered systems is very challenging, though. S. John introduced an alternative approach to Anderson localization [25]. Instead of using entirely disordered samples, he proposed theoretically that light localization occurs in periodic dielectric materials, called photonic crystals, after inducing only a slight amount of disorder.

This thesis contributes to two fields of research of multiple scattering in the realm of quantum optics exploiting multiple scattering as a resource, rather than as a nuisance.

In the first part of this thesis, predicted spatial quantum correlations of purely quantum origin and induced by multiple scattering are demonstrated experimentally. As a consequence, the number of photons scattered into one direction can be predicted from the number of photons detected in a different direction. The quantum nature of light is exploited by the fluctuations in the multiply scattered photons. For the first time, ensemble-averaged photon fluctuations reduced beyond the classical limit are observed, showing that nonclassical properties of light survive the complex stochastic process of multiple scattering, thereby disproving the common belief that quantum properties of

light are fragile. Remarkably, the spatial quantum correlations give rise to significant deviations in the transport of photon fluctuations as compared to the transport of light intensity in multiple scattering media. The obtained results constitute the first experiments in the realm of multiple scattering that cannot be explained by classical means and can be potentially used for breaking the classical limit on the information capacity.

The second part concerns the light confinement in disordered nanostructures. In particular, Anderson-localized cavity modes are generated by deliberately adding disorder in photonic crystal waveguides. For the first time, emitters are embedded into disordered photonic crystal waveguides and coupled to an Anderson-localized mode. Thereby, the emission rate of an embedded semiconductor quantum dot can be strongly enhanced. The experimental conformation of Anderson localization is recurrently debated since it can usually not be distinguished from losses such as light leakage or absorption [26, 27]. Here, a fundamentally different approach is developed by utilizing many quantum dots embedded in the disordered structure. The quantum dot photoluminescence is exploited to probe the statistical properties of Anderson localization. Using this approach the localization length and the loss length can be measured independently in the photonic crystal waveguide. Additionally, a thorough analysis is presented to estimate the localization length from transmission measurements in photonic crystal waveguides without embedded emitters. The obtained results on disorder-induced light confinement provide an efficient platform for disorder-robust quantum electrodynamics and offer a new approach to test fundamental questions of Anderson localization.

The outline of the thesis is as follows: In Chapter 2, a continuous-mode quantum theory of multiple scattering is derived and compared to quantum noise measurements of photon fluctuations. Positive and negative spatial quantum correlations induced by multiple scattering of squeezed light are demonstrated. Chapter 3 discusses experiments on spatial photon coincidence-measurements of multiply scattered light. The photon fluctuations in a single optical speckle are studied in angular-resolved measurements. The spatial photon correlation function between two different directions is found to be infinite in range and its strength can be tuned by varying the quantum state of the incident light source. Further experiments in the coherent backscattering cone

reveal enhanced backscattered photon fluctuations that are larger than the enhancement factor of two predicted for the intensity transport. Furthermore, the coherent backscattering cone is investigated in the few photon regime using a spontaneous down-conversion light source.

Chapter 4 provides analytical calculations to determine the statistical properties of Anderson localization in disordered one-dimensional systems. A transfer matrix theory method and a Green's function formalism are used to study transmission and local density of states distributions. From the frequency dependence of the local density of states, the spectral linewidth of Anderson-localized modes is calculated. Chapter 5 demonstrates the control of Anderson-localization in disordered photonic crystal waveguides. The extinction mean free path is studied in transmission measurements and identified with the localization length at the vicinity of the waveguide mode band edge. The extinction mean free path is found to be disorder dependent and strongly dispersive, which is confirmed by measurements of the transmission distributions. Chapter 6 reports on measurements that probe the statistical properties of Anderson localization by embedding quantum dots inside photonic crystal waveguides. The spectral distribution of Anderson-localized modes is used to estimate the localization length and to distinguish Anderson localization from losses. A single quantum emitter is coupled to an Anderson-localized mode leading to enhanced light-matter interaction. Finally, the conclusions are presented in Chapter 7.

Part I

Light propagation in a multiple scattering medium

Chapter 2

Quantum correlations induced by multiple scattering of light

2.1 Introduction

Recently, the interest in multiple scattering experiments utilizing the quantum properties of light has increased rapidly [28, 29, 30, 31, 32]. The theoretical framework for a quantum optical description of multiple scattering was derived by Beenakker and co-worker. They related the scattering matrix to the photon statics [11] and calculated the impact of gain and absorption in multiple scattering media on the quantum state of the transmitted light [13]. Lodahl, et *al.* carried out the first quantum optical experiments by investigating the transmission of photon fluctuations through a multiple scattering medium in the diffusive regime [28]. Further experiments showed that classical intensity correlations [15] change the transmitted photon probability distributions [29]. So far, quantum optical variables have only been measured in very few multiple scattering experiments that only have focused on the regime of a classical light source. To enter the quantum regime of multiple scattering, nonclassical

light sources are required. An example is the quantum mechanical generalization of the spatial intensity correlations [15]. This theoretically predicted spatial quantum correlation function is induced by multiple scattering of light and shows an entirely different behaviour for classical and nonclassical light sources, respectively [12, 14, 32, 33].

This chapter presents the first experimental observation of spatial quantum correlations induced by multiple scattering of squeezed light [30]. In order to motivate the experiments, the fundamental concepts of multiple scattering are introduced in Section 2.2. After a brief review of the classical description, a continuous-mode quantum theory of multiple scattering is developed in Section 2.3. Section 2.4 presents measurements on multiply scattered photon fluctuations. Using a squeezed light source, spatial quantum correlations are investigated and the results are discussed in Section 2.5.

2.2 Fundamentals of multiple scattering

Any inhomogeneities originating from particles of different shape and size cause scattering of the waves along different directions. If the impurities are randomly distributed over the entire medium, the waves might be repeatedly scattered and the ballistic propagation is not sufficient to describe the light transport (Fig. 2.1). The direction of propagation tends to be lost and the medium becomes opaque. The average distance between two scattering events is defined by the scattering mean free path, ℓ_s. Multiple scattering occurs if the sample size, L, exceeds ℓ_s. For uncorrelated scatters, the scattering mean free path can be evaluated from the density of the scatter, ρ, and the average scattering cross-section, σ_s

$$\ell_s = \frac{1}{\rho\,\sigma_s}. \tag{2.1}$$

The scattering cross-section describes the scattering strength between the incident wave and the particle. When the medium shows isotropic scattering in all directions, ℓ_s might simply be identified with the transport mean free path ℓ. In the weakly multiple scattering regime, with $\lambda \ll \ell \ll L$, the different possible light trajectories through the medium interfere leading to the formation of a complex spatial intensity distribution of the light exiting the sample, cf.

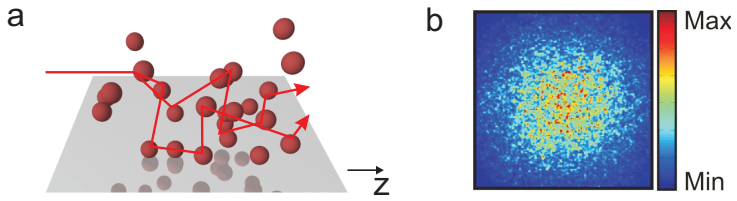

Figure 2.1: **a**, *When light enters a randomly disordered medium, it is split into a multitude of different trajectories that perform a random walk through the medium. Thereby the different light trajectories can interfere with each other.* **b**, *Measured spatial intensity distribution of light transmitted through a multiple scattering medium displaying a volume speckle pattern.*

Fig. 2.1b. To characterize a complex system with randomly distributed scatters, it is essential to investigate physically predictable variables after ensemble averaging over all possible realizations of disorder. In this process, interference effects tend to vanish, and light transport is described by a diffusion process.

The light propagation in a random multiple scattering medium requires solving Maxwell's equations, taking into account the shape, size and position of each scatter. Neglecting interference effects after ensemble averaging simplifies the calculation. The transport of the ensemble-averaged light intensity, $\overline{I(\vec{r},t)}$, is then approximated by a random walk and can be viewed as a diffusion process. The diffusive light transport describes almost all physical processes of multiple scattering in three-dimensional disordered media. The light propagation follows in absence of absorption the diffusion equation [15]

$$\frac{\partial}{\partial t}\overline{I(\vec{r},t)} = D\nabla^2\overline{I(\vec{r},t)} + S(\vec{r},t), \tag{2.2}$$

where $S(\vec{r},t)$ describes the light source. The transport through the medium is quantified by the diffusion constant, $D = v_e\ell/3$, with v_e being the energy velocity. When the diffusion constant decreases, the transport process slows down. Light transport in diffusive media is very different as compared to ballistic light transport in homogeneous media where the intensity decays exponentially (law of Lambert-Beer).

An important parameter in the realm of multiple scattering is the transmission through the medium. Here we distinguish between the ensemble-averaged

transmission, $\overline{T_b}$, in a certain direction, b, and the total transmission that is integrated over all angles, $\overline{T}$, where the bar denotes the ensemble average. The transmission through a sample with a slab geometry[1] can be calculated analytically from the diffusion equation. The diffusion equation for the intensity requires extrapolative boundary conditions with $I(z) = 0$ at $z = -z_{e_1}$ and $z = L + z_{e_2}$ with L being the system length and $z_{e_{1,2}}$ being the extrapolation lengths. The extrapolation lengths account for internal reflections at the sample interfaces and simplifies to $z_e = 2/3\ell$ for vanishing reflections [34, 35]. Incorporating the boundary conditions to the stationary diffusion equation leads to the total transmission [36]

$$\overline{T} = \frac{\ell + z_{e_1}}{L + z_{e_1} + z_{e_2}} \times (1 - R_{\text{surf}})\,. \tag{2.3}$$

In addition, we introduce the sample surface reflection R_{surf} to account for the light that is reflected on the incident surface and does not enter the multiple scattering medium. Hence, the total transmission is directly related to the transport mean free path and sample thickness and is often approximated to $\overline{T} \simeq \ell/L$.

Under conditions where multiple scattering is strong, the diffusion process is modified leading to spatial intensity correlations. These correlations imply that the multiply scattered light intensity observed at one position depends on the intensity at another position even after ensemble averaging over all realizations of disorder. A general definition of the spatial intensity correlation function between two different angular directions b_0 and b_1 is given by [37]

$$C^{(C)}_{ab_0a'b_1} \equiv \frac{\overline{T_{ab_0}T_{a'b_1}}}{\overline{T_{ab_0}} \times \overline{T_{a'b_1}}}, \tag{2.4}$$

where a, a' are the incident light directions. One distinguishes three different types of transmission correlations, $C^{(C)}_{ab_0a'b_1} = C^{(1)} + C^{(2)} + C^{(3)}$. The first term is of the order of unity and refers to the short range correlations that dominates for very small angles between b_0 and b_1. $C^{(2)}$ describes the long-range correlation of the sample [37]. The correlation scales with g^{-1}. $g = \sum_a \overline{T}$ is the conductance of the sample and defined as the total transmission summed over all incident directions. The last term, $C^{(3)}$, is the optical analogue of the

[1] The system is assumed to be infinite in x and y direction and finite in $z = 0 \ldots L$.

Universal Conductance Fluctuations [38] and scales with the inverse square of the conductance.

2.3 Continuous-mode quantum theory of multiple scattering

One of the fundamental principles of quantum mechanics concerns the quantization of the electric field. As a consequence, vacuum fluctuations were predicted that are associated with the zero point energy and can be used to, e.g., explain the spontaneous emission processes. The quantized electric field, expanded in terms of plane waves, takes the form [39]

$$\vec{E}(\vec{r},t) = \sum_{\vec{k}} \vec{\epsilon}_{\vec{k}}\, \hat{a}_{\vec{k}}\, e^{-i\omega t + i\vec{k}\cdot\vec{r}} + \sum_{\vec{k}} \vec{\epsilon}_{\vec{k}}\, \hat{a}^{\dagger}_{\vec{k}}\, e^{i\omega t - i\vec{k}\cdot\vec{r}}, \tag{2.5}$$

where $\vec{k}$ is the wave number, $\vec{\epsilon}_{\vec{k}}$ is a normalization constant and ω is the frequency. The operators $\hat{a}$ and $\hat{a}^{\dagger}$ are referred to as the electric field annihilation and creation operators, respectively. The photon number operator is defined as $\hat{n} = \hat{a}^{\dagger}\hat{a}$. The quantum mechanical expectation value of the photon number operator, denoted by $\langle \ldots \rangle$, corresponds to the classical intensity of the light field, i.e., $I \propto \langle \hat{n} \rangle$. Fluctuations in the number of photons are given by the variance in the photon number: $\Delta n^2 \equiv \langle \hat{n}^2 \rangle - \langle \hat{n} \rangle^2$ and reveal the quantum nature of light. Due to the Heisenberg uncertainty principle intrinsic quantum fluctuations are always present. Although of inherent quantum origin, photon fluctuations are classified as either classical or non-classical if similar fluctuations can be induced by classical light sources or not. The classical boundary corresponds to Poissonian photon statistics where the variance in the photon number fluctuations equals the mean number of photons. A purely quantum regime exists where photon fluctuations are reduced beyond the classical limit leading to sub-Poissonian photon statistics. A single-photon state, which can be generated by the decay of an excited emitter [40], will ideally have vanishing photon fluctuations. Sub-Poissonian photon statistics can be generated in bright beams containing many photons. An example of such a quantum state is the amplitude squeezed state, that can be generated by a quadratic nonlinear process and possess strongly reduced photon fluctuations [41].

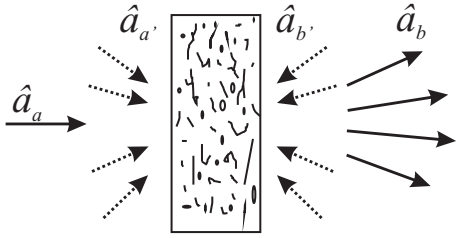

Figure 2.2: Scheme to illustrate the quantum theory of multiple scattering. The annihilation operator, $\hat{a}_a$, represents a single quantum state of light that couples to the input mode a of the disordered medium. After multiple scattering, the light exits the medium in different angular directions b with the electric field transmission coefficients t_{ab}. The direction corresponds to different $\vec{k}$-vectors of the incoming and outgoing light. All other incident channels $a' \neq a$ and b' couple vacuum fluctuations into the medium that need to be incorporated in the quantum description.

The theoretical model describing light propagation through a non-absorbing, multiple scattering medium is based on quasi one-dimensional calculations that are a very good approximation to three-dimensional systems [11, 13]. An illustration of the model is shown in Fig. 2.2 where an incident quantum state enters the medium in direction a. This direction is determined by the wave vector $\vec{k}$. The angular frequency, ω, defines the length of the wave vector vector, i.e., $k = |\vec{k}| = n\omega/c$, with c being the vacuum speed of light and n the refractive index. The continuous mode annihilation operator of the spatial output mode b is related to the annihilation operators of all incident modes a', b',

$$\hat{a}_b(\omega) = \sum_{a'=1}^{N} t_{a'b}\hat{a}_{a'}(\omega) + \sum_{b'=N+1}^{2N} r_{b'b}\hat{a}_{b'}(\omega). \tag{2.6}$$

The summations are evaluated for all N input and N output modes. t, r are the electric field transmission and reflection coefficients which are assumed to be frequency independent within the spectral range of interest.

Light beams are time-dependent since they do not continue forever and often exhibit variations on time-scales comparable to the observation time [42].

In the continuous-mode theory, a collimated light beam is considered as a superposition of modes with a multitude of wave vectors pointing in the same direction, $\vec{e}_k = \vec{k}/|\vec{k}|$. This leads to a dispersion relation and the frequency, ω, can be considered as the characteristic variable instead. Introducing the continuous-mode theory allows us to consider the dispersion relation to be continuous. The continuous-mode annihilation and creation operators between two different spatial directions a and a' is then defined as

$$\left[\hat{a}_a(\omega), \hat{a}^\dagger_{a'}(\omega')\right] = \delta(\omega - \omega')\delta_{a,a'}. \tag{2.7}$$

This expression incorporates the continuous frequency relation (Dirac delta function $\delta(\omega - \omega')$) and the discrete number of spatial directions since a multiple scattering sample exhibits only $2N$ uncorrelated input and output modes (Kronecker delta $\delta_{a,a'}$). The photon number operator per angular frequency (photon flux) can be written as $\hat{n}_a(\omega) = \hat{a}^\dagger_a(\omega)\hat{a}_a(\omega)$.

2.3.1 Spatial quantum correlation function

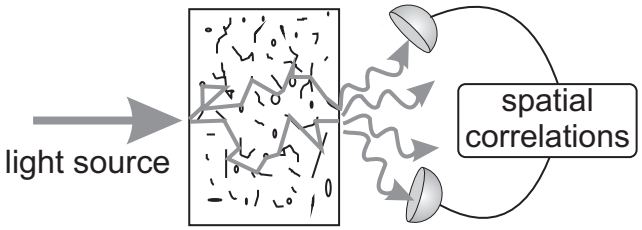

Figure 2.3: Illustration of a multiple scattering process leading to spatial quantum correlations. A light source illuminates a medium consisting of a random distribution of scatters. The number of photons exiting the medium in a specific direction can be anti correlated with the number of photons in another direction, and this correlation depends on the quantum state of light illuminating the medium.

In this section we derive the spatial quantum correlation function between two different output directions of a multiple scattering medium. Figure 2.3 illustrates the nature of spatial quantum correlations that can be obtained by correlating the number of photons at two different output directions. The

spatial quantum correlation function between two different output directions b_0, b_1 and frequencies ω, ω' is defined as

$$\overline{C^Q_{b_0 b_1}(\omega,\omega',\Delta\omega)} = \frac{\overline{\langle : \tilde{n}_{b_0}(\omega,\Delta\omega)\tilde{n}_{b_1}(\omega',\Delta\omega) : \rangle}}{\overline{\langle \tilde{n}_{b_0}(\omega,\Delta\omega)\rangle} \times \overline{\langle \tilde{n}_{b_1}(\omega',\Delta\omega)\rangle}}. \tag{2.8}$$

$\langle : \cdots : \rangle$ is the quantum mechanical expectation value of normally ordered operators that is given by the photon detection process [39] and the bars refer to the classical ensemble average. The need for two averages is due to the fact that both quantum fluctuations and random multiple scattering are stochastic processes. Eq. (2.8) represents a frequency-resolved measurement that is limited by the resolution bandwidth $\Delta\omega$. Here, we introduce the experimentally relevant dimensionless photon number within the resolution bandwidth $\Delta\omega$

$$\tilde{n}(\omega,\Delta\omega) = \int_{\omega-\Delta\omega/2}^{\omega+\Delta\omega/2} \hat{n}(\omega')\, d\omega'. \tag{2.9}$$

In the following we want to relate the annihilation and creation operators of the multiply scattered light to the incident light source. We insert Eq. (2.9) in Eq. (2.8) and obtain

$$\overline{C^Q_{b_0 b_1}(\omega,\omega',\Delta\omega)} = \frac{\int_{\omega-\Delta\omega/2}^{\omega+\Delta\omega/2} d\omega_x \int_{\omega'-\Delta\omega/2}^{\omega'+\Delta\omega/2} d\omega_y\, \overline{\langle : \hat{n}_{b_0}(\omega_x)\hat{n}_{b_1}(\omega_y) : \rangle}}{\int_{\omega-\Delta\omega/2}^{\omega+\Delta\omega/2} d\omega_x \int_{\omega'-\Delta\omega/2}^{\omega'+\Delta\omega/2} d\omega_y\, \overline{\langle \hat{n}_{b_0}(\omega_x)\rangle} \times \overline{\langle \hat{n}_{b_1}(\omega_y)\rangle}}. \tag{2.10}$$

First, we calculate the quantum mechanical expectation values. Based on Eq. (2.6) we can evaluate $\langle \hat{n}_b(\omega)\rangle$ and get

$$\begin{aligned} \langle \hat{n}_b(\omega)\rangle &= \sum_{a',a''} t^*_{a'b} t_{a''b} \langle \hat{a}^\dagger_{a'}(\omega)\hat{a}_{a''}(\omega)\rangle \\ &= \sum_{a',a''} t^*_{a'b} t_{a''b} \langle \hat{n}_a(\omega)\rangle \delta_{a',a}\delta_{a'',a} \\ &= T_{ab}\langle \hat{n}_a(\omega)\rangle, \end{aligned} \tag{2.11}$$

where $T_{ab} = t^*_{ab} t_{ab}$ is the intensity transmission coefficient. In Eq. (2.11) we exploited that the light source only couples to the input mode a and the average number of photons in all other input modes equals $\langle \hat{n}_{a'\neq a,b'}(\omega)\rangle = 0$. In order to calculate the photon fluctuations (discussed further below), we express the numerator in Eq. (2.10) by unordered operators which equals the ordered expression for $b_0 \neq b_1$, i.e., $\langle : \hat{n}_{b_0}(\omega_x)\hat{n}_{b_1}(\omega_y) : \rangle = \langle \hat{n}_{b_0}(\omega_x)\hat{n}_{b_1}(\omega_y)\rangle$. A detailed

derivation is shown in Appendix A. As a result we get

$$\begin{aligned}\langle \hat{n}_{b_0}(\omega_x)\hat{n}_{b_1}(\omega_y)\rangle &= t^*_{ab_0}t_{ab_1}\langle \hat{n}_a(\omega_x)\rangle\delta(\omega_x-\omega_y)\delta_{b_0,b_1} \\ &\quad + T_{ab_0}T_{ab_1}\left(\langle \hat{n}_a(\omega_x)\hat{n}_a(\omega_y)\rangle - \langle \hat{n}_a(\omega_x)\rangle\delta(\omega_x-\omega_y)\right).\end{aligned} \tag{2.12}$$

In the experiment, we record the correlation function for frequencies within the resolution bandwidth, $\omega_x - \omega_y < \Delta\omega$ and can therefore integrate Eq. (2.10) (for small $\Delta\omega$)

$$\int_{\omega-\Delta\omega/2}^{\omega+\Delta\omega/2} d\omega_x\, \delta(\omega_x-\omega_y) \approx \delta_{\omega,\omega_y}. \tag{2.13}$$

After evaluating the quantum mechanical expectation values, we now focus on the classical ensemble average. The photon number operator, $\hat{n}_a(\omega)$, of the incident quantum state of light is not affected by multiple scattering. In order to perform the ensemble average of Eq. (2.11) and Eq. (2.12), only the transmission coefficients, $\overline{T_{ab}}$ and $\overline{T_{ab_0}T_{ab_1}}$, need to be calculated. This results in the dimensionless spatial quantum correlation function between two independent output modes of a multiple scattering medium, b_0, b_1, and light coupling into a single input mode a

$$\overline{C^Q_{ab_0ab_1}(\omega,\Delta\omega)} = \frac{\langle \tilde{n}_a(\omega,\Delta\omega)\,\tilde{n}_a(\omega,\Delta\omega)\rangle - \langle \tilde{n}_a(\omega,\Delta\omega)\rangle}{\langle \tilde{n}_a(\omega,\Delta\omega)\rangle\langle \tilde{n}_a(\omega,\Delta\omega)\rangle} \times C^{(C)}_{ab_0ab_1}. \tag{2.14}$$

$\tilde{n}_a(\omega,\Delta\omega)$ depicts the photon number within the bandwidth $\Delta\omega$ (Eq. (2.9)). The spatial intensity correlation, $C^{(C)}_{ab_0ab_1}$ (Eq. (2.4)), reveals the classical intensity correlations of multiply scattered light and equals one in the diffusive regime. Thus, the spatial quantum correlation function is the quantum optical generalization of the spatial intensity correlations. In Eq. (2.14) we assumed that than ω and ω' cannot be distinguished within the resolution bandwidth $\Delta\omega$. Alternatively, the spatial quantum correlation function can be expressed as

$$\overline{C^Q_{ab_0ab_1}(\omega,\Delta\omega)} = \left[1 + \frac{F_a(\omega,\Delta\omega)-1}{\langle \tilde{n}_a(\omega,\Delta\omega)\rangle}\right] \times C^{(C)}_{ab_0ab_1}, \tag{2.15}$$

where $F_a(\omega,\Delta\omega) \equiv \Delta\tilde{n}^2_a(\omega,\Delta\omega)/\langle \tilde{n}_a(\omega,\Delta\omega)\rangle$ is the dimensionless Fano factor and $\Delta\tilde{n}^2(\omega,\Delta\omega) = \langle \tilde{n}(\omega,\Delta\omega)^2\rangle - \langle \tilde{n}(\omega,\Delta\omega)\rangle^2$ is the variance in the photon

number fluctuations within the bandwidth $\Delta\omega$. The Fano factor gauges the variance in the photon number fluctuations of the light source entering the multiple scattering medium in direction a. The size of the Fano factor determines the transition from the classical ($F_a(\omega, \Delta\omega) \geq 1$) to the nonclassical regime ($F_a(\omega, \Delta\omega) < 1$). Here it becomes apparent that a quantum state of light does not only depends on the angular frequency ω but also on the bandwidth. Using nonclassical light opens the door to a genuine quantum regime where $0 \leq C^{Q}_{ab_0ab_1}(\omega, \Delta\omega) < 1$, corresponding to spatially anti-correlated photons. Such spatial quantum correlations are of *infinite range* in the sense that the magnitude is independent of the angular difference of the two uncorrelated output directions, which translates into a spatial separation in the far field. This is an example of the fundamentally new phenomena that arise in quantum optical descriptions of multiple scattering of light.

2.3.2 Photon number fluctuations

The mean number of transmitted photons through a multiple scattering medium is obtained from the sum over all output modes, $\langle \hat{n}_T(\omega) \rangle = \sum_b \langle \hat{n}_b(\omega) \rangle$. The variance in the transmitted photon fluctuations is the sum of the individual output modes and the cross-correlations between different modes

$$\Delta n_T^2(\omega) \quad = \quad \sum_b \Delta n_b^2(\omega) + \sum_{b_0} \sum_{b_1 \neq b_0} \langle \hat{n}_{b_0}(\omega) \hat{n}_{b_1}(\omega) \rangle - \langle \hat{n}_{b_0}(\omega) \rangle \langle \hat{n}_{b_1}(\omega) \rangle. \tag{2.16}$$

It turns out that cross-correlations are significant in a multiple scattering medium and give rise to spatial quantum correlations. The variance in the photon fluctuations (Eq. (2.16)) can be evaluated in a similar way as presented for the spatial quantum correlation function. In the experiment it is not feasible to collect the multiply scattered light from all output modes and the collection efficiency is smaller than one. We therefore introduce the overall detection efficiency, η. The ensemble-averaged variances in the detectable multiply scattered

photon fluctuations are calculated to be (see Appendix A for details)

$$\begin{aligned}\overline{\Delta\tilde{n}_T^2(\omega,\Delta\omega)} &= \eta\overline{T}\langle\tilde{n}_a(\omega,\Delta\omega)\rangle \\ &\quad +\eta^2\overline{T}^2\langle\tilde{n}_a(\omega,\Delta\omega)\rangle\left(F_a(\omega,\Delta\omega)-1\right), \qquad (2.17)\\ \overline{\Delta\tilde{n}_R^2(\omega,\Delta\omega)} &= \eta\left(1-\overline{T}\right)\langle\tilde{n}_a(\omega,\Delta\omega)\rangle \\ &\quad +\eta^2\left(1-\overline{T}\right)^2\langle\tilde{n}_a(\omega,\Delta\omega)\rangle\left(F_a(\omega,\Delta\omega)-1\right). \qquad (2.18)\end{aligned}$$

The total transmitted and reflected variance, respectively is represented by $\overline{\Delta\tilde{n}_{T,R}^2(\omega,\Delta\omega)}$ and $\overline{T}$ is the ensemble-averaged total transmission coefficient. The calculations are carried out in the diffusive regime in the limit of a large number of optical modes, N. Therefore the additional contribution due to coherent backscattering can be neglected in the total reflection coefficient $\overline{R} = 1-\overline{T}$. In the diffusive regime, the spatial quantum correlation can be evaluated from the ensemble average total transmitted photon fluctuations

$$\overline{C^Q_{ab_0ab_1}(\omega,\Delta\omega)} = 1+\frac{\overline{F_T(\omega,\Delta\omega)}-1}{\eta\overline{T}\langle\hat{n}_a(\omega,\Delta\omega)\rangle}, \qquad (2.19)$$

with $\overline{F_T(\omega,\Delta\omega)}$ being the ensemble-averaged Fano factor of the total transmitted light. Note that this result only holds in the diffusive regime where the average sample transmission, $\overline{T_{ab}}$, is assumed to be identical in all directions b. A similar result can be calculated for the spatial quantum correlation in reflection geometry.

So far, we have calculated the variance in the multiply scattered photon number and the spatial quantum correlation function in the frequency-domain. A possible experimental setup to measure $\overline{\Delta\tilde{n}_T^2(\omega,\Delta\omega)}$ and $\overline{C^Q_{ab_0ab_1}(\omega,\Delta\omega)}$ consists of a photodiode that converts the photons into a photo-current. A spectrum analyzer measures the variance of the Fourier transformed photo current at a frequency ω within the resolution bandwidth, $\Delta\omega$, that is proportional to the variance in the photon fluctuations, $\Delta\tilde{n}^2(\omega,\Delta\omega)$. Since the proportionality constant is not known and depends on the device settings, we utilize the fact that a coherent quantum state is defined by $\Delta\tilde{n}_c^2(\omega)/\langle\tilde{n}_c(\omega)\rangle = 1$. Thus, the spectrum analyzer can be used to compare an unknown quantum state of light with a coherent light source which exhibits the same average number of photons, $\langle\tilde{n}(\omega,\Delta\omega)\rangle = \langle\tilde{n}_c(\omega,\Delta\omega)\rangle$. We can extract the Fano factor independent

on the device parameter

$$F \equiv \frac{\Delta\tilde{n}^2(\omega,\Delta\omega)}{\langle\tilde{n}(\omega,\Delta\omega)\rangle} = \frac{\Delta\tilde{n}^2(\omega,\Delta\omega)}{\Delta\tilde{n}_c^2(\omega,\Delta\omega)}. \tag{2.20}$$

A second important parameter to derive the spatial quantum correlation function involves the estimation of the mean photon number, see Eq. (2.19). The time-dependent annihilation operator is defined via a Fourier integral

$$\hat{a}(t) \quad = \quad \frac{1}{\sqrt{2\pi}}\int_{-\infty}^{\infty} d\omega\, \hat{a}(\omega)e^{i\,\omega\,t}, \tag{2.21}$$

with the corresponding commutator relation (substituting Eq. (2.7))

$$\begin{aligned}\left[\hat{a}(t),\hat{a}^\dagger(t')\right] &= \frac{1}{2\pi}\int_{-\infty}^{\infty}\int_{-\infty}^{\infty} d\omega\, d\omega' \left[\hat{a}(\omega),\hat{a}^\dagger(\omega')\right] e^{i\omega t}\, e^{-i\omega' t'} \\ &= \delta(t-t').\end{aligned} \tag{2.22}$$

Instead of measuring $\langle\hat{n}(\omega,\delta\omega)\rangle$ directly, we detect experimentally the mean photon number in the time domain, $\langle\hat{n}(t,\Delta T)\rangle$, within the time interval ΔT, that is related to the frequency domain via related via (Eq. (2.21))

$$\begin{aligned}\langle\hat{n}_a(t,\Delta T)\rangle &= \int_t^{t+\Delta T} d\tau\, \langle\hat{a}_a^\dagger(\tau)\hat{a}_a(\tau)\rangle \\ &= \frac{1}{2\pi}\int_t^{t+\Delta T} d\tau \int_{-\infty}^{\infty} d\omega \int_{-\infty}^{\infty} d\omega'\, \langle\hat{a}_a^\dagger(\omega)\hat{a}_a(\omega')\rangle e^{-i(\omega'-\omega)\tau}.\end{aligned} \tag{2.23}$$

If $\Delta T(\omega-\omega') \gg 1$ then the last equation simplifies to

$$\langle\hat{n}_a(t,\Delta T)\rangle \approx \int_{\omega_0-\frac{\Delta\omega}{2}}^{\omega_0+\frac{\Delta\omega}{2}} d\omega\, \langle\hat{a}_a^\dagger(\omega)\hat{a}_a(\omega)\rangle. \tag{2.24}$$

Thus we can link the mean photon number in the time domain to the mean photon number in the frequency domain

$$\langle\hat{n}_a(t,\Delta T)\rangle \approx \langle\hat{n}_a(\omega_0,\Delta\omega)\rangle. \tag{2.25}$$

It is important to realize the difference between $\Delta\omega$ and $\delta\omega$ caused by the definition of our quantum state. In the experiment the mean number of photons is dominated by a coherent light beam centered around ω_0 with a line width $\Delta\omega$. However, the Fano factor is investigated at a sideband frequency ω within the bandwidth $\delta\omega$. We assume that $F_a(\omega,\delta\omega)$ is approximately constant throughout the frequency interval of the quantum state, $[\omega\pm\frac{\delta\omega}{2},\omega_0\pm\frac{\Delta\omega}{2},\omega'\pm\frac{\delta\omega}{2}]$.

2.4 Quantum noise measurements

2.4.1 Experimental setup

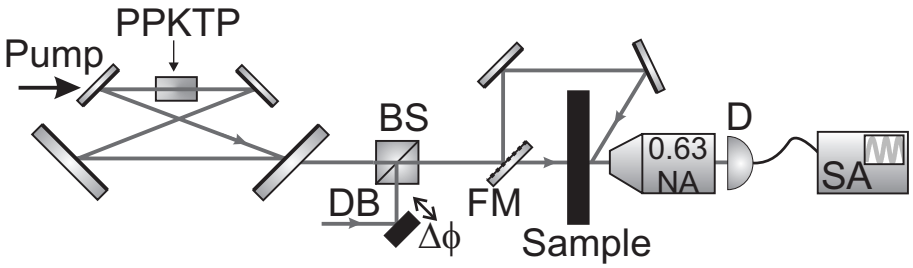

Figure 2.4: Sketch of the experimental setup. Vacuum squeezing is generated in an optical parametric amplifier with a periodically poled potassium titanyl phosphate (PPKTP) nonlinear crystal, overlapped with a displacement beam (DB) on a beam splitter (BS), and directed onto the sample (S). The flip mirror (FM) is used to choose between transmission and reflection measurements. The multiply scattered light is imaged onto a photo-detector (D) and its photon fluctuations are recorded using an electronic spectrum analyzer (SA).

The experimental setup to study the photon fluctuations of multiply scattered light is schematically shown in Fig. 2.4. As a nonclassical light source we use squeezed light generated in a second-order nonlinear process at a wavelength of $\lambda = 1064\,\mathrm{nm}$ corresponding to a frequency of $\omega_0 = 2.8 \cdot 10^{14}\,\mathrm{Hz}$ [41]. This versatile nonclassical source features continuous tuning between classical and nonclassical photon fluctuations. The photon fluctuations are recorded with a photo detector. The DC voltage of the photo detector is related to the light intensity, i.e., the average number of photons per second, $\langle \hat{n}(t) \rangle$. The AC voltage of the photo detector contains the time-dependent fluctuations. An electrical spectrum analyzer computes the frequency-resolved variance in the photon fluctuations, $\Delta n^2(\omega, \Delta\omega)$ at the sideband frequency ω relative to the carrier frequency of the light source, ω_0. This experimental technique is called quantum noise measurement and allows us to investigate relative photon fluctuations within our experimental resolution bandwidth $\Delta\omega = 300\,\mathrm{kHz}$, that is set by the spectrum analyzer. As a detection frequency we choose the resonance frequency of the photo detector, $\omega = 3.93\,\mathrm{MHz}$. Figure 2.3

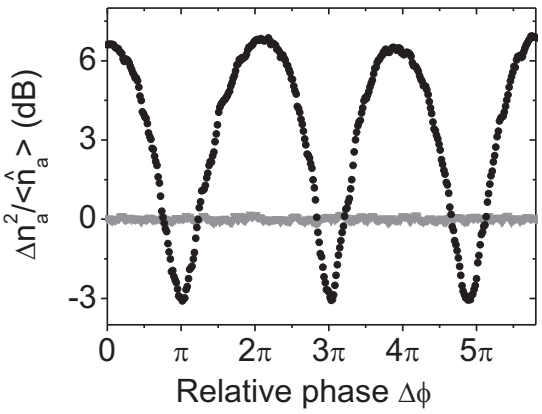

Figure 2.5: Measured photon fluctuations of the squeezed light source depending on the relative phase between the squeezed vacuum generated in the optical parametric amplifier and the bright displacement beam (black circles). The gray triangles plot the measurement of a coherent laser representing the classical limit. We obtain a squeezing of 0.52 ± 0.02 *(*≈ -3 *dB) and an anti-squeezing of* 4.6 ± 0.2 *(*≈ 7 *dB). The detection frequency in the experiment is* 3.93 *MHz and the resolution bandwidth of the spectrum analyzer is* 300 *kHz.*

plots the recorded variance in the photon fluctuations of the light source. The classical limit (gray triangles) is recorded by blocking the squeezed vacuum beam and measuring the bright displacement beam. When the squeezed vacuum is unblocked, it interferes with the displacement beam and the photon fluctuations of the nonclassical light source are recorded. The change in the average number of photons by unblocking the squeezed vacuum is negligible and $\langle \hat{n}_a(\omega, \Delta\omega) \rangle$ is approximated to be the same as from the bright displacement beam $\langle \hat{n}_c(\omega, \Delta\omega) \rangle$. This allows us to estimate the Fano factor of the light source, $F_a(\omega, \Delta\omega)$ (cf. Eq. (2.20)). The phase of the displacement beam, $\Delta\phi$, is scanned with a mirror that is mounted on a piezo-electric element (see Fig. 2.4). Thereby the photon fluctuations of the incident light are continuously tuned. As shown in Fig. 2.5 (black circles) the photon fluctuations of the nonclassical light source ($F_a(\omega, \Delta\omega) = 0.52 \pm 0.02$) can be reduced below the classical limit ($F_a(\omega, \Delta\omega) = 1$) and excess fluctuations can be induced above the classical limit ($F_a(\omega, \Delta\omega) = 4.6 \pm 0.2$). The uncertainty in the Fano factor is estimated

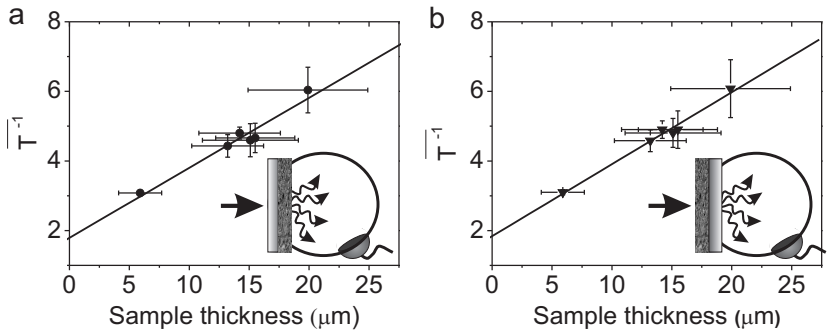

Figure 2.6: **a**, *Measured inverse total transmission through the multiple scattering samples versus sample thickness obtained using an integrating sphere. The back surface of the samples with a glass interface is illuminated under an angle* $\theta = 90°$. ***b***, *Similar measurement method as in* **a**, *but in this case the front surface of the sample is illuminated. The red lines represent a linear fit to the data whereby the transport mean free path and the extrapolation lengths are obtained. The extrapolation lengths and the surface reflection depend on the refractive indices of the surrounding materials for which we used* $n_{glass} = 1.45$ *and* $n_{air} = 1.0$.

over 18 full periods of $\Delta\phi = 0 \ldots 36\pi$. Further details on the characterization of the light source can be found in Appendix B.1.

The multiple scattering experiment is conducted by focusing the nonclassical light onto either the front surface or the back surface of the sample, cf. Fig. 2.4, to perform total transmission and total reflection measurements, respectively. The multiply scattered light is collected with a microscope objective ($NA = 0.63$). In the reflection geometry the contributions from single-scattering events are avoided by illuminating the sample surface under a steep angle. The multiple scattering samples consist of titanium dioxide that has been grounded into strongly scattering particles with a typical size of 200 nm. The thicknesses of the samples range between $L = 6 - 20\,\mu$m.

The ensemble-averaged total intensity transmission coefficient $\overline{T}$ is the characteristic parameter of the multiple scattering medium entering in the quantum optics theory (Eqs. (2.17)-(2.19)). Independent measurements of $\overline{T}$ for all fab-

ricated samples are therefore important. $\overline{T}$ was obtained experimentally using an integrating sphere with two entrance ports. A detector was mounted on one port and the samples on the second port. We record the total transmitted intensity I_T through a sample and the light intensity I_0 without the sample, and extract the total sample transmission T. To obtain the ensemble-averaged total transmission $\overline{T} = I_{\mathrm{T}}/I_0$ we have measured at 6 different positions on the sample. Small changes in the transmission coefficients were observed depending on which of the two sample surfaces were illuminated, since they are surrounded by different dielectric media (glass and air, respectively). The inverse of the total transmission depending on the sample thickness is shown in Fig. 2.6a, b. Fitting the experimental data of the inverse total transmission measured for both sample surfaces with theory (Eq. (2.3)), we estimate a transport mean free path of $\ell = (0.9 \pm 0.3)\,\mu$m and extrapolation lengths of $z_{e1} = (4.3 \pm 0.3)\,\mu$m and $z_{e2} = (4.6 \pm 0.3)\,\mu$m, respectively. Note that $\ell \ll L$, which confirms that the multiple scattering samples are in the diffusive regime. The effective refractive index of the samples can be obtained from the extrapolation lengths [35] and is $n = 2.0 \pm 0.4$. The average number of scattering events taking place in the multiple scattering process is given by $N \propto (L_{\mathrm{eff}}/\ell)^2$ where $L_{\mathrm{eff}} = L + z_{e1} + z_{e2}$ is the effective sample thickness including interface effects [43]. For our samples we estimate $N \approx 300 - 1000$ scattering events depending on the sample thickness quantifying the complexity of the multiple scattering process.

2.4.2 Photon fluctuations of multiply scattered light

Figure 2.7a shows the measured photon fluctuations, recorded in reflection, for squeezed light illumination of a multiple scattering medium with a thickness of $L = 20\,\mu$m (black circles). The data are taken at a specific sample position, representing a single realization of disorder. The reflected photon fluctuations from multiply scattered photons differ clearly from the classical limit ($F_R(\omega, \Delta\omega) = 1$). In particular, we record both, classical and nonclassical photon fluctuations depending on $\Delta\phi$. Using the total transmission configuration of our setup allows us to measure transmitted photon fluctuations through a multiple scattering medium. The results are exemplary shown for $L = 6\,\mu$m in Fig. 2.7b. The variations in the transmitted photon fluctuations are smaller than in the reflection geometry. This fact originates from a higher reflection

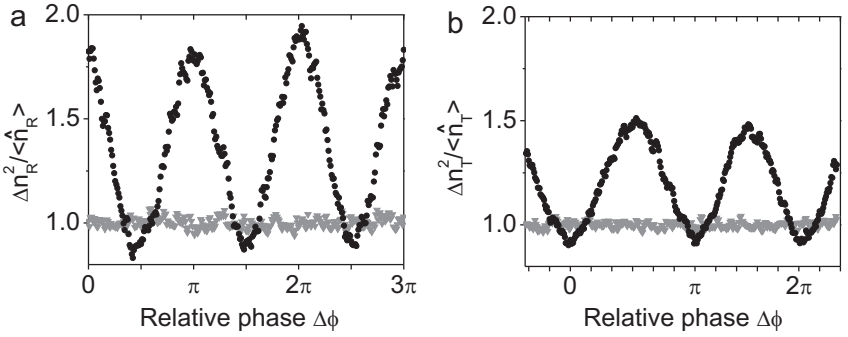

Figure 2.7: Measured photon fluctuations after multiple scattering recorded in **a**, *reflection geometry ($L = 20\,\mu$m) and* **b**, *transmission geometry ($L = 6\,\mu$m), respectively. The photon fluctuations of the total reflection for a squeezed light source (black circles) and the classical limit (gray triangles). Depending on the phase of a displacement beam, photon fluctuations below or above the classical limit are detected.*

than transmission of our samples and is especially pronounced in the variance in the photon fluctuations since they scale with the square of the transmission and reflection coefficients, respectively (cf. Eqs. (2.17) and (2.18)).

In order to compare the experiment with theory, we have to perform an ensemble average over different realizations of disorder. First, we tune the relative angle $\Delta\phi$ over 18 full periods ($0 \ldots 36\pi$) at a single sample position. All data that are multiple of $\Delta\phi + 2N\,\pi$ correspond to the same incident quantum state of light and can be averaged to account for any instabilities of the light source. The statistical ensemble average is obtained by repeating the procedure for six different sample positions. Figure 2.8 shows the transmitted, ensemble-averaged photon fluctuations depending on the incident quantum state of light for $L = 6\,\mu$m. The photon fluctuations are found to be linear dependent on the Fano factor of the light source, $F_a(\omega, \Delta\omega)$, which is in perfect agreement with the quantum theory of multiple scattering. Starting from Eq. (2.17), we substitute $\overline{\langle \hat{n}_T(\omega, \Delta\omega)\rangle}$ by $\eta\overline{T}\langle \hat{n}_a(\omega, \Delta\omega)\rangle$ and obtain the experimentally observed linear dependence in the diffusive regime $\overline{F_T(\omega, \Delta\omega)} = 1 + \eta\overline{T}(F_a(\omega, \Delta\omega) - 1)$, with $\overline{T}$ as a sample specific constant. Note that the plotted data in Fig. 2.8

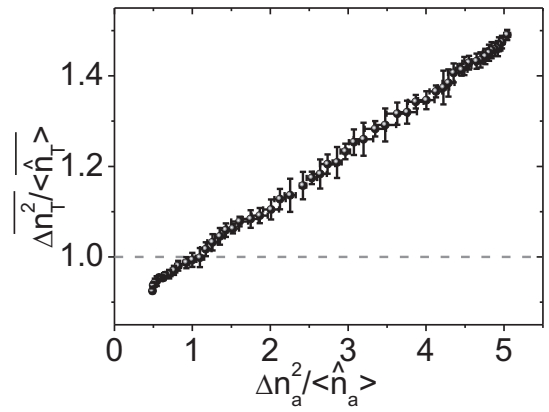

Figure 2.8: Ensemble-averaged transmitted photon photon fluctuations depending on the photon fluctuations of the incident light source. The sample thickness is $L = 6\,\mu m$ and the dashed line represents the classical limit. The error bars represents the standard deviation of the ensemble average. Furthermore they include the propagated error of the individual measurements, caused by instabilities in the light source.

represent the direct measurement and are not corrected by the collection efficiency, η, of the setup. For a nonclassical light source ($F_a(\omega, \Delta\omega) < 1$), the multiply scattered photons show reduced photon fluctuations below the classical limit. The reduction of $\overline{F_T(\omega, \Delta\omega)} < 1$ is the direct experimental proof that nonclassical properties of light survive the complex stochastic process of multiple scattering despite the common belief that quantum properties of light are fragile.

We have carried out a detailed investigation of the transport of nonclassical and classical photon fluctuations through the multiple scattering medium for a range of different sample thicknesses. Figure 2.9a and b display the detected photon fluctuations after multiple scattering plotted versus the sample thickness. Using light sources with classical fluctuations, the multiply scattered light always displays excess photon fluctuations corresponding to the classical regime (Fig. 2.9a). Nonclassical light allows entering the quantum regime where the photon fluctuations are reduced below the classical limit, see Fig. 2.9b. Our

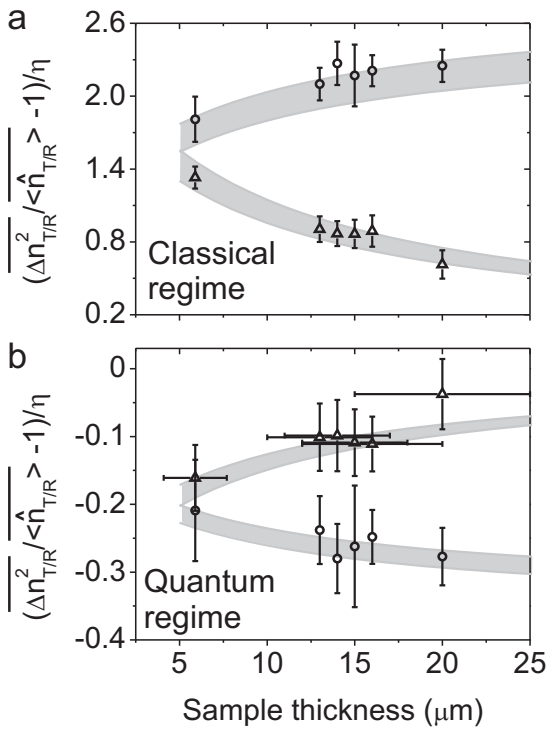

*Figure 2.9: Measured transmitted (triangles) and reflected (circles) photon fluctuations scaled to the collection efficiency η after multiple scattering of light with classical (**a**, $F_a(\omega, \Delta\omega) = 4.6$) and nonclassical (**b**, $F_a(\omega, \Delta\omega) = 0.52$) photon fluctuations versus sample thickness. The classical limit ($\overline{\Delta n^2_{T,R}(\omega, \Delta\omega)}/\overline{\langle \hat{n}_{T,R}(\omega, \Delta\omega)\rangle} = 1$) marks the boundary between the classical regime and the quantum regime. Every data point is obtained after ensemble averaging over six different sample positions. The shaded areas correspond to the theoretical predictions for the diffusive regime and incorporate the uncertainties in $F_a(\omega, \Delta\omega)$, ℓ, η, and the extrapolation lengths. The error bars on the sample thicknesses are only plotted once.*

experimental results can be compared to the predictions from the full quantum theory for multiple scattering of photons (Eqs. (2.17) and (2.18)). Excellent agreement between experiment and theory is apparent from Fig. 2.9 both in the classical and quantum regime. The shaded areas in the theoretical prediction

represent the uncertainties in the sample transmission, incident photon fluctuations, and collection efficiency. In transmission, we infer an average collection efficiency of 36 %, while the average value is slightly lower in the reflection measurements (34 %). Further details on η are discussed in Appendix B.4. It should be stressed that the comparison to theory requires no adjustable parameters, and only depends on measured parameters. It was suggested that random scattering of waves can enhance the maximum amount of information that can be transmitted, the so-called information capacity. This pioneering idea is nowadays widely implemented in wireless communication systems. The observed reduction in the photon fluctuations in the present experiment shows that the information capacity associated with the multiple scattering channels can be enhanced beyond the classical limit, as predicted theoretically [44].

2.5 Observation of spatial quantum correlations

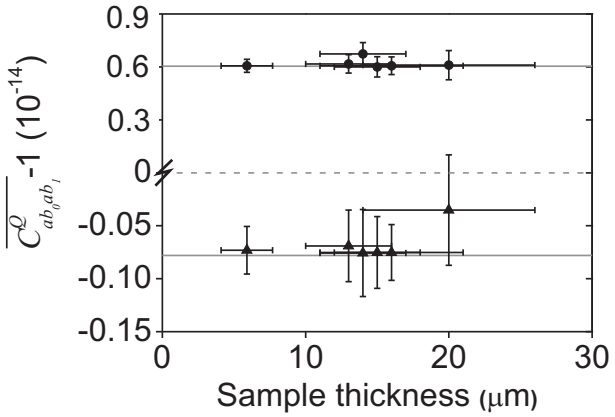

Figure 2.10: Measured spatial quantum correlation function versus sample thickness taken at an input power of $P = 120\mu W$ for classical ($F_a(\omega, \Delta\omega) = 4.6$, black points) and nonclassical ($F_a(\omega, \Delta\omega) = 0.52$, black triangles) photon fluctuations of the light source. The spatial quantum correlation function is ensemble-averaged over six data points and is found to be independent of the sample thickness which is in agreement with theory in the diffusive regime (horizontal lines).

The theory predicts that the multiply scattered photon fluctuations depend on two terms varying as $\overline{T}$ and $\overline{T}^2$, respectively, cf. Eqs. (2.17) and (2.18). The latter term is only observable for non vanishing spatial quantum correlations, i.e., the comparison between experiment and theory allows extracting the spatial quantum correlation function in the frequency-domain $\overline{C^Q_{ab_0ab_1}(\omega, \Delta\omega)}$ (Eq. (2.19)). We observe that the spatial quantum correlation function $\overline{C^Q_{ab_0ab_1}(\omega, \Delta\omega)}$ is directly accessible by measuring in addition to the photon fluctuations at the sideband frequency ω within the bandwidth $\Delta\omega$ also the detection efficiency, the mean number of photons entering the sample $\langle \tilde{n}_a(\omega, \Delta\omega) \rangle$, and the ensemble-averaged sample transmission coefficient. As sketched in Eqs. (2.23) - (2.25) it is possible to estimate the mean photon number from time domain measurements having fulfilled that $\Delta T = 1\,s$ exceeds all other time scales of the measurement process. From the power of the incident light, P,

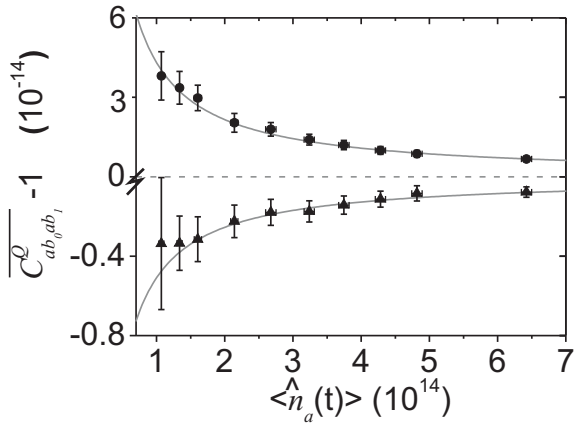

Figure 2.11: Measured spatial quantum correlation function, $\overline{C^Q_{ab_0ab_1}(\omega, \Delta\omega)}$, versus the mean photon flux $\langle \hat{n}_a(t) \rangle$ of the incident light beam. We varied the power between $P = 20 - 120\,\mu W$. For classical ($F_a(\omega, \Delta\omega) = 4.6$, black points) and nonclassical ($F_a = 0.52$, black triangles) photon fluctuations, positive and negative spatial correlations are observed, respectively. Every data point represents an average over three different positions on the sample of thickness $L = 6\ \mu m$. The curves are the theoretical predictions and the dashed line represents the uncorrelated case.

measured with a power meter, we calculate $\langle \hat{n}_{T,R}(t, \Delta T) \rangle = \frac{P\lambda}{hc}$ that we identify with $\overline{\langle \hat{n}_{T,R}(\omega, \delta\omega) \rangle}$. We note that in the total transmission experiments we perform a slightly different ensemble average, namely $\overline{\langle \hat{n}_{b_0}(\omega_x) \rangle \langle \hat{n}_{b_1}(\omega_y) \rangle}$ that equals the general definition in the diffusive regime $\overline{\langle \hat{n}_{b_0}(\omega_x) \rangle} \times \overline{\langle \hat{n}_{b_1}(\omega_y) \rangle}$ (Eq. (2.8)).

In the diffusive regime, the spatial quantum correlation function is predicted to be independent of the sample thickness (Eq. (2.15)). We confirm this behavior experimentally, by extracting $\overline{C^Q_{ab_0ab_1}(\omega, \Delta\omega)}$ for different sample thicknesses. During the measurement, the photon fluctuations and the average number of photons of the light source are kept constant. Figure 2.10 shows the spatial quantum correlation function for a classical light source and a nonclassical light source depending on sample thickness. We observe negative (positive) spatial correlations in the case where the transmitted photon fluctuations are

in the quantum (classical) regime. The recorded spatial quantum correlation function does not show any dependence on the sample thickness and shows an excellent agreement to theory. According to Eq. (2.15) the strength of the spatial quantum correlation is expected to increase when reducing the number of photons of the incident light. This pronounced behavior is clearly demonstrated in Fig. 2.11 and is in excellent agreement with theory. Controlling the power of the nonclassical light source provides an efficient way of tuning the strength of the spatial quantum correlations.

2.5.1 Spatial intensity correlations

In order to test the validity of the diffusive approximation in our experiments, we investigate experimentally the influence of spatial intensity correlations, $C^{(C)}_{ab_0a'b_1} = C^{(1)} + C^{(2)} + C^{(3)}$ (Eq. (2.4)), in strongly scattering media. In the diffusive regime, interference effects vanish after ensemble averaging over many different realizations of disorder. The multiply scattered light is represented by a superposition of many statistically independent partial waves. The probability distribution of the transmission coefficient in a angular direction b follows the Rayleigh statistics, $P(T_{ab}/\overline{T_{ab}}) = \exp(-T_{ab}/\overline{T_{ab}})$ [45, 46]. The total transmittance through the sample from direction a, $\overline{T_a} = \sum_b \overline{T_{ab}}$, is the sum over all outgoing directions. If the directions are uncorrelated T_a equals a convolution of N independent Rayleigh distributions that becomes a Gaussian distribution for large N. Experiments in strongly scattering media have revealed deviations from the Rayleigh statistics in a single outgoing direction [47] as well as non-Gaussian total transmission distributions [48]. The deviations from the diffusive transport are dominated by long-range intensity correlations that survive the ensemble average.

The long-range intensity correlation function for large conductances, g, is approximately given by

$$C^{(2)} \approx 1 + \frac{4}{3g},\ b \neq b'. \tag{2.26}$$

The angular difference between the two measured directions b and b' is much larger than the average speckle width to avoid any effects from the short-range correlation function, $C^{(1)}$. The dimensionless conductance, g, is obtained by

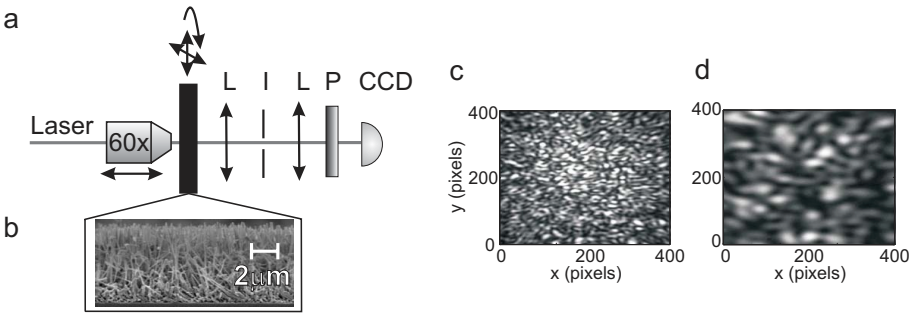

Figure 2.12: **a**, *Experimental setup to measure spatial intensity correlations. L: lens, I: iris (diameter* $500\,\mu m$*), P: polarizer, CCD: charged-coupled device camera.* **b**, *Scanning electron microscope image of a three-dimensional sample consisting of strongly scattering nano wires.* **c**, *Recorded volume speckle pattern with the CCD camera, illuminating the sample with a large beam diameter and,* **d**, *small beam diameter of* $1.9\,\mu m$*. The measured intensity is color-coded where white pixel represent high intensities and black pixel low intensities.*

summing the total transmission over all incident directions a,

$$g \equiv \sum_a \overline{T_a} \approx \frac{N\ell}{L}, \quad g \gg 1. \tag{2.27}$$

Based on conservation of energy it has been shown that for a finite number of modes, N, in a multiple scattering medium, the conductance is finite and the modes in transmission and reflection are correlated [49]. Neglecting diffusive broadening, the number of modes and hence independent speckles are determined by the area of the light that illuminates the sample $N = 2\pi^2\rho_0^2/\lambda^2$ [48], with ρ_0 being the Gaussian beam width of the light beam. For weak scattering in three-dimensional media N becomes very large and $4/3g$ can be neglected in Eq. 2.26. If a multiple scattering medium has a small conductance, the exponential distribution, $P(T_{ab}/\overline{T_{ab}})$, deviates from the Rayleigh statistics [50, 51]. To study the impact of $C^{(2)}$ on the quantum correlation function, a direct angular-resolved measurement is required. A possible experimental setup is discussed in Chapter 3. Here, we explore the long-range correlations in strongly scattering media by investigating the transmission probability distribution of multiply scattered light.

The experimental setup to measure deviations from Rayleigh statistics is shown Fig. 2.12a. The laser beam emerging from a Ti:Sapphire laser ($\lambda_0 = 780\,\mathrm{nm}$) is focussed on a strongly scattering sample that consists of disordered GaP nano wires with an effective refractive index $n = 2.2$, a transport mean free path of $\ell = 0.27\,\mu\mathrm{m}$, and a sample length $L = 4\,\mu\mathrm{m}$ [52] (Fig. 2.12b). Theses samples scatter light much stronger that titanium dioxide samples and thus, it is more likely to observe deviations from the diffusive regime. The multiply scattered light is collected with an aspheric lens, spatially filtered, and the collimated far field speckle pattern is imaged onto a CCD camera. Different realizations of disorder are recorded by rotating and translating the sample. It is essential to measure independent speckle pattern and therefore the speckle correlation length is estimated for each measurement. Hence, we determine the rotation and translation length of the sample using a motorized rotation and translation stage. In order to observe any deviations from diffusive light transport, the illumination area on the sample should be small to obtain a small number of modes. The beam waist at the focal point of the microscope objective is estimated to be $\rho_0 = 1.9\,\mu\mathrm{m}$.

Figures 2.12c and 2.12d show the recorded speckle pattern when the sample is not in the focus and is in the focus of the microscope objective, respectively. It is clearly visible that the number of modes, i.e., the number of speckles, reduces when the illumination area on the sample surface decreases. In accordance to Eq. (2.27) the conductance decreases simultaneously. To observe long-range correlations we focus tightly on the sample surface. Calculations show that diffusive broadening increases the beam width slightly and we expect to measure a minimum conductance of $g \approx 100$ corresponding to a maximum spatial intensity correlation function of $C^{(2)} = 1.014$. Since the average spatial width of the speckles is very large in Fig. 2.12d, we have to record many independent speckle pattern (sample displacement) to obtain a sufficient ensemble average and prove the statistical significance of eventual deviations from the diffusion transport. While recording the speckle pattern, the experimental conditions should be constant since any correlations induced by the experimental setup cause deviations from the Rayleigh statistics and $C^{(2)} = 1$, respectively.

The transmission probability distribution of a single speckle in the diffusive regime is plotted in Fig. 2.13a. Each pixel on the CCD camera (cf. Fig. 2.12c)

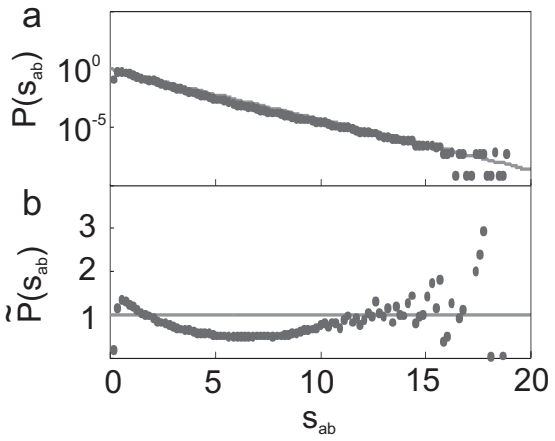

Figure 2.13: **a**, *Measured transmission probability distribution for a single speckle in the diffusive regime with* $s_{ab} = T_{ab}/\overline{T_{ab}}$. *The gray line represents the Rayleigh statistics.* **b**, *The probability distribution,* $\tilde{P}(s_{ab})$ *shows the same data as in* **a** *but normalized to the Rayleigh statistics,* $P(s_{ab}) = \exp(-s_{ab})$.

represents a transmission T_{ab}. In order to get a statistical ensemble average, we record 100 different speckle pattern. The average pixel intensity defines $\overline{T_{ab}}$. At a first glance, the experimental data follow an exponential decay, $\exp(-T_{ab}/\overline{T_{ab}})$ (gray line), that is predicted by the Rayleigh statistics. A normalization of the data to the Rayleigh statistics reveals deviations, presented in Fig. 2.13b. We observe fluctuations in the experimental transmission distribution which we attribute to the slightly nonlinear response of the CCD camera. Thus, for a weakly focussed light source onto a very strongly scattering sample as used here, we do not find significant deviations from the diffusive regime. Within the experimental accuracy, our experiment can therefore be approximated by the diffusion theory and the spatial quantum correlation function can be extracted from total transmission measurements. By replacing the CCD camera with an array of photo diodes (with a linear response), angular-resolved photon fluctuations could be investigated in quantum noise measurements. This would allow us to estimate the impact of classical intensity correlations such as $C^{(2)}$ on the spatial quantum correlation function.

2.6 Conclusion

Multiple scattering was found to induce infinite range spatial correlations that are of a purely quantum origin. A continuous-mode quantum theory was developed to describe multiple scattering in the realm of quantum optics. Using squeezed light source, the quantum nature of multiply scattered light was investigated by evaluating the variance in multiply scattered photon fluctuations. Both positive and negative spatial quantum correlations were observed when varying the quantum state incident to the multiple scattering medium, and the strength of the correlations was controlled by the number of photons. Our experimental results were in excellent agreement with the developed theory. A very interesting extension to this work would be to send two different quantum states of light inside a multiple scattering medium and to investigate predicted quantum interference that survive multiple scattering [53, 54].

Chapter 3

Photon Statistics in disordered media

3.1 Introduction

The photon statistic of a light source determines whether it is described to be classical or nonclassical. One method to study multiply scattered photon fluctuations is the quantum noise measurement, as discussed in Chapter 2. Alternatively, the arrival time of the individual photons can be recorded, leading to a photon counting statistic that determines the mean photon number and its variance in the time-domain [29]. So far, quantum properties of multiply scattered light have only been investigated by performing a spatial average over the entire volume speckle pattern. In order to measure spatial quantum correlations directly or to observe quantum interference of multiply scattered photons, it is essential to investigate the quantum nature of light for different angular directions separately.

This chapter concerns angular-resolved measurements to study photon counting statistics of multiply scattered light in a single optical speckle. Section 3.2 discusses the direct measurement of spatial photon correlations. This

is the spatial analogue to the Hanbury Brown and Twiss experiment [55] generalized to a multiple scattering setting. We perform a detailed study of the angular and temporal dependence of the photon correlation function. When interference survives the ensemble average, the light transport shows deviations from the diffusion theory. One example is the coherent backscattering of light [56, 57]. Constructive interference of counter-propagating light paths results in an enhanced backscattered intensity. For the direct backscattering direction, the multiply scattered light intensity is twice as high as expected from diffusive light transport. In Section 3.3, the backscattered photon fluctuations are investigated using angular-resolved photon counting statistics. The ensemble-averaged variance in the backscattered photon fluctuations that exhibit the same polarization as the light source (coherent backscattering) is much larger than the variance in backscattered photon fluctuations in the orthogonal polarization (diffusive transport). This enhancement is found to be larger than the corresponding enhancement of the coherently backscattered intensity. These experiments explore the complex interplay between interference effects in strongly scattering media and the quantum nature of light.

3.2 Angular-resolved photon-coincidence measurements

In Chapter 2, the spatial quantum correlation was extracted from total transmission noise measurements of multiply scattered light in the frequency domain. Here, we measure directly spatial time-correlations of photons that are induced by multiple scattering of light. Since we use exclusively a classical light source in the following experiments, we refer to this type of correlation as spatial photon correlations. In accordance with the definition in the frequency domain (Eq. (2.8)), we define the dimensionless spatial photon correlation function between two angular directions b_0 and b_1 as

$$\overline{C^{Q}_{b_0 b_1}(t,t',\Delta t)} = \frac{\overline{\langle : \hat{n}_{b_0}(t,\Delta t)\hat{n}_{b_1}(t',\Delta t) : \rangle}}{\overline{\langle \hat{n}_{b_0}(t,\Delta t)\rangle} \times \overline{\langle \hat{n}_{b_1}(t',\Delta t)\rangle}}. \tag{3.1}$$

The classical ensemble average of the stochastic process of multiple scattering is denoted by the bars. The normally ordered quantum mechanical expectation

value of the numerator represents the coincidence counts between two detectors within the time interval Δt and averaged over many time intervals. We define the flux operator $\hat{n}(t) = \hat{a}_b^\dagger(t)\hat{a}_b(t)$ (see Eq. (2.21)) that, when integrating $\int_t^{t+\Delta t} dt' \langle \hat{n}(t') \rangle$, we obtain the dimensionless mean photon number $\hat{n}_b(t, \Delta t)$ within the measurement time Δt [33]. We further consider a stationary light source whose statistical fluctuations do not change in time. The spatial correlation function therefore only depends on the time difference $\tau = t' - t$ of the measurement between b_0 and b_1 and the time argument t can be neglected. Similar to measurements in the frequency-domain,[28, 30] the quantum properties of light can be probed in the time-domain. A single photon counting detector records n photons within a time interval Δt. The mean number of photons $\langle \hat{n}(\Delta t) \rangle$ as well as the variance in the photon number fluctuations, $\Delta n^2(\Delta t) = \langle \hat{n}^2(\Delta t) \rangle - \langle \hat{n}(\Delta t) \rangle^2$, are obtained by counting photons in many time intervals Δt. Figure 3.1 plots a stream of photons that is recorded by a single photon counting detector. Both, the average number of photons and the variance in the photon fluctuations are dependent on Δt. The Fano factor, $F(\Delta t) \equiv \Delta n^2(\Delta t)/\langle \hat{n}(\Delta t) \rangle$ illustrates that it is possible to probe different quantum states of light by changing the time interval Δt (see Appendix B.5). In the following this property is exploited to investigate the quantum nature of multiple scattering.

Utilizing the continuous mode quantum theory to relate the spatial photon correlation function to the annihilation and creation operators of the light source. Having an incident light wave in direction a, we get

$$\overline{C^Q_{ab_0ab_1}(\tau, \Delta t)} = \frac{\langle : \hat{n}_a(\Delta t)\hat{n}_a(\tau, \Delta t) : \rangle}{\langle \hat{n}_a(\Delta t) \rangle^2} \times \overline{C^{(C)}_{ab_0ab_1}}. \tag{3.2}$$

The first term on the right side represents the second order coherence function of the light source, $g^{(2)}(\tau)$, while the latter factor is due to spatial intensity correlations (Eq. (2.4)). For the selected case of a thermal light source we have [42]

$$\overline{C^Q_{ab_0ab_1}(\tau)} = \left[1 + \exp\left(-\pi(\tau/\tau_c)^2\right)\right] \times \overline{C^{(C)}_{ab_0ab_1}}, \tag{3.3}$$

with τ_c being the coherence time. Here, Δt is chosen in such a way that the Fano factor of the light source, $F_a(\Delta t)$, reflects the characteristics of thermal light, $F_a(\Delta t) = \langle \hat{n}_a(\Delta t) \rangle + 1$. In contrast photons of a coherent light source are

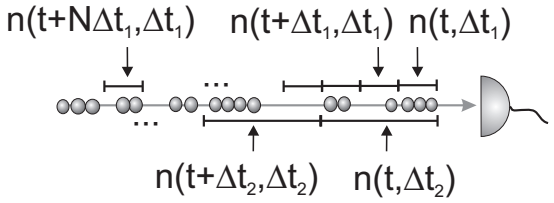

Figure 3.1: Photon counting detection in the time-domain. A photon detector records the arrival times of photons (spheres) from a light source. The photon stream can be divided in N equidistant time intervals, Δt_1, to determine the mean photon number $\langle \hat{n}(\Delta t_1) \rangle$. Changing the interval length from Δt_1 to Δt_2 results in a different average photon number and in a different variance in the photon fluctuations.

uncorrelated ($F_a(\Delta t) = 1$) and the angular photon correlation function equals the classical intensity correlation function.

3.2.1 Experimental setup

The experimental setup is displayed in Fig. 3.2. As a light source we use a continuous wave Ti:Sapphire laser ($\lambda = 780\,\mathrm{nm}$) that is focused onto a ground glass plate. Super-Poissonian photon statistics are obtained by a superimposing coherent beams with random amplitudes and phases. For that purpose the ground glass plate is rotated slowly and only fraction of the transmitted light is collected using an iris with an aperture that is smaller than the average speckle size of the scattered light generated by the ground glass plate [58, 59]. The collimated light beam is then focussed onto the front surface of a multiple scattering medium consisting of titanium dioxide nano-particles[1] ($L = 6.3 \pm 0.2\,\mu\mathrm{m}$, $\ell = 0.9 \pm 0.1\,\mu\mathrm{m}$ [60]). Two single photon counting detectors (D_1, D_2) are positioned behind the sample to record multiply scattered photons at different angular directions. Detector D_1 can be rotated to vary the angle $\Delta\Theta$ between both detectors. We avoid the contribution from ballistic propagation of light through the multiple scattering medium by only collecting light polarized perpendicular to the incident light polarization.

[1] Different sample batch as in Chapter 2.4 but same fabrication process.

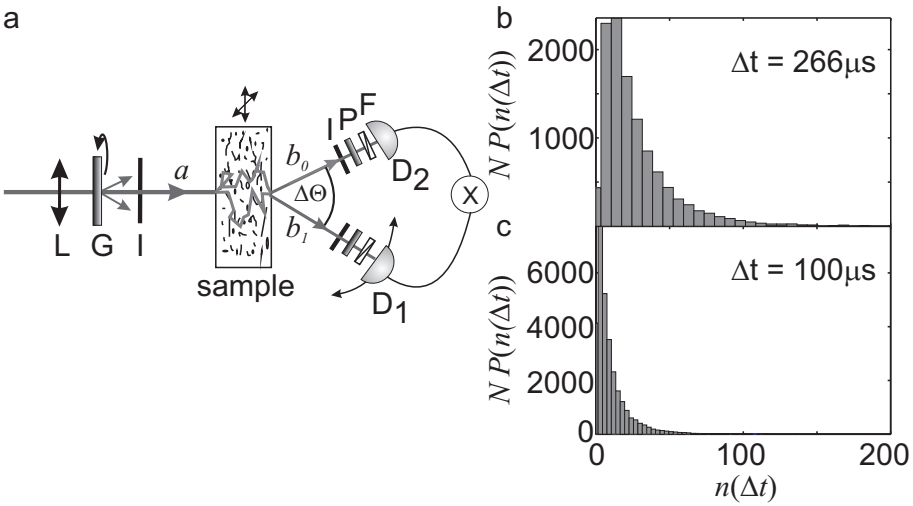

Figure 3.2: **a**, *Sketch of the experimental setup. L: lens, G: ground glass plate that can be rotated as indicated by the arrow, I: iris, P: polarizer, F:* 10 *nm interference filter,* $\Delta\Theta$*: angle between detector* D_1 *and* D_2*; a: incident light channel;* b_0, b_1*: exit light channels. To probe different realizations of disorder the sample can be displaced. Optional a neutral density filter (OD) with an optical density of of OD=* $2 \cdot 10^{-5}$ *can be inserted in front of detector* D_1 *to attenuate the light beam.* **b**, *Recorded photon counting distribution,* $P(n(\Delta t))$*, of the light source on detector* D_1 *after the neutral density filter using a time interval of* $\Delta t = 266\,\mu s$ *to bin the measured photons. The photoncounts* $n(\Delta t)$ *have been measured* N *times.* **c**, *Same as measurement as in* **b** *using a time interval of* $\Delta t = 100\,\mu s$*.*

In order to characterize the quantum properties of the light source, we measure the photon statistics, i.e., we create a histogram from the number of photons, $\hat{n}_a(\Delta t)$, that are detected within Δt. This distribution determines directly the variance in the photon fluctuations. To this end, the sample is removed and D_1 is positioned in the light beam emerging from the source. The light source has been attenuated with a neutral density filter to protect the photon counting detector. Figure 3.2b displays the measured super-Poissonian photon statistics for $\Delta t = 266\,\mu$s yielding $F_{\mathrm{OD}}(\Delta t) = \langle \hat{n}_{\mathrm{OD}}(\Delta t) \rangle = 29$. The properties the light source without attenuation is calculated using the sepa-

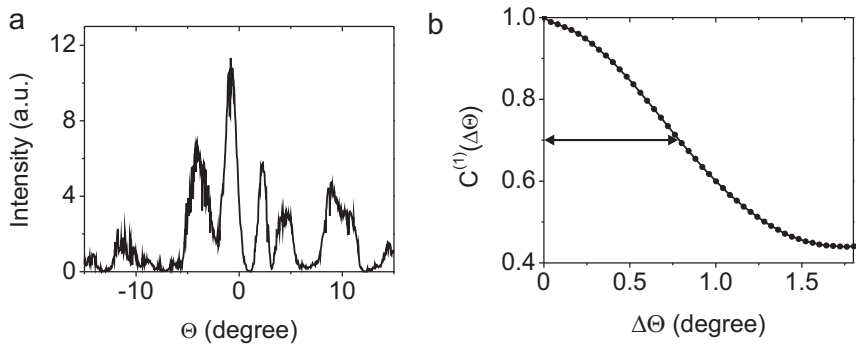

Figure 3.3: **a**, *Speckle pattern that was obtained by rotating detector D_1 behind the sample.* **b**, *Angular intensity correlation function $C^{(1)}(\Delta\Theta)$ of the speckle pattern, shown in a. The full width at half maximum (straight line) represents the average width of the speckles.*

rately measured optical density, OD$= 2 \cdot 10^{-5}$, of the filter. We obtain a Fano factor of $F_a(\Delta t) \equiv (F_{\mathrm{OD}}(\Delta t) - 1)/\mathrm{OD} + 1 = 14 \cdot 10^5$ and a mean number of photons of $\langle \hat{n}_a(\Delta t) \rangle = \langle \hat{n}_{\mathrm{OD}}(\Delta t) \rangle / \mathrm{OD} = 14 \cdot 10^5$. Hence, the light source incident on the multiple scattering medium exhibits the properties of thermal light and is called Gaussian radiation source.[58] By varying Δt, the photon counting distribution changes. Figure 3.2c shows exemplarily the measured (attenuated) photon statistics for $\Delta t = 100\mu$s with a corresponding Fano factor of $F_{\mathrm{OD}}(\Delta t) = 17$ and mean number of photons of $\langle \hat{n}_{\mathrm{OD}}(\Delta t) \rangle / \mathrm{OD} = 10$. By removing the ground glass plate in the incident light beam, we measure $F_{\mathrm{OD}}(\Delta t) = 1$, independent of Δt, reflecting the coherent state of the continuous wave Ti:Sapphire laser.

We ensue to probe different speckles, i.e. independent output modes b_0 and b_1, by determining the average speckle width, α. A typical intensity speckle pattern of multiply scattered light is shown in Fig. 3.3a, recorded by moving detector D_1 behind the sample. From the angular-resolved speckle pattern we calculate the intensity correlation function $C^{(1)}(\Delta\Theta)$ [61]

$$C^{(1)}(\Delta\Theta) \equiv \int d\Theta \frac{\overline{\delta I(\Theta)\delta I(\Theta + \Delta\Theta)}}{\overline{\sigma(\Delta\Theta)} \times \overline{\sigma(\Theta + \Delta\Theta)}}, \tag{3.4}$$

where $\delta I(\Theta) = I(\Theta) - \overline{I(\Theta)}$ denotes the intensity fluctuations and $\sigma(\Delta\Theta) =$

$\overline{I(\Theta)^2} - \overline{I(\Theta)}^2$ is the variance of the intensity distributions. The full width at half maximum of $C^{(1)}(\Delta\Theta)$ is determined by the average speckle width that is calculated to be $\alpha = 1.5°$ (Fig. 3.3b). To ensure light collection from only a single speckle spot on each detector, corresponding to a single output mode, the apertures in front of the photon counting detectors have to be adjusted accordingly. In the following experiments, the angle between both detectors, $\Delta\Theta$, is chosen to be much larger than the width of a single speckle. Thereby independent output modes are probed and the $C^{(1)}(\Delta\Theta)$ correlation function does not contribute to the photon correlation function.

3.2.2 Angular and temporal dependence of the spatial photon correlation function

We measure the spatial photon correlation function (Eq. (3.1)) between two angles by recording simultaneously the ensemble-averaged number of photons in each direction ($\overline{\langle \hat{n}_{b_0}(\Delta t)\rangle}$, $\overline{\langle \hat{n}_{b_1}(\Delta t)\rangle}$) as well as the ensemble-averaged photon-coincidences between detector D_1 and D_2 ($\overline{\langle : \hat{n}_{b_0}(\Delta t)\hat{n}_{b_1}(\tau, \Delta t) : \rangle}$). The ensemble average is achieved after repeating the measurement at 200 different sample positions (indicated by the arrows at the sample in Fig. 3.2) corresponding to different realizations of disorder. The experimental configuration further allows us to measure independently classical intensity correlations $\overline{C^{(C)}_{ab_0ab_1}}$ (cf. Eq. (2.4)). For this purpose we record the ensemble-averaged number of photons $\overline{\langle \hat{n}_b(\Delta t)\rangle}$ on each detector and the joint ensemble average $\overline{\langle \hat{n}_{b_0}(\Delta t)\rangle\langle \hat{n}_{b_1}(\Delta t)\rangle}$ on both detectors.

First, the spatial photon correlation function is studied depending on the average number of photons and Fano factor of the incident light field. Figure 3.4 shows the measured ensemble-averaged spatial photon correlation function between detector D_1 and D_2 that is induced by multiple scattering of light (see Eq. (3.1)). The quantum properties of the light source are changed by varying Δt. For light sources with super-Poissonian probability distributions ($F_a(\Delta t) > 1$) we measure a decrease of $\overline{C^{Q}_{ab_0ab_1}(0, \Delta t)}$ with increasing number of photons and slower increasing Fano factor (gray data points). On the contrary, we observe that $\overline{C^{Q}_{ab_0ab_1}(0, \Delta t)}$ is independent of the incident number of photons for a coherent light source, as obtained by removing the ground glass plate

(black data points). In order to compare the experimental data with theory (Eq. (3.3)) we measure, in addition to $\overline{C^{Q}_{ab_0ab_1}(0,\Delta t)}$, also the intensity correlations induced by the multiple scattering medium. Afterwards, the Fano Factor of the light source is determined with detector D_1 as a function of Δt by removing the sample. The experimental data are found to be in good agreement with theory without any adjustable fitting parameters. The slightly smaller predicted values of the angular photon correlations (gray line in Fig. 3.4) are attributed to variations in the rotation speed of the ground glass plate over time, which influence the Fano factor. For very low number of incident photons we observe a saturation at $\overline{C^{Q}_{ab_0ab_1}(0,\Delta t)} \approx 2.9$ corresponding to very short time intervals Δt. This effect we attribute to the properties of the light source. The phase of an otherwise coherent light source is scrambled by the rotating glass plate imposing an upper limit on the ratio $(F_a(\Delta t)-1)/\langle \hat{n}_a(\Delta t)\rangle$ and the correlations, respectively, for times Δt smaller than the time scale on which the phase distortion occurs. These results demonstrate that the quantum aspects of multiple scattered light depend sensitively on the investigated timescales, even though samples with static disorder are probed. Thus, the strength of the angular photon correlation function can be controlled by varying Δt and the number of photons and the Fano factor of the light source, respectively, illuminating the multiple scattering medium.

In the diffusive regime, spatial photon correlations are predicted to be infinite in range, i.e., to be independent of the exit direction. This holds if the distance between the two coincidence detectors is much larger than the average speckle width and the classical intensity correlation function $C^{(1)}(\Delta\Theta)$ can be neglected. Figure 3.5a plots the spatial photon correlation function as a function of the angle $\Delta\Theta$ between the detector D_1 and D_2 for a coherent and for a Gaussian radiation source. The error bars in $\overline{C^{Q}_{ab_0ab_1}(0,\Delta t)}$ arise mainly from uncertainties in the classical intensity correlations caused by a finite number of disorder realizations contributing to the ensemble average. In good agreement with theory we do not observe a dependence of the photon correlations on the angle between the direction of multiply scattered light confirming that the spatial photon correlation function is infinite in range.

In order to investigate the temporal dependence of the spatial photon correlations, a relative time difference, τ, is induced between detector D_1 and D_2.

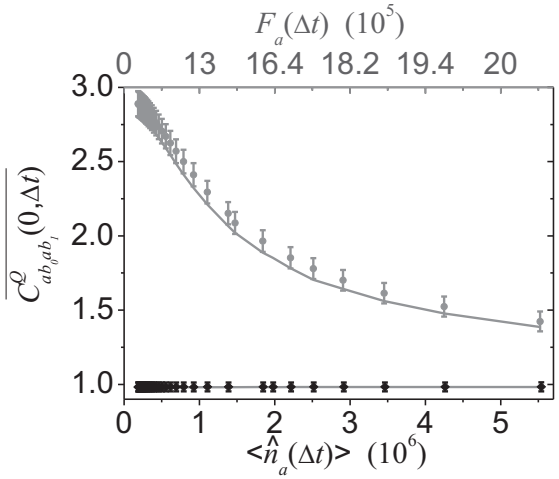

Figure 3.4: Photon correlation function $\overline{C^Q_{ab_0ab_1}(0,\Delta t)}$ depending on $\langle \hat{n}_a(\Delta t) \rangle$ and $F_a(\Delta t)$ (top axis) that is measured by slowly rotating the ground glass plate of the light source (gray circles). Measurements for a coherent state show that $\overline{C^Q_{ab_0ab_1}(0,\Delta t)}$ is independent of $\langle \hat{n}_a(\Delta t) \rangle$ (black squares, $F_a(\Delta t) = 1$)). The theoretical predictions contain no free fitting parameters (solid curves).

Figure 3.5b presents the spatial photon correlation function depending on τ using a Gaussian radiation source. As the time difference increases, a clear decay of $\overline{C^Q_{ab_0ab_1}(\tau,\Delta t)}$ is observed. Fitting the experimental results with theory (Eq. (3.3)), the coherence time of the Gaussian radiation source is determined to be $\tau_c = 750\,\mu$s. The coherence time describes the dephasing of a light source, i.e. the average time interval between phase distortion fluctuations of the light source. Only coherence times of the light source can be resolved that are larger than Δt, i.e., the experimentally measured photon statistic does not contain information about photon fluctuations on shorter timescales. As $\tau_c > \Delta t$ we resolve the coherence time of our Gaussian radiation source. The magnitude of spatial intensity correlation function does not exhibit any time dependence. Thus, the time response of $\overline{C^Q_{ab_0ab_1}(\tau,\Delta t)}$ only originates from the quantum properties of the light source, namely a temporal bunching of photons. τ_c is therefore a property of the light source that survives the complex process of multiple scattering of light confirming that there exists quantum properties that are robust against disorder. For comparison, the temporal dependence

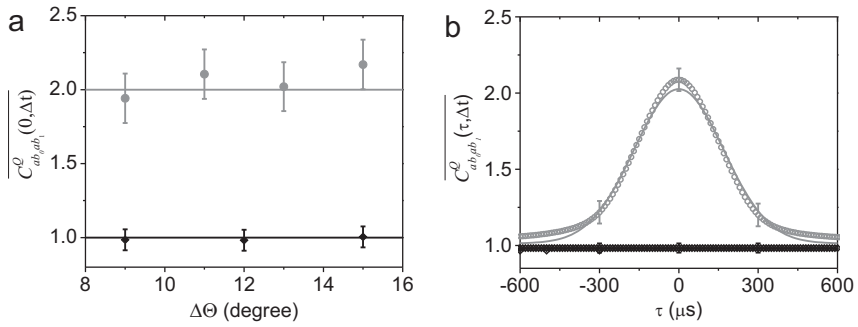

Figure 3.5: **a**, *Angular dependence of* $\overline{C^{Q}_{ab_0ab_1}(0,\Delta t)}$ *for a coherent light source (black squares) and a Gaussian radiation source (gray circles). Detector* D_1 *is rotated behind the sample to change* $\Delta\Theta$*. The straight lines are the theoretical predictions assuming that the classical intensity correlations equal to unity.* **b**, *Measured temporal dependence of the spatial photon correlation function for a Gaussian radiation source (gray circles) and a coherent light source (black squares), plotted with representative selected error bars. The straight gray line is a fit to the data with the coherence time as a free parameter. The black line represents the theory for a coherent light source.*

of the spatial photon correlation function is investigated for a coherent light source, too (Fig. 3.5b). We find a good agreement between experiment and theory, which predicts that the spatial photon correlation function is independent of τ and equals unity for a coherent light source.

3.3 Quantum properties of light in the coherent backscattering cone

The second part of this chapter is devoted to the quantum properties of multiply scattered light in the realm of coherent backscattering. Coherent backscattering arises from constructive interference of counter-propagating waves, as illustrated in Fig. 3.6a. A plane wave enters a disordered medium and is multiply scattered. During the propagation through the medium the wave splits

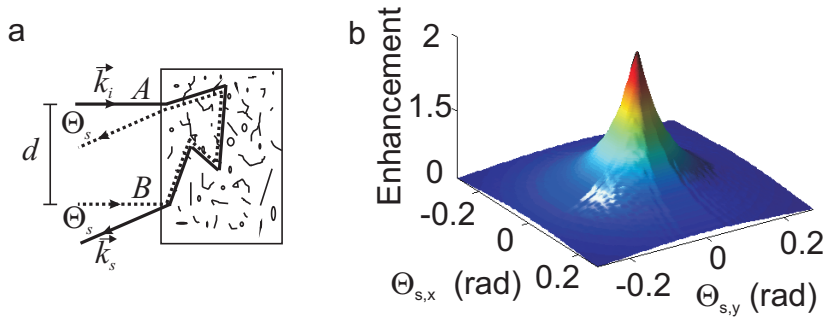

Figure 3.6: **a**, *Illustration of coherent backscattering. An incident plane wave (wave vector $\vec{k}_i$) is multiply scattered inside a disordered medium and exits the medium with a wave vector $\vec{k}_s$. For each random path (solid curve) exists a counter-propagating path undergoing the scattering events in a time-reversed order (dashed curve). The path length difference depends on the distance d and the scattering angle Θ_s. The coherent backscattering cone arises after summing over all path contributions by performing an ensemble average.* **b**, *Simulation of the coherent backscattering cone as a function of the scattering angle in x and y direction. The parameter used for the simulation are $|\vec{k}|\ell = 7.4$ and $\varepsilon = 2$ (see Appendix C.3).*

up in a multitude of different paths. The solid curve in Fig. 3.6a depicts one possible path where the wave enters at position A and exits the medium after many scattering events at position B. The angle between the wave vector of the incident wave, $\vec{k}_i$, and the scattered wave, $\vec{k}_s$, determines the scattering angle Θ_s. Surprisingly, for each random path a counter-propagating path exists, i.e., a plane wave enters the medium at position B and is scattered in time-reversed order (dashed line). The counter-propagating wave exits the medium at A under the same angle Θ_s [62]. The path difference between the wave exiting at A and the wave exiting at B depends on Θ_s and the distance $d = \lambda_0 \cos\Theta_s$ between A and B inducing an angle-dependent interference pattern in the far field. In the case of exact backscattering ($\Theta_s = 0\,\text{mrad}$), all counter-propagating waves interfere constructively, independent on d. For increasing Θ_s the far field pattern depends strongly on d. Figure 3.6b illustrates a simulation of a coherent backscattering cone [63]. The backscattered intensity for $\Theta_s = 0\,\text{mrad}$ is exactly twice as high as it is predicted by the diffusion

approximation corresponding to a maximum enhancement factor of $\varepsilon = 2$.

3.3.1 Experimental setup

The width of a coherent backscattering cone depends strongly on the scattering strength of the sample. Scattering is most pronounced when a large change in the refractive index occurs over length scales that are comparable to the wavelength of light. We have studied macroporous, single-crystalline gallium phosphide (GaP) samples with a refractive index of $n = 3.3$ and negligible absorption for light around $\lambda = 800\,\mathrm{nm}$. The thickness of the sample and the size of the voids can be controlled by electrochemical etching [64].

The experimental setup used to measure coherent backscattering is presented in Fig. 3.7. As a light source ($\lambda = 780\,\mathrm{nm}$) we either use a Ti:Sapphire laser or a spontaneous parametric down-conversion source (discussed below). The collimated light beam is directed onto a multiple scattering medium using a beam splitter. The backscattered photons from the sample, that are transmitted through the beam splitter, can be detected in an angular-resolved measurement within a backscattering range of $\Theta_s = -200\,\mathrm{mrad} \ldots 200\,\mathrm{mrad}$. The angular resolution, $\Delta\Theta_s$, is varied by changing the iris aperture in front of detector D_2. The angle-dependent transmission through the beam splitter has been measured independently. This allows us to account for losses at the beam splitter and deduce the variance in the photon fluctuations directly at the sample surface. The statistical ensemble average over different realization of disorder is achieved by slowly rotating the sample while recording the multiply scattered light. A challenge of coherent backscattering experiments is the contribution of single scattering events. They do not have a distinct time-reversed path and contribute to a background intensity that reduces the enhancement factor. The direct reflection can partly be avoided by tilting the sample relative to the incident light. The polarization of the multiply scattered light is selected with a polarizer.

In order to characterize our setup, the coherent backscattering cone of the GaP sample is studied with a reference setup that has an angular resolution of $\Delta\Theta_s = 5\,\mathrm{mrad}$ [60]. First, the ensemble averaged light intensity is measured depending on Θ_s, for the same polarization as the incident light beam

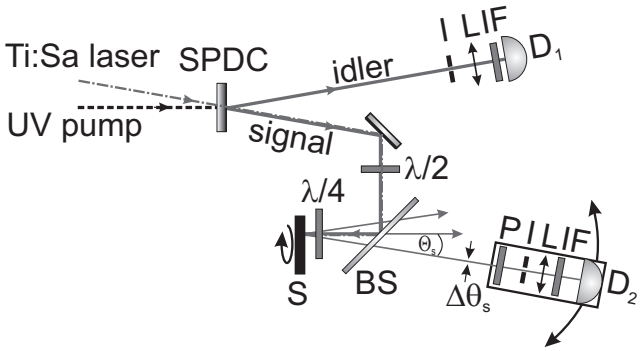

Figure 3.7: Scheme of the experimental setup. As a light source a Ti:Sapphire (Ti:Sa) laser (gray dashed-dotted line) and spontaneous parametric down-conversion (SPDC) light source can be used. The black dashed line illustrates the ultra violet (UV) pump laser beam to generate a SPDC photon pair (solid gray lines, signal and idler photon). The idler photon serves as a trigger and is detected with detector D_1 while the signal photon is used for the coherent backscattering experiment. The beam width of the light sources is approximately 2 mm. Detector D_2 records multiply scattered photons and can be rotated behind the sample. The rotation precision is 1.7 mrad. The thickness of the GaP sample is $L = 10.3\,\mu m$ with a sample reflection larger than 90 %. B: beam block, BS: 2 inch 50:50 beam splitter, I: iris, IF: 10 nm interference filter at $\lambda = 780\,nm$, L: lens, P: polarizer, S: sample that can be rotated. The elements placed directly in front of the detectors (I, L, IF) are positioned inside a tube that is mounted on the detector in order to suppress stray light from the surrounding.

$\overline{I_{\parallel}(\Theta_s)}$. Afterwards, the measurement is repeated for the orthogonal polarization, $\overline{I_{\perp}(\Theta_s)}$. The contribution of the coherent backscattering is visualized by plotting the ratio $\overline{I_{\parallel}(\Theta_s)}/\overline{I_{\perp}(\Theta_s)}$, as displayed in Fig. 3.8a. A fit to the data gives a transport mean free path of $\ell = 0.8\,\mu$m, an extrapolation length of $z_e = 0.7\,\mu$m, and an enhancement factor of $\varepsilon = 1.84$ (cf. Appendix C.3). The enhancement-factor is close to two proving that single scattering events and absorption do not affect the measurement significantly. The small rounding at $\Theta_s = 0$ mrad can be attributed to the experimental resolution. Next, the coherent backscattering cone is studied with our setup, as illustrated in

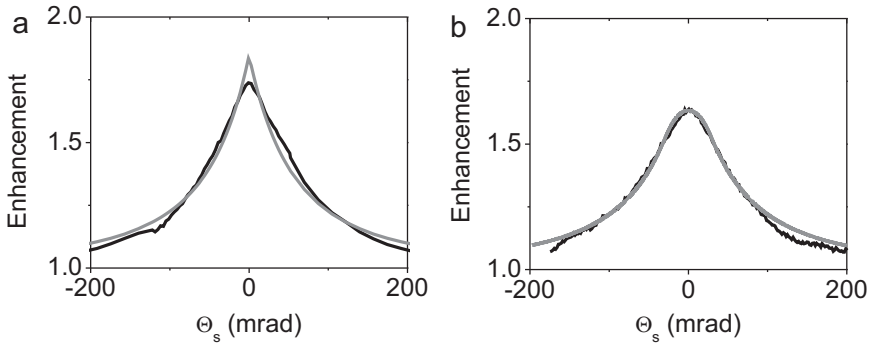

Figure 3.8: Coherent backscattering cone of a porous GaP sample at $\lambda = 780\,nm$. **a**, *Measured in a reference setup and,* **b**, *in the setup shown in Fig. 3.7 using a continuous wave Ti:Sapphire laser. The gray curve in the left panel is a fit to the experimental data. The obtained fitting parameters are used to calculate the gray curve shown in right panel. The curve does not contain any adjustable parameter and is determined by the angular resolution of* $\Delta\Theta_s = 60\,mrad$ *of the setup.*

Fig. 3.7. As a light source, the Ti:Sapphire laser is used. For experiments in the few photon regime (discussed below), a low angular resolution is required to collect a sufficient amount of backscattered photons from different angles. Figure 3.8b displays the coherent backscattering cone, that has been measured with a resolution of $\Delta\Theta_s = 60\,\mathrm{mrad}$. We observe a rounding of the cone as compared to Fig. 3.8a. In order to model the experimental data, we apply an angular average to the fit-function of the reference measurements. The resulting function is plotted as a gray curve in Fig. 3.8b and in agreement with the experimental data proving the applicability of the setup.

In the following, two experiments are presented that investigate the quantum aspects of light in the realm of coherent backscattering. Section 3.3.2 focusses on the feasibility to perform multiple scattering experiments on the level of single photons. Section 3.3.3 discusses the measurement of angular-resolved photon statistics to characterize the variance in the photon number in the coherent backscattering cone.

3.3.2 Coherent backscattering in the few photon regime

Quantum entanglement [65] is a necessary basis for fundamental tests of quantum mechanics such as quantum interference [66] and for applications such as quantum cryptography [67] and quantum teleportation [18]. It describes correlations between quantum systems, for example in the polarization of two photons, that are much stronger than any classical correlation could be. An interesting question is now, whether it is possible to observe quantum correlations after one of the two photons undergoes a multiple scattering process. In the diffusive regime the polarization of light is scrambled and thus, the ensemble averaged polarization correlation between the photon pair vanishes. In the coherent backscattering cone, the polarization correlation between the two photons is expected to be dependent on the backscattering angle and higher than in the diffusive regime. Eventually, quantum correlated photons might be observable, even after the complex stochastic process of multiple scattering. The fundamental requirement to study the correlations is to detect the initially quantum correlated photon pairs after the multiple scattering process. Therefore, in the first approach we want to focus on the feasibility of a coherent backscattering experiment in the few photon regime and do not aim our attention on the generation of quantum correlated photons.

As a light source a spontaneous parametric down-conversion source is established that generates pairs of photons [68, 69, 70]. To initiate the spontaneous parametric down-conversion process, a femto-second pulsed laser ($\lambda = 390\,\mathrm{nm}$) pumps a nonlinear beta-barium borate crystal generating at maximum one photon pair per pulse ($\lambda = 780\,\mathrm{nm}$). One photon pair is composed of an idler photon and a signal photon with orthogonal polarizations. In the experiment, all idler photons are directed onto detector D_1 while the signal photons are directed onto the multiple scattering sample (Fig. 3.7). A characterization of the light source showed that 70.000 photon pairs are generated per second. Next, a photon-coincidence measurement between detector D_1 and D_2 is established to identify the backscattered signal photons. For that purpose, we record the number of backscattered photons during a measurement time of $T = 140\,\mathrm{s}$. After postprocessing the data, we find that the signal photons can clearly be distinguished from the background photons (see Appendix C.2). To improve

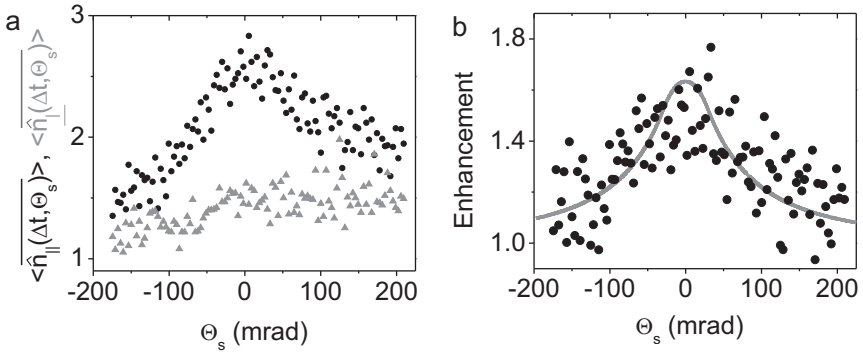

*Figure 3.9: Measurement of the coherent backscattering cone in the few photon regime using a triggered single photon source and an angular resolution of $\Delta\Theta_s = 60\,mrad$. **a**, Detected average photocounts ($\Delta t = 1\,s$) for the same polarization (black circles) and cross polarization (gray triangles) of the light source. **b**, Ratio of $\langle\overline{\hat{n}_{\parallel}(\Delta t,\Theta_s)}\rangle/\langle\overline{\hat{n}_{\perp}(\Delta t,\Theta_s)}\rangle$ to display the coherent backscattering cone (black circles). The theoretical prediction is represented by the gray curve used in Fig. 3.8b without any adjustable parameter.*

the experimental sensitivity, the photon-coincidence measurement is electronically gated using the pulses of the ultraviolet pump laser. For visibility, the measurement time is divided in time intervals of $\Delta t = 1\,\mathrm{s}$. The angular-resolved mean photon number, $\langle\hat{n}_{\parallel,\perp}(\Delta t,\Delta\Theta_s)\rangle$, of the backscattered signal photons for both orthogonal polarizations is presented in Figure 3.9a. The contribution of coherent backscattering is clearly observed in the conserved polarization, even on the level of only a few recorded photons per second. In average only two photons per angular position and second are detected highlighting the complexity of the measurement. The low collection efficiency originates mainly from the low number of backscattered photons in a limited angular range and the losses on the beam splitter. Figure 3.9b plots the corresponding coherent backscattering cone. In order to compare the coherent backscattering cone with the characterization measurement, the fit-function of Fig. 3.8b is plotted in Fig. 3.9b. A good agreement is obtained between theory and experimental data. The large fluctuations in the cone originate from the low average number of photons.

This experiment confirms that the established light source is sufficient to carry out a multiple scattering experiment in the coherent backscattering cone. The next possible experiment could be the investigation of nonclassical correlations. The idler and the signal photons could be spatially and temporally overlapped on a beam splitter creating quantum correlated photon pairs. The photons from one output port could be directed to detector D_1 and the photons from the second output port could be directed onto the sample and recorded with detector D_2. To detect a high initial correlation of the photon pairs, interference filter with a narrow bandwidth in front of the detectors and a good overlap of the photons on the beam spitter are essential. The rate of entangled photons reported with a Type-II beta-barium borate crystal (as is it used in our case) therefore reduces to only a few thousand counts per second [70]. This is not sufficient to conduct an angular-resolved multiple scattering experiment within a reasonable measurement time. A further drawback of this method is that the quantum correlation of the photons is only approximated by post-selecting half of the total quantum state when the photons leave via different output ports of the beam splitter [68]. Recently, a light source based on PPKTP nonlinear crystal was presented generating 273.000 pairs of inherently entangled photons [65]. The light source could be feasible for the investigation of polarization correlations in the coherent backscattering cone.

3.3.3 Measurement of the photon number fluctuations

Using classical (nonclassical) light sources, we demonstrated that the ensemble averaged Fano factor of multiply scattered light is reduced (enhanced) approaching one for very thick samples $\overline{F_{T,R}} \to 1$ (Eqs. (2.17) and (2.18), Chapter 2). This phenomenon originates from quantum vacuum fluctuations that are induced by multiple scattering.

Here, we report on an increase of the Fano factor of the multiply scattered light in the coherent backscattering cone, as compared to the Fano factor of the coherent light source (continuous wave Ti:Sapphire laser). Figure. 3.10 displays the Fano factor of the backscattered photon fluctuations that increases as Δt increases. We attribute the enhancement of the Fano factor to the rotation of the sample while recording the photon fluctuations. Measurements

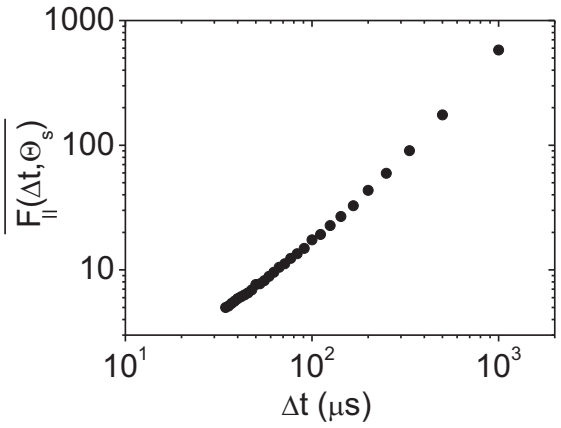

Figure 3.10: Measured Fano factor of the backscattered photon fluctuations for $\Theta_s = 0$ mrad depending on the time interval Δt. The sample is slowly rotated with a constant speed while recording the photon statistics.

of the backscattered photon fluctuations without rotating sample do not show an increase in the Fano factor supporting our assumption. When the sample rotates, the recorded photocounts of the backscattered light belong to different realizations of disorder. For short time intervals, only a few disorder realizations are averaged and we measure a Fano factor close to one. The Fano factor increases as Δt increases because multiply scattered photons from many different realizations of disorder contribute to the photon statistics. This shows a subtle but important point: it makes a different whether we evaluate the quantum mechanical expectation value first or the classical ensemble average first. In Section 3.2, $\overline{\langle \hat{n}(\Delta t) \rangle}$ has been measured whereas here we evaluate $\langle \overline{\hat{n}(\Delta t)} \rangle$.

Figure 3.11a plots the coherent backscattering cone of the average number of photons for two different time intervals. Both graphs are exactly on top of each other proving that the intensity coherent backscattering cone, is not affected by the sample rotation. The corresponding coherent backscattering cone of the photon fluctuations is displayed in Fig. 3.11b. For small time intervals the multiply scattered light is Poissonian distributed and the maximum enhancement factor, ε_n, of the variance in the photon fluctuations equals the intensity enhancement factor, ε. As the Fano factor increases, ε_n increases

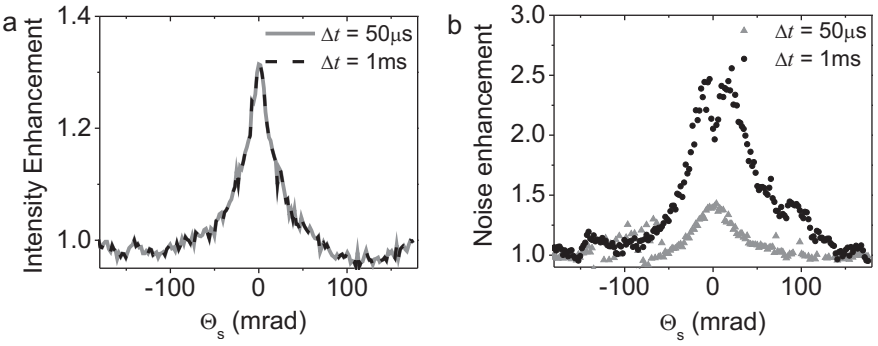

Figure 3.11: **a**, *Measured coherent backscattering cone of the backscattered intensity,* $\langle \overline{\hat{n}_{\parallel}(\Delta t, \Theta_s)} \rangle / \langle \overline{\hat{n}_{\perp}(\Delta t, \Theta_s)} \rangle$, *reconstructed from the detected average number of photons. The used GaP sample has a lower reflection and scattering strength than the one used in Fig. 3.8. Therefore, the backscattering cone appears more narrow and has a smaller intensity enhancement factor.* **b**, *Coherent backscattering cone obtained from the backscattered variance in the recorded photon fluctuations,* $\Delta\overline{n^2_{\parallel}(\Delta t, \Theta_s)} \,/\, \Delta\overline{\hat{n}^2_{\perp}(\Delta t, \Theta_s)}$. *The angular resolution in the present configuration is* $\Delta\theta = 9\,\mathrm{mrad}$. *The dip in the center of the coherent backscattering cone might be due to instabilities in the rotation speed of the sample. Further measurements showed dips at other randomly distributed angles.*

while ε does not change. This illustrates that the enhancement factor of the photon fluctuations depends clearly on the induced excess fluctuations in the multiply scattered light. Figure 3.12 plots the measured enhancement in the backscattered intensity and backscattered variance in the photon fluctuations depending on the Fano factor of the multiply scattered light. While the enhancement in the intensity does not change ($\varepsilon = 1.3$), we observe a continuous increase in the noise enhancement up to $\varepsilon_n = 2.6$. This value is much larger than the maximum enhancement of the backscattered intensity, $\varepsilon \leq 2$ proving that the quantum nature of multiply scattered light, explored by the photon fluctuations, behaves fundamentally different than the corresponding classical intensity properties.

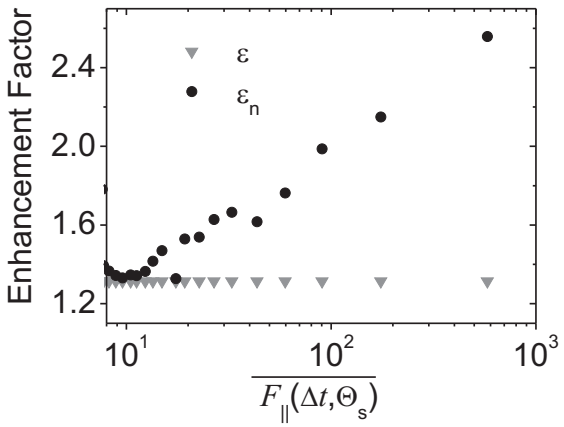

Figure 3.12: Enhancement factor of the photon fluctuations, ε_n (black circles), and the intensity, ε (gray triangles), as a function of the Fano factor of the multiply scattered light for $\Theta_s = 0\,mrad$. The Fano factor has been tuned by changing Δt.

3.4 Conclusion

We reported on angular-resolved measurements of photon counting statistics in multiple scattering media. In the diffusive regime, the spatial photon correlation function was found to be infinite in range, i.e., independent on the direction of propagation of multiply scattered photons. For a Gaussian radiation source, the strength of the spatial photon correlation function decreased as the time difference in the measurement between the detectors was increased. The experimental results were found to be in excellent agreement with the quantum theory of multiple scattering. In further experiments the quantum properties of light were investigated in the coherent backscattering regime. The coherent backscattering cone was studied in the few photon regime using a spontaneous parametric down-conversion light source. Using a bright coherent light source, the variance in the photon fluctuations was found to be altered by performing a statistical ensemble average over different realizations of disorder, while measuring the photon statistics in the coherent backscattering cone. In particular, the ensemble-averaged photon fluctuations depended on the scattering

angle and on the measured polarization. The variance in the photon fluctuations showed a coherent backscattering cone with enhancement factors larger than two representing the maximum value of the intensity enhancement factor. We believe that the experiments will inspire future work to develop a dynamic quantum theory in the realm of coherent backscattering. A spontaneous down-conversion source could be utilized to generate entangled photons and study the propagation of correlated photons in disordered media [31, 71].

Part II

Anderson localization of light

Chapter 4

Theory of one-dimensional Anderson localization

4.1 Introduction

In a disordered medium, light is multiply scattered along different directions. Due to interference of the different possible light paths inside the medium a complex spatial intensity distribution is generated. After ensemble averaging over all statistical realizations of disorder, interference effects are usually negligible and the light transport is approximated by diffusion theory. If multiple scattering is very pronounced wave interference can lead to new physics. The most prominent example is the formation of Anderson localization of light [21]. In this Anderson-localized regime interference causes large fluctuations in the spatial intensity profile while its ensemble-averaged envelope decays exponentially away from the light source [72, 73]. As a consequence, light is confined by disorder on a typical length scale called localization length, ξ [74]. Anderson localization was introduced by P. W. Anderson to explain localization of electrons in a random spatial potential [21] but has also been observed for, e.g., light [22, 17, 3], sound [23], and matter waves [24]. In three-dimensional systems a phase transition between diffusion and localization is expected when

the transport mean free path, i.e., the average distance between two scattering events, is comparable to the wave number [75]. In lower dimensions a crossover takes places from ballistic or diffusive light transport to localization. Anderson localization occurs in a one-dimensional multiple scattering medium, when the sample length, L, exceeds the localization length. Confirming Anderson localization remains a major challenge since any light losses in the system, such as leakage or absorption, lead to an exponential decay of the intensity profile as well [26, 27]. This problem has partly been circumvented by analyzing transmission distributions [76]. However, a method to measure the localization length, ξ, and the exponential loss length, l, is still lacking.

In this chapter, we provide a theoretical framework to calculate the statistical properties of Anderson localization in a one-dimensional disordered medium. We develop a method to distinguish unambiguously Anderson localization from losses by analyzing the linewidth distributions of Anderson-localized modes. In Section 4.2 Anderson localization is theoretically studied positioning emitters outside and inside a one-dimensional multiple scattering medium. The calculations are based on the transfer matrix theory [77] and a Green's function formalism [78, 79]. An important property of a disordered medium is its local density of states which is calculated analytically in the course of this chapter. Between different realizations of disorder, large fluctuations in the local density of states are observed originating from light scattering in close proximity to the emitter [80]. Section 4.4 discusses calculated linewidth distributions of Anderson-localized modes. These results form the basis to confirm Anderson localization experimentally in one-dimensional photonic structures, as demonstrated in Chapter 5 and 6.

4.2 Light scattering and light emission in disordered media

In the Rayleigh limit, light scattering on distant objects can be approximated by light rays. As the objects get closer, interfere effects dominate the scattering process and multiply scattered light forms a volume speckle pattern. In the calculations, light scattering needs to be included coherently from all ob-

jects. This is done using an electromagnetic propagator called Green's tensor, $\overrightarrow{G}(\vec{r}, \vec{r}_0)$. It describes the electric field at point z that originates from an oscillating point source at point z_0. This section discusses the analytical solution of the Green's function in a one-dimensional disordered medium by employing the transfer matrix theory.

4.2.1 Light transmission - transfer matrix theory

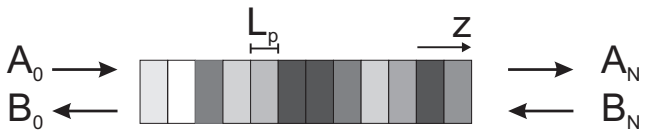

Figure 4.1: Sketch of a one-dimensional disordered structure where the gray tones represent different refractive indices. The structure consists of N stacked layers. The electric field amplitude of the incident plane wave is A_0, of the reflected plane wave is B_0, and of the transmitted plane wave is A_N. L_p determines the length of the individual layers.

Suppose an electromagnetic plane wave that travels in z-direction and approaches an interface to another medium in the xy-plane. At the interface the wave is partly reflected back and partly transmitted into the other medium. If a medium consists of several stacked interfaces in the xy-plane, the reflected waves from the first interface are again partly reflected at other interfaces resulting in multiple scattering and hence, constructive and destructive wave interference. The total reflection of such a medium is determined by the reflection at all interfaces and the thickness of the individual layers. Figure 4.1 illustrates a one-dimensional disordered medium with random variations in the refractive index, $n(z)$, along the z-direction. The wave vector, $\vec{k}$, always aims in the $\pm z$ direction while the electric and magnetic field vectors are perpendicular to the wave vector. Further, the electric and magnetic field are perpendicular to each other and continuous across an interface[1]. These boundary conditions are used to calculate the electric field reflection and transmission coefficients.

[1]The relative magnetic permeabilities are approximated to equal the magnetic vacuum permeability.

Thus, the electric field can everywhere be determined, once it is known at an initial position [81].

In a one-dimensional structure, the electric field is a superposition of a forward and a backward propagating plane wave with position dependent amplitudes, i.e.,

$$E(z) = A(z)e^{i\,\beta(z)\,z} + B(z)e^{-i\,\beta(z)\,z}. \tag{4.1}$$

$\beta(z) = k_0\,n(z)$ is the propagation constant with $k_0 = \omega/c$ as the wave number. If the electric field amplitude is known at position z_0 it can be calculated at another position $z > z_0$ via

$$\begin{pmatrix} A(z) \\ B(z) \end{pmatrix} = \underline{M} \begin{pmatrix} A(z_0) \\ B(z_0) \end{pmatrix}, \tag{4.2}$$

where $\underline{M}$ is the transfer matrix of the disordered medium between z_0 and z that is composed of m stacked layers. Assuming z_0 is located in layer j then $\underline{M}$ is given by $\underline{M} = \underline{M}_{j+m} \ldots \underline{M}_{j+1}\underline{M}_j$. The transfer matrix of a single layer with constant refractive index n_j and length L_p is the product of a propagation matrix, $\underline{M}_p$, and an interface matrix, $\underline{M}_I$,

$$\underline{M}_p = \begin{pmatrix} e^{-i\,\beta_j\,L_p} & 0 \\ 0 & e^{i\,\beta_j\,L_p} \end{pmatrix}, \quad \underline{M}_I = \frac{1}{t}\begin{pmatrix} 1 & r \\ r & 1 \end{pmatrix}, \tag{4.3}$$

with the electric field transmission and reflection coefficients

$$t = \frac{2\,n_j}{n_{j+1} + n_j}, \quad r = \frac{n_j - n_{j+1}}{n_{j+1} + n_j}. \tag{4.4}$$

The fraction of transmitted and reflected energy can be evaluated using, $I = 1/2\,n^2\,c\,|E|^2$. Having established the matrices of the individual layers, we can calculate the transmitted and reflected electric field of the entire structure. We assume an electric field incident on the structure from the left hand side with amplitudes A_0 and B_0 (Fig. 4.1). The medium consists of N layers. Once the electric field wave exits the structure on the right side of the structure, it is not reflected back, i.e., $B_N \equiv 0$. The electric field transmission coefficient through the medium, $t_N = A_N/A_0 = 1/\underline{M}(1,1)$, can be derived from the total transfer matrix of the medium and is given by the inverse of the transfer matrix element $\underline{M}(1,1)$ using $A_N \equiv 1$. The reflection of the medium, $r_N = B_0/A_0$ is

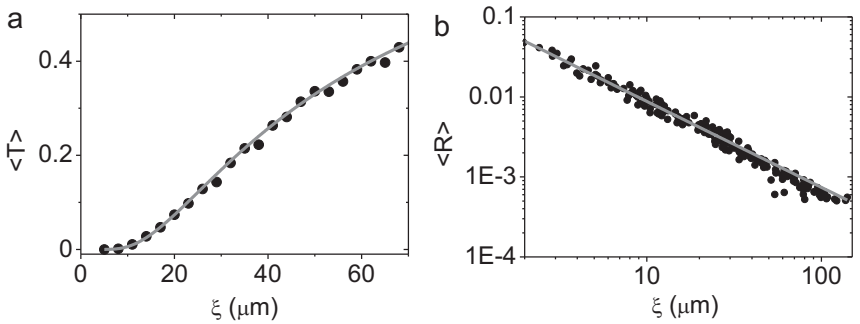

Figure 4.2: **a**, *Transmission, averaged over 10,000 different realizations of disorder, of one-dimensional structures (sample length $L = 100\,\mu m$) depending on the localization length. The gray curve plots $\langle T(\xi)\rangle = \exp(-L/2\xi)$.* ***b***, *Ensemble-averaged reflection between two unit cells (length $a = 260\,nm$) as a function of localization length. The gray curve represents a background-free powerlaw fit to the calculated data.*

calculated in the same way and we get $r_N = \underline{M}(2,1)/\underline{M}(1,1)$. After A_N and B_N is known, we can calculate the electric field at all positions.

The localization length of a one-dimensional medium is determined by the variations in the refractive indices among the layers. For the individual layers, the average refractive index, $\langle n\rangle$, is superimposed with a flat distribution within $\pm\Delta n$ around the average. For a fixed sample length, we calculate the intensity transmissions, T, for many different realizations of disorder. A single disorder realization is given by a specific arrangement of randomly varying refractive indices of the interfaces. A change of the refractive indices results in a new realization. The ensemble-averaged transmission, $\langle T(\xi)\rangle$, decays exponentially with the sample length and in one dimension it is directly related to ξ via [72]

$$\langle T(L)\rangle = e^{-L/2\xi}. \tag{4.5}$$

We can therefore relate the localization length to Δn and L_p by estimating the intensity transmission through many different disorder realizations $\langle T(L)\rangle$ depending on the sample length. In our calculations we assume that all interfaces are equally spaced and their distance, L_p, is much smaller than the wavelength. We choose $L_p \approx \lambda_0/100$ to ensure that the scattered light wave

responds to the disorder in the entire medium. The value of L_p is arbitrary and used to determine Δn for a specific localization length. The calculations are performed in the weak scattering limit with localization lengths that are more than 1,000 times larger than L_p. Figure 4.2a plots the calculated ensemble-averaged transmission for a fixed sample length depending on the estimated localization length[2]. The obtained intensity transmission follows exactly the function of Eq. (4.5). Alternatively, the localization length can be determined by $\langle \ln T(L) \rangle = -L/\xi$ which converges faster [72, 73] because $\langle T(L) \rangle$ can be dominated by anomalous transmission events such as necklace states [82].

An alternative possibility to relate the localization length to the disorder in a system is the average reflection, $\langle R \rangle$, between unit cells consisting of a fixed number of layers. This property is independent of the sample length and describes how much light is in average reflected from the individual unit cells. The average reflectance shows a powerlaw dependence on ξ and the results are presented in Fig. 4.2b. This functional dependence can be used to create a disordered medium of unknown length exhibiting a certain localization length that is determined by $\langle R \rangle$ and Δn, respectively.

4.2.2 Embedded light sources - Green's function formalism

In the previous section we presented an approach to estimate the transmission, the reflection, and the localization length of a disordered medium. In this section we apply the transfer matrix theory to calculate the Green's function of a one-dimensional disordered medium. The electric field distribution and the local density of states are determined by embedding light sources inside a disordered medium. In a one-dimensional system the Green's tensor simplifies to the Green's function, $G(z, z_0)$. As a disordered medium we consider stacked layers of different refractive indices with an embedded monochromatic point source, as shown in Fig. 4.3. To model the interaction between light and matter in a disordered medium we start from the inhomogeneous Helmholtz equation

[2] The calculations are based on $L = 100\,\mu$m, $\lambda_0 = 980\,$nm, and $\langle n \rangle = 3.5$ (gallium arsenide) allowing us a comparison to the experiments presented in Chapter 5 and 6.

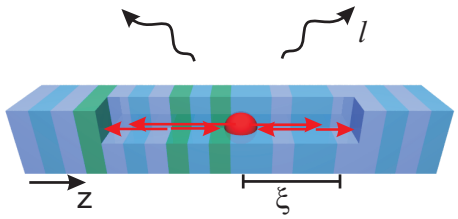

Figure 4.3: Illustration of a one-dimensional disordered structure with an embedded point source (red sphere). The structure is sliced to illustrate the scattered wave vectors of the light (red arrows). The colors of the layers represent different refractive indices (as in Fig. 4.1). We include losses out of the structure (black arrows) to approximate the experiment and define a loss length, l. The typical length scale on which light localizes is defined by the localization length, ξ.

for the electric field in the frequency domain [79, 83],

$$-\nabla^2 E(z,\omega) - k_0^2 \varepsilon(z) E(z,\omega) = \frac{k_0^2}{\varepsilon_0} P(z,\omega), \tag{4.6}$$

where $\varepsilon(z)$ denotes the position dependent relative permittivity and ε_0 is the electric constant. $P(z)$ acts as a source term and defines the polarization. For the electric fields we get

$$E(z,\omega) = \int_{-\infty}^{\infty} G(z,z',\omega)\, \frac{k_0^2}{\varepsilon_0}\, P(z',\omega)\, dz', \tag{4.7}$$

with $G(z,z',\omega)$ being the electric field Green's function of the material system. $G(z,z',\omega)$ is the solution to the equation

$$-\nabla^2 G(z,z',\omega) - k_0^2 \varepsilon(z) G(z,z',\omega) = \delta(z-z'). \tag{4.8}$$

Explicit expressions of $G(z,z',\omega)$ can often be found after expanding the Green's function in the basis of given eigenfunctions of the system. Eq. (4.7) can be integrated if we consider a point source at z_0 with a dipole moment $d(\omega)$ and substitute $P(z) = d(\omega)\delta(z-z_0)$

$$E(z,\omega) = G(z,z_0,\omega)\, \frac{k_0^2}{\varepsilon_0}\, d(\omega). \tag{4.9}$$

Hence, the Green's function determines the electric field at position z, having a point source at z_0. In a homogeneous one-dimensional medium ($\varepsilon = n^2 =$

const), the Green's function can be calculated analytically and describes a plane wave [78],

$$G(z, z_0, \omega) = \frac{i}{2\,k_0\,n} e^{i\,\beta\,|z-z_0|}. \tag{4.10}$$

The imaginary part of the Green's function determines the one-dimensional projected local density of states, ρ, in the medium (Appendix D.1)

$$\rho(z_0, \omega) = \frac{k_0}{\pi c} \Im(G(z_0, z_0, \omega)), \tag{4.11}$$

resulting in $\rho(\omega) = (2\pi\,c\,n)^{-1}$ for a homogenous medium.

While in a homogenous medium the Green's function is simply a plane wave that has its origin at the position of the point source, scattering events lead to modifications. A point source is positioned at z_0 in a host layer that is surrounded by many disordered layers. This problem can be solved analytically [83, 84]. The derivation is self consistent and discussed in Appendix D.2. When the thickness of the host layer, L_p, is much smaller than the wavelength the solution simplifies and we get for the Green's function at the source position [85]

$$G(z_0, z_0, \omega) = \frac{i\,c}{2\,\omega\,n(z_0)} \times \frac{1 + r_L + r_R + r_L\,r_R}{1 - r_L\,r_R}. \tag{4.12}$$

To calculate the Green's function at all positions of the disordered medium we divide the medium in three parts: all layers to the left of the host layer, the host layer, and all layers to the right. The frequency dependent electric field reflection coefficients correspond to the disordered medium to the left, r_L, and to the right, r_R, of the host layer and can be evaluated using transfer matrix theory. To calculate the Green's function at all positions of the medium, it is decomposed in a forward propagating amplitude, A, and backward propagating amplitude, B. The amplitudes are defined as A_R (A_L) and $B_R = r_R\,A_R$ ($B_L = r_L\,A_L$) for the stacked layers to the right (left) of the host layer with $G(z_0, z_0, \omega) = A_R + B_R = A_L + B_L$ and

$$A_R = \frac{i\,c}{2\,\omega\,n(z_0)} \times \frac{1 + r_L}{1 - r_R\,r_L}, \quad A_L = \frac{i\,c}{2\,\omega\,n(z_0)} \times \frac{1 + r_R}{1 - r_L\,r_R}. \tag{4.13}$$

First, we focus on the right hand side ($z > z_0$). The Green's function is calculated by identifying A_R and B_R with A_0 and B_0 (Fig. 4.1) and utilizing the transfer matrix theory (Eq. (4.2)). The position dependent Green's function

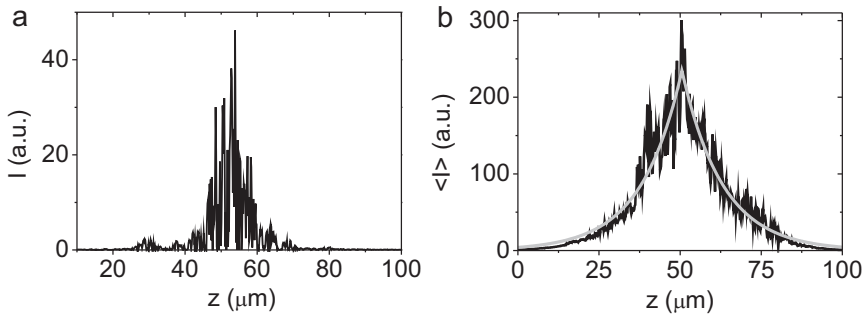

Figure 4.4: **a**, *Calculated intensity profile in a one-dimensional lossless medium with* $\xi = 15\,\mu m$. *The thickness of the layers is* $L_P = 10\,nm$, *the length of the structure is* $100\,\mu m$, *the refractive index varies within* $n = 3.5 \pm 0.32$, *and the monochromatic light source with* $\lambda = 980\,nm$ *is placed at* $z_0 = 50\,\mu m$. **b**, *Ensemble-averaged spatial intensity profile. The gray curve is a fit to the data with* $I(z) = \exp(-|z - z_0|/2\xi)$.

equals $G(z, z_0, \omega) = A(z) + B(z)$. The outlined approach can also be applied to the left hand side of the host layer ($z < z_0$) using A_L and B_L instead[3]

Fig. 4.4a displays the intensity profile, $I(z)$, in a disordered medium with a light source positioned in the center. The intensity shows strong fluctuations that originate from multiple scattering of the emitted light. The spatial intensity profile, obtained after ensemble averaging over 10,000 different realizations of disorder, is presented in Fig. 4.3b. From a fit to the ensemble-averaged intensity we obtain a localization length of $\xi = 15\,\mu$m. This value equals the localization length that has been used to generate the individual disordered structures. In accordance with the prediction, Eq. (4.5), these results demonstrate clearly the validity of our model.

So far, we calculated the Green's function assuming the excitation of a single point source. A local spatial average over the Green's function around the source position corresponds to the excitation of an ensemble of emitters reflecting the experimental situation discussed in Chapter 6. To model the local excitation of many emitters, we can utilize that the reflection coefficients

[3]For $z < z_0$ the order of the layers has to be reversed before applying Eq. 4.2.

oscillate on the scale of the wavelength. If the excitation position is shifted by Δz then $r_L \rightarrow r_L \exp(i\,\beta\,2\Delta z)$ and $r_R \rightarrow r_R \exp(-i\,\beta\,2\Delta z)$. The product $r_L\,r_R$ does not display the oscillations and this combination should be contained. When we perform a spatial average over one wavelength (average over the rapid oscillations), we can express the Greens function in terms of [85]

$$\langle G(z_0, z_0, \omega)\rangle = \frac{i\,c}{2\,\omega\,n(z_0)} \times \frac{1 + r_L\,r_R}{1 - r_L\,r_R}, \tag{4.14}$$

that is related to the so-called spatially averaged local density of states, $\langle\rho(z_0,\omega)\rangle = \frac{k_0}{\pi c}\langle\Im(G(z_0,z_0,\omega))\langle$.

4.3 Fluctuations in the transmittance and the emitted intensity

Characterizing a multiple scattering medium by its statistical means requires an ensemble average of physical quantities. The evaluation of the probability distribution of the transmitted light, $P(T/\langle T\rangle)$, for different realizations of disorder is a well-established method to determine Anderson localization since $P(T/\langle T\rangle)$ depends sensitively on ξ. Figure 4.5a plots $P(T/\langle T\rangle)$ deep in the localized regime showing log-normal distributions. The crossover from localization to the ballistic regime occurs for $\xi = L$ where a very flat transmission distribution is found (Fig. 4.5b). For even weaker scattering ($\xi \gg L$) $P(T/\langle T\rangle)$ is normal distributed. Here, we want to emphasize that our results display very similar transmission distributions as three-dimensional calculations [86] in photonic crystal waveguides, indicating that a photonic crystal waveguide behaves as a one-dimensional disordered medium (see Chapter 5 and Chapter 6). Note that a one-dimensional structure only supports one forward and one backward propagating mode and the total transmission through the structure equals the transmission in a single channel. Therefore, these results are different from calculations through a disordered waveguide that supports many spatial modes. In the present case, the single channel transmission does not show the Rayleigh distribution, as predicted for the transmission of a single speckle [45], neither it recovers the characteristic deviation from the Rayleigh distribution on the onset of localization [51].

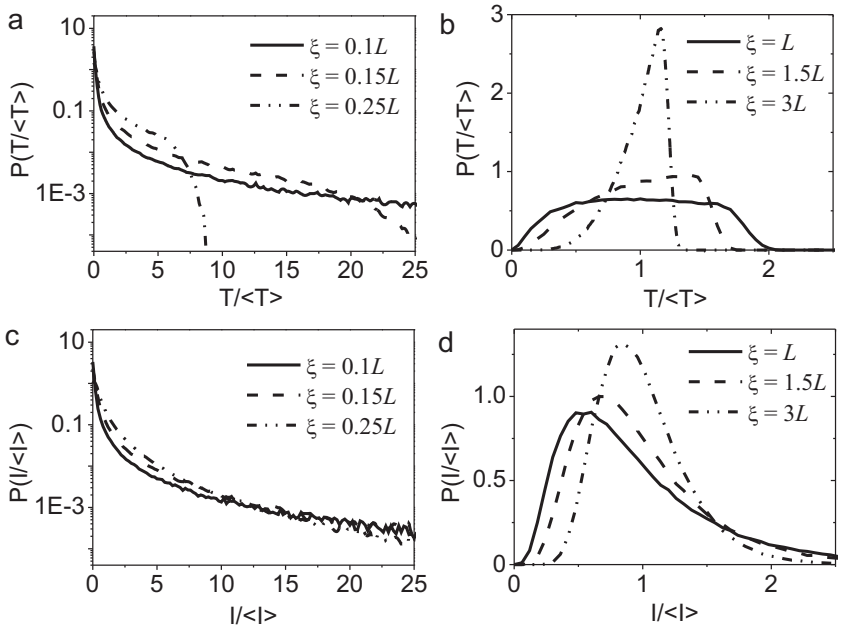

Figure 4.5: Transmission probability distributions in one-dimensional multiple scattering media for different localization lengths **a**, *in the localized regime* ($\xi < L$) *and* **b**, *for ballistic light transport* ($\xi \geq L$). *The transmissions are normalized to the average transmittance.* **c**, **d**, *Intensity probability distributions of an emitter embedded at the center of a disordered medium and normalized to the average intensity. The graphs are calculated for the same localization lengths as used for the transmission distributions. All presented data are obtained after ensemble averaging over 250,000 different realizations of disorder.*

The total emitted intensity of an embedded emitter in a one-dimensional system is proportional to the local density of states and can be calculated from the Green's function[4]. Figure 4.5c displays the emitted intensity probability distributions for the same localization lengths, as used in Fig. 4.5a. A very different behaviour is observed by comparing the probability distributions of the emitted intensity with the transmission distributions. In contrast to the

[4]The intensity depends on the radiative decay rate of the emitter. Therefore, the emitter needs to be excited continuously.

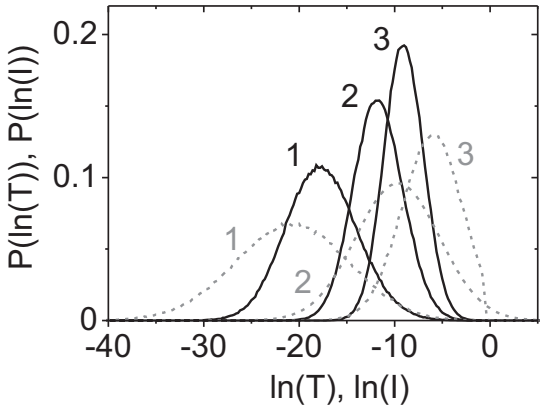

Figure 4.6: Direct comparison of transmission (dashed gray) and emitted intensity (black) probability distributions deep in the localized regime for 1: $\xi = 0.05L$, 2: $\xi = 0.1L$ and 3: $\xi = 0.15L$. All distributions are found to be log-normal distributed.

transmission, the intensity remains log-normal distributed when approaching $\xi = L$ (discussed below). For $\xi > L$ the emitted intensity approaches a normal distribution in the weak scattering limit, as illustrated in Fig. 4.5d. We find that the emitted intensity distribution is independent of the emitter position inside the medium. A detailed study of the differences between the transmission and the emitted intensity deep in the localized regime is presented in Fig. 4.6. Both quantities are log-normal distributed but do not follow each other for the same localization length. To validate our model with analytical predictions we compare the transmission distributions with [87]

$$P(\ln T) = A\sqrt{\frac{\xi}{4\,\pi\,L}}\,\exp\left(-\frac{\xi}{4\,L}\times\left(\ln T + \frac{L}{\xi}\right)^2\right) \tag{4.15}$$

and find an excellent agreement. Note that this expression only holds deep in the localized regime for negligible ballistic light transport. As for the transmission, the intensity distributions are predicted to show log-normal tails $P(\ln I) \propto \exp\left(-\text{const}\,(\ln I)^2\right)$ [85] that we recover with our calculations, too. Deep in the localized regime, the distribution of the total transmittance is broader than of the intensity. This behavior is due to the fact that the

Anderson-localized modes are confined inside the sample. The modes are not influenced by the boundary conditions and the transmission is almost zero for the majority of disorder realizations. Rarely, a very high sample transmission ($T \to 1$) can be measured that originates from so-called necklace states [82] and give rise to the transmission broad distribution (dashed lines in Fig. 4.6).

4.3.1 Impact of losses

In the localized regime, the ensemble-averaged intensity decays exponentially. Light losses, such as light leakage or absorption, lead to an exponential decay of the intensity profile, too [26, 27]. In our calculations losses are incorporated by including an imaginary part in the refractive index with an associated loss length $l = 1/k_0\Im(n)$. The measured effective localization length in transmission measurements is called extinction length, ℓ_e, and defined as

$$\frac{1}{\ell_e} = \frac{1}{\xi} + \frac{1}{l}. \tag{4.16}$$

In presence of a finite loss length, ℓ_e appears shorter than ξ. Therefore, con-

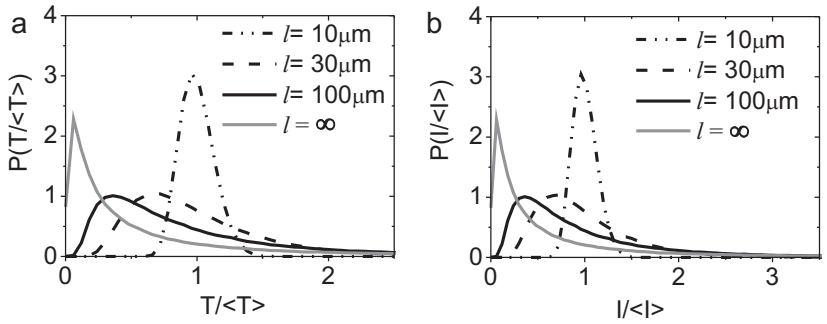

Figure 4.7: **a**, *Transmission and* **b**, *emitted intensity probability distributions for $\xi = 25\,\mu m$ for different amount of losses induced in the disordered medium ($L = 100\,\mu m$). A lossless medium is represented by $l = \infty$.*

firming Anderson localization utilizing transmission measurements might be misleading. Here, the distribution in the transmittance can serve as a rough estimate of losses. Figure 4.7a shows that in absence of losses the most likely

transmission is much lower than the average transmission. As losses increases the log-normal distribution converges to a normal distribution and the most likely transmission approaches the average transmission. In contrast to the calculations where ξ is varied (Fig. 4.5b), the distribution changes directly from log-normal to normal. The emitted intensity probability distribution approaches a normal distribution with increasing losses, too (cf. Fig. 4.7b). However, we cannot distinguish between changing the loss length and changing the localization length. Lossless media with a certain localization length exhibit a specific transmission and intensity distribution. These distributions are found to be very similar to distributions that are obtained from disordered lossy media that have an accordingly smaller localization length. This can be explained by the fact, that losses shorten effectively the sample length to L_{eff}. The distributions only depend on the ratio ξ/L which is in presence of losses given by ξ/L_{eff}. To obtain the same ratio (same distributions), ξ needs to be reduced.

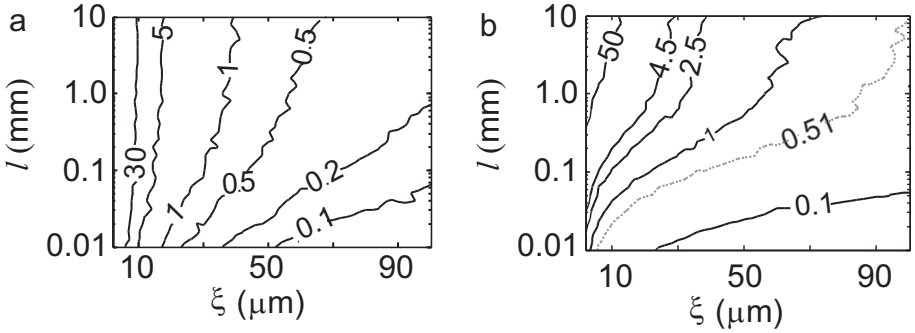

Figure 4.8: **a**, *Contour plot of the variances of the transmission fluctuations,* $\text{var}(T/\langle T\rangle)$, *and* **b**, *emitted intensity fluctuations,* $\text{var}(I/\langle I\rangle)$. *The calculations are presented as a function of loss length and localization length. The sample length is* $L = 100\,\mu m$. *The gray dashed contour line in b represents the variance in the emitted intensity fluctuations that can be measured for* $\xi = L$ *in absence of losses. By inducing losses in the medium the variance decreases (when* ξ *is fixed). Thus,* $\text{var}(I/\langle I\rangle) = 0.51$ *serves as a criterion for Anderson localization.*

Each transmission (intensity) distribution corresponds to a certain variance in the transmission (intensity) fluctuations. The calculations of the variance are plotted in Fig. 4.8. The Figure shows that the variance decreases with increas-

ing losses and increasing localization length. A. A. Chabanov *et al.* applied this behavior to establish a criterion for Anderson localization that holds even in presence of absorption [3]. Our calculations confirm their results, predicting that if the variance of the transmission distribution exceeds $\mathrm{var}(T/\langle T\rangle) > 0.2$ the sample localizes[5] ($\xi < L$). Similarly, we define a criterion for Anderson localization that concerns the fluctuations in the light emission from an emitter embedded in a disordered medium. As for the transmission the intensity fluctuations decrease with increasing localization length and decreasing loss length, presented in Fig. 4.8b. We find that the fluctuations in $I/\langle I\rangle$ are much larger than in $T/\langle T\rangle$. If the variance in the intensity fluctuations exceeds the value $\mathrm{var}(I/\langle I\rangle) \geq 0.51$ then ξ is smaller than L and Anderson localization occurs in one-dimensional disordered samples (dashed line in Fig. 4.8b). This result is general and independent on the losses and the sample length.

4.4 Quality factor distributions of Anderson-localized modes

The response of a disordered medium to the incident light wave is strongly frequency dependent. This provides an alternative to obtain a new realization of disorder by fixing the refractive indices of the layers and changing the frequency of the light source instead. The frequency dependent transmission through a disordered medium is shown in Fig. 4.9a. Clear distinct optical modes with high transmission can be observed belonging to different realizations of disorder. Thouless showed that the average spectral linewidth width of the modes $\delta\lambda$ and average distance between those modes $\Delta\lambda$ serve as a criterion of Anderson localization of light, namely $\delta\lambda/\Delta\lambda < 1$ [88]. Thus, the modes are not only spatially localized but also spectrally distinct. This does not apply in the ballistic and diffusive regime where modes overlap spectrally. Embedding an emitter enables us to calculate the frequency dependence of the local density of states (Eq. (4.12)). Figure 4.9b plots the corresponding total emitted intensity for a light source positioned in the center of the disordered medium. Comparing Fig. 4.9 a and b, we find modes with enhanced intensity at similar positions reflecting that we investigate the same structure. The lo-

[5] Their definition of ξ differs from our definition [72] by a factor of two. Hence, we have to compare our result at $\xi = L/2$ with their result and get the same variance $\mathrm{var}(T/\langle T\rangle) = 2/3$.

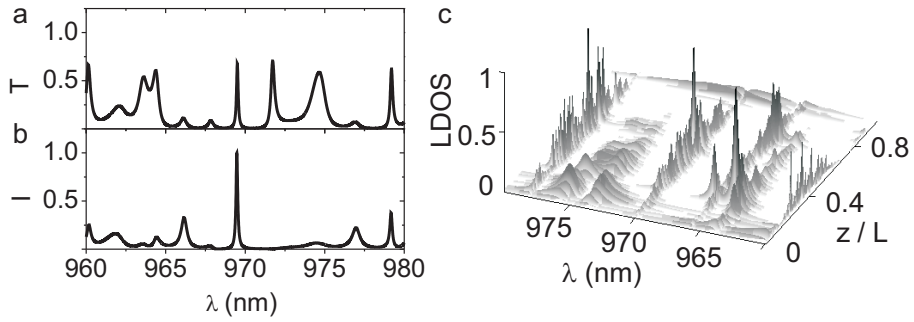

Figure 4.9: **a**, *Calculated transmission spectrum through a disordered medium depending on the wavelength of the light source positioned outside of the medium. The localization length is* $\xi = 0.4L$. **b**, *Normalized emission spectrum of an emitter embedded in a disordered medium that corresponds to the emitter decay rate. The monochromatic light source is placed at the center of a multiple scattering medium (same disorder realization as in* **a**). **c**, *Spatially and spectrally resolved local density of states (LDOS) of a disordered medium using the same parameters in the calculations as in panel a and b. The LDOS is normalized to its maximum.*

cal density of states for a one-dimensional medium in the localized regime is depicted in Fig. 4.9c. In accordance with the expectation, large fluctuations are observed. The Anderson-localized modes are spectrally well-separated and spatially confined due to the disorder in the sample.

The spectral extension of an Anderson-localized mode can be characterized by the quality factor (Q factor), as used for traditional cavities [20]. It is defined as the ratio of the central wavelength and its mode linewidth. In an extensive analysis Q factors of Anderson-localized modes are calculated in a small spectral region for many different realizations of disorder. The obtained Q factor distributions of Anderson-localized modes are plotted in Fig. 4.10a and found to be in agreement to the predicted log normal distributions [89, 90]. The long tails of the distributions describe a non-vanishing probability to observe very high Q factors. This probability increases when the ratio ξ/L decreases, as shown in Fig. 4.10b. Moreover, each Q factor distribution can uniquely be assigned to a localization length which is essential to compare experimental

data and theory. We highlight that all presented calculations are general and only depend on ξ/L.

4.4.1 Impact of losses

One important result of Section 4.3.1 is that losses in a disordered medium reduce the fluctuations in the transmission and emitted intensity distributions. The Q factor determines the dwell time, τ, that a photon stays inside the optical mode without exiting the sample or being absorbed, i.e., $Q = \tau\,\omega$. Figure 4.11a displays the Q factor distributions depending on the loss length, l, obtained after evaluating the linewidths of 100,000 Anderson-localized modes that belong to different realizations of disorder. In absence of losses the Q factors of Anderson-localized modes are log-normal distributed. With increasing losses the distributions are found to be truncated. This shows that not only a finite system size but also losses limit the maximum dwell time before the photon leaks out of the structure or gets absorbed. The Q factor in a medium that exhibits losses can be expressed as

$$Q^{-1} = Q_0^{-1} + Q_l^{-1}, \tag{4.17}$$

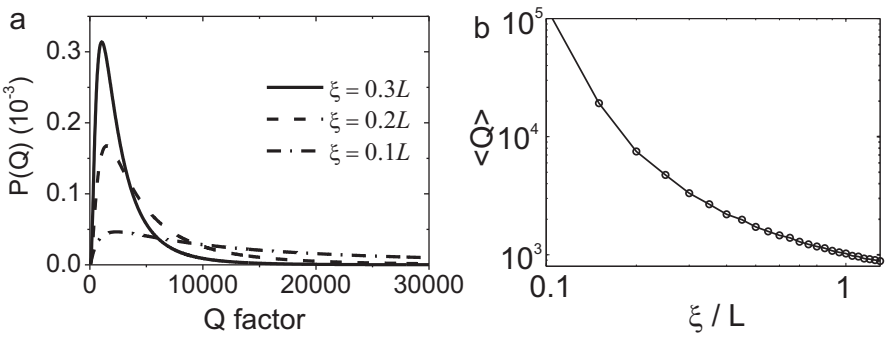

Figure 4.10: **a**, *Q factor probability distributions in lossless one-dimensional media. The distributions are shown for different localization lengths relative to the sample length.* **b**, *Ensembles averaged Q factor, $\langle Q \rangle$, as a function of localization length. An increase in the average Q factor reflects a higher probability to observe large Q factors.*

where Q_0 corresponds to the mode quality factor in absence of losses. Q_l represents the degradation of the quality of light confinement due to the losses in the medium and thus is related to the loss length. Starting from the generalized eigenproblem of the wave equation of a source-free medium (Eq. (4.6), where $P(z,\omega)=0$) we can account for losses using perturbation theory. In particular we are interested in the frequency perturbations $\Delta\omega$ that result from small perturbations $\Delta\varepsilon$ in the relative permittivity

$$\Delta\omega = -\frac{\omega}{2}\,\frac{\langle E(z)|\Delta\varepsilon|E(z)\rangle}{\langle E(z)|\varepsilon|E(z)\rangle} + O(\Delta\varepsilon^2), \tag{4.18}$$

where $E(z)$ describes the electric field in the lossless unperturbed medium. If we now separate the relative permittivity in a real and an imaginary part, $\varepsilon = \varepsilon' + i\varepsilon"$ we get for $\varepsilon" \ll \varepsilon'$

$$\begin{aligned}\Delta\omega &= -\frac{\omega}{2}\,\frac{\langle E(z)|\varepsilon"|E(z)\rangle}{\langle E(z)|\varepsilon'|E(z)\rangle} \\ &= -\frac{\omega\,\varepsilon"}{2\varepsilon'}\,\frac{\langle E(z)|\varepsilon'|E(z)\rangle_{\mathrm{m}}}{\langle E(z)|\varepsilon'|E(z)\rangle_{\mathrm{t}}}.\end{aligned} \tag{4.19}$$

The subscripts denote the perturbation in the material (m) and in the total sample (t). Hence, the last term refers to the fraction of the sample that is being perturbed which is approximately one in our case. The perturbations in the relative permittivity lead to changes in the frequency resulting in frequency perturbations $\Delta\omega$. Furthermore we can relate relative permittivity to the refractive index, $(n' + i\,n")^2 = \varepsilon' + i\,\varepsilon"$, and by substituting $Q = \omega/(2\Delta\omega)$ we get $Q = n'/(2n")$. According to Lambert Beer's law the intensity loss length is related to the refractive index $l = 1/(k_0\,n")$ resulting in the final expression

$$Q_l = \frac{n'\,\pi}{\lambda}\,l, \tag{4.20}$$

with n' being the average real part of the refractive index. Utilizing Eq. (4.17) the distribution of the measured Q factors is given by $P(Q) = P(Q_0)\frac{dQ_0}{dQ}$, where $P(Q_0)$ is determined by the ratio ξ/L [89]. The resultant Q factor distributions in the presence of losses is then defined as

$$P(Q) = -\exp\left(-\frac{(\mu - \log(-Q\,Q_l/(Q-Q_l)))^2}{2\sigma^2}\right) \times \frac{Q_l\,H(-Q+Q_l)}{\sqrt{2\pi}\,\sigma(Q-Q_l)}. \tag{4.21}$$

The localization length determines the parameter of the lognormal distribution, σ and μ, H is the heaviside step function. A fit to the data (Fig. 4.11a) reveals

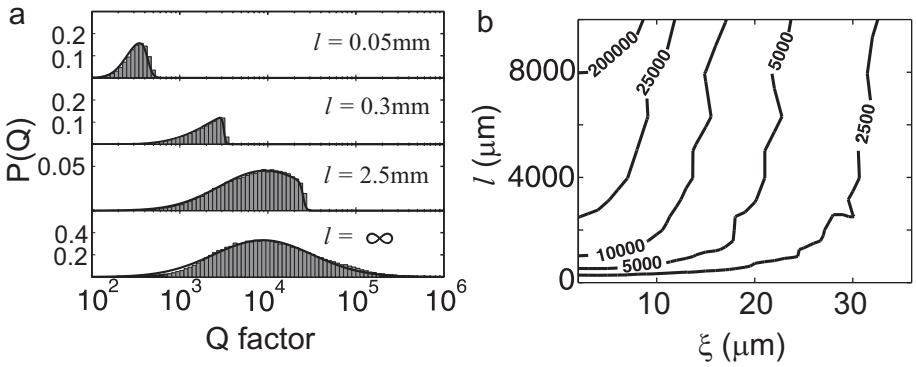

Figure 4.11: **a**, *Truncated log-normal Q factor distributions depending on the loss length in a disordered medium ($\xi = 13\,\mu m$).* **b**, *Plot of the average Q factor (represented by the contour lines) depending on loss length and localization length. The simulated structures in* **a**, **b**, *have a sample length of $L = 100\,\mu m$ and the emitter wavelength in the calculations varies within $\lambda = 970 \ldots 990\,nm$.*

a linear dependence of the maximum Q factor and the loss length. Remarkably, losses can truncate high Q factors, even though the loss length is of the order of 10 mm while the sample length is only $L = 100\,\mu$m (Fig. 4.11b). In order to test our findings of Eq. (4.21) we estimated l from the fitted Q_l and ind a perfect agreement to the initial parameters for the loss lengths used in the calculations showing the consistency of our model. Further investigations show that the fitted for loss lengths, $l > L$, the characteristic parameter of the underlying log-normal distribution does not change but is only truncated. This allows us to distinguish between Anderson localization and losses in a one-dimensional structure. Each localization length is related to an unique log normal Q factor distribution while each loss length cuts the distribution at a characteristic value.

A drawback of a highly engineered cavity is the reduction of its Q factors due to fabrication imperfections. On the contrary, a Q factor distribution formed by Anderson localization is inherently robust against disorder. For studies of enhanced light-matter interaction [91], it is essential that a system exhibits tightly confined optical modes with a high Q factor and a small mode-volume. Anderson-localized modes are very promising since their Q factor distributions provide non-vanishing probability to observe a large Q (Fig. 4.10a). Further-

more, the average mode volume that a photon explores in a disordered structure decreases as ξ decreases. Thus, the light-matter interaction in disordered photonic structures can be enhanced by decreasing ξ, and minimizing losses in the structures, reaching eventually strong coupling between light and matter [92].

4.5 Conclusion

In conclusion, analytical calculations were presented to determine the transmission and the local density of states in a one-dimensional disordered medium. The statistical properties of Anderson localization were investigated by means of the transmission distributions and transmission fluctuations placing a light source outside of the structure. The emitted intensity distribution of a light source embedded inside a disordered structure was calculated and the fluctuations of the intensity were used to establish a new criterion for Anderson localization. By changing the frequency of the light source, the Q factor distributions of Anderson-localized modes were calculated. In presence of losses, these distributions were found to be truncated which can possibly be used to distinguish between Anderson-localization and losses.

Chapter 5

Controlling Anderson localization in photonic crystal waveguides

5.1 Introduction

Indications of three-dimensional Anderson localization of light have been observed in entirely disordered samples like powders [17, 16] or dielectric layers [93, 82]. In these systems no control can be exerted over the frequency or spatial extent of the localized modes. A promising proposal on how to control multiple scattering is to induce a slight amount of disorder in periodic nano-structures called photonic crystals [25]. In an ideal photonic crystal the light propagation is described by Bloch modes [94]. Breaking the symmetry of such structures leads to multiple scattering of light. The interference of multiply scattered light can form Anderson-localized modes appearing at random positions in the system but in a restricted frequency range close to the photonic crystal bandgap. Contrary to non-dispersive systems, photonic crystals offer the possibility to modify the photonic density of states with respect to a homogeneous medium that controls Anderson localization through a highly dispersive localization length.

The first experimental signature of light confinement in disordered photonic crystal waveguides was presented by J. Topolancik *et al.* [95]. Close to the waveguide mode band edge, they observed spatially and spectrally confined modes. However, they did not investigate ensemble-averaged quantities such as the localization length to prove Anderson localization. Despite this ground-breaking experiment, the experimentally observed deviations from the light dispersion in photonic crystal waveguides were not attributed to disorder induced Anderson localization of light [96, 97, 98, 99].

This chapter is devoted to studies of light propagation in disordered photonic crystal waveguides. Chapter 5.1.1 introduces the fundamental properties of photonic crystals and the impact of disorder. In Section 5.2, we show experimentally how to control and tune accurately the localization length, ξ, and the frequency range where Anderson-localized modes appear, exploiting the dispersion in a photonic crystal. Contrary to earlier experiments we do not focus on single measurements, but investigate the statistical properties of Anderson-localization utilizing different realizations of disorder. In particular, we present ensemble-averaged measurements of the extinction mean free path, ℓ_e, which describes the attenuation of the light transmission along the waveguide. We confirm that the strongly confined modes appearing for high density of states, where we approximate $\ell_e \approx \xi$, are due to one-dimensional Anderson localization. In addition, we interpret our experimental data of the wavelength-dependent localization length with a model that links the localization length explicitly to the density of states. Finally, we investigate the probability distribution of the transmitted light and confirm the dispersion in the localization length.

5.1.1 Disordered photonic crystal waveguides

A two-dimensional photonic crystal is a dielectric material that consists of a triangular periodic lattice of air holes etched in a high refractive index membrane. The periodic lattice forms a frequency bandgap where light propagation is suppressed. A one-dimensional waveguide for light can be created by omitting a row of air-holes in the periodic lattice. (Fig. 5.1a). To investigate the impact of disorder on the light propagation, the hole positions are varied randomly in

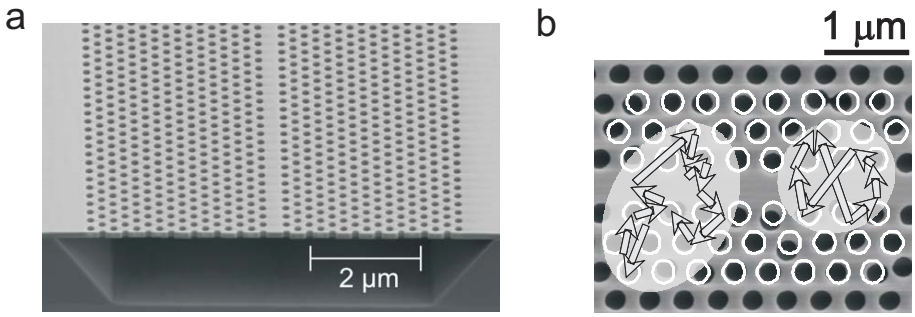

Figure 5.1: **a**, *Scanning electron microscope image of a photonic crystal waveguide.* **b**, *Photonic crystal waveguide with $\delta = 6\,\%$ engineered disorder (standard deviation relative to the lattice constant). The white circles represent the hole positions in an ideal structure without disorder. Imperfections can lead to multiple scattering and Anderson-localized modes form spontaneously. The shaded areas illustrate the localized light intensity and the arrows depict the wave vectors of Anderson-localized modes.*

the three rows above and below the waveguide using a Gaussian random number generator function (Box-Muller). The degree of disorder in each sample, δ, is characterized by the standard deviation of the hole positions relative to the lattice constant within $\delta = 0, 1, \ldots, 6, 9, 12\,\%$ (Fig. 5.1b). Details of the fabrication process is described in Appendix E.1.

A complete bandgap for light can be achieved in three-dimensional photonic crystals, whereas in two dimensions a bandgap only exists for transversal electromagnetic waves. The optical modes, that the structure sustains, can be calculated numerically [100]. The corresponding dispersion diagram of our samples is shown in Fig. 5.2a. As design parameters we used a lattice constant of $a = 240\,\text{nm}$, a filling fraction $f = 0.330 \pm 0.006$, the refractive index of gallium arsenide under ambient conditions of $n = 3.54$, and a membrane height of $160 \pm 5\,\text{nm}$. The gray shaded area displays the optical bandgap that can be controlled by varying the fabrication parameters. Introducing a one-dimensional waveguide breaks the crystal symmetry and creates optical modes inside the bandgap that are confined to the waveguide (gray graphs). Due to the underlying periodicity, the light propagation in an ideal photonic crystal waveguides

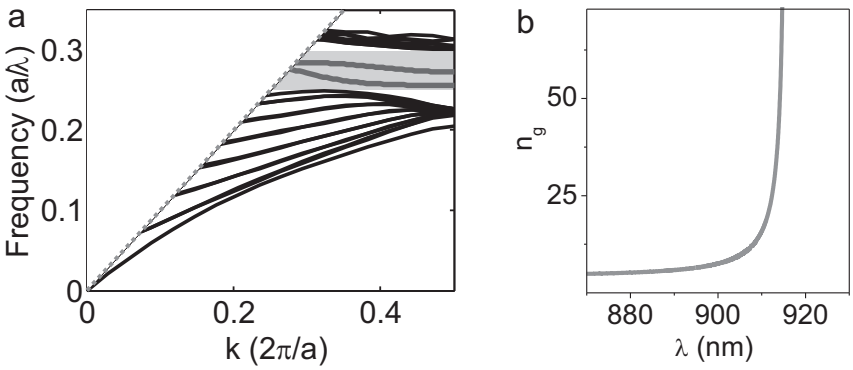

Figure 5.2: Calculated dispersion diagram of a photonic crystal waveguide. **a**, *Band structure of the supported transverse electromagnetic modes in the ideal photonic crystal without a waveguide (black graphs). For a limited frequency region the crystal does not provide optical modes (gray shaded area). All modes above the light line (dashed) are radiation modes out of the membrane plane and are not confined by the crystal. Introducing a waveguide in the structure gives rise to two defect modes (gray graphs) with orthogonal polarization inside the bandgap (gray shaded area). The wave vector of these two modes always points along the waveguide forming a one-dimensional system for light propagation.* **b**, *Dispersion relation of a guided defect mode as a function of wavelength. The group index, n_g, diverges, when the spectral mode band edge is reached.*

is described by extend Bloch-modes following a dispersion relation $\omega(k)$ [94]. The frequency of light is denoted as ω and k is the absolute value of the wave vector. The slope of the lower waveguide mode in Fig. 5.2a becomes infinitely small as k increases. This reflects an increase in the group index, $n_\mathrm{g} = \frac{\partial k}{\partial \omega}$, which can be illustrated in a waveguide mode dispersion relation (Fig. 5.2b). The divergence of the group index corresponds to the spectral mode band edge which is calculated to be 915 nm. The corresponding density of states, DOS, is proportional to the group index. The group velocity is inversely proportional to n_g and is slowed down as the group index increases [101]. Here, we introduce two regimes: $n_\mathrm{g} \leq 10$ is called the low-density of states regime while $n_\mathrm{g} > 10$ is referred to as the high-density of states regime.

In a photonic crystal waveguide scattering events change the direction of light propagation resulting in a forward and in a backward propagating Bloch-mode. The distance between two scattering events is defined as the scattering mean free path, l_s, and can be related to the localization length via $\xi \approx N \cdot \ell_\mathrm{s}$ [72, 102]. N is the number of spatial electromagnetic modes that equals one in our single-mode waveguides. In order to relate ξ to the density of states, we model the function $\xi(\mathrm{DOS})$. Two separate mechanisms determine ℓ_s: the excitation of the scatterer and the radiation from the scatterer. The coupling to the scatterer is described by the density of states of the excitation beam [103], i.e., the waveguide mode. The second process is described by the local density of states. The local density of states equals the density of states of the waveguide mode ignoring the contributions of coupling to leaky radiation modes and modifications deep in the localized regime [104, 105]. This applies to every scattering event giving rise to a modified scattering cross section σ in photonic crystal waveguides scaling as $\sigma \propto \mathrm{DOS}^2(\omega)$. The scattering mean free path in a random medium in the independent-scattering approximation can be expressed as $\ell_\mathrm{s} = 1/\rho_\mathrm{s}\sigma$ (cf. Eq. (2.1)), where ρ_s is the density of scatterers. For one-dimensional single-mode photonic crystal waveguides we therefore predict

$$\xi \propto \mathrm{DOS}^{-2}(\omega). \tag{5.1}$$

In the next section the extinction mean free path is determined in photonic crystal waveguides as a function of the optical wavelength and the developed model (Eq. (5.1)) is applied to the experimental data.

5.2 Measurement of the extinction mean free path

5.2.1 Experimental setup

To investigate Anderson localization in photonic crystal waveguides we measure the light intensity in the waveguide as a function of distance from a light source, as illustrated in Fig. 5.3. A continuous wave Ti:Sapphire laser, tuneable within $\lambda = 700\,\mathrm{nm} - 1000\,\mathrm{nm}$, is coupled into a single mode tapered fiber with

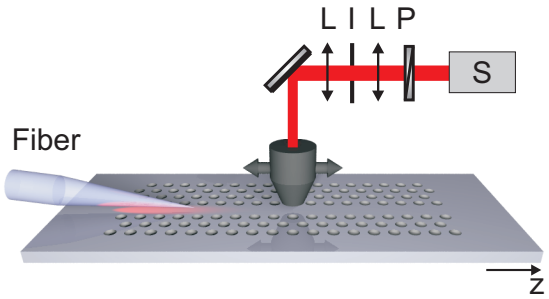

Figure 5.3: Illustration of the experimental setup to investigate Anderson localization of light in photonic crystal waveguides. Light is coupled into the waveguide with a tapered fiber. Light scattered from the waveguide is collected with a microscope objective (NA= 0.8), spectrally filtered (L: lens, I: iris), and recorded with a detector placed behind the spectrometer (S). The polarization of the detected light is selected with a polarizer (P).

a tip diameter comparable to the waveguide width. The evanescent mode of the fiber couples to the propagating mode of the waveguide by placing the fiber tip close to the waveguide. We measure the wavelength-dependent out-of-plane scattered light intensity from the top of the membrane, using a microscope objective, as a function of the distance z from the light source, i.e., the fiber tip. The distance is varied by scanning the objective along the waveguide. We probe different spatial realizations of disorder, that are, different parts of the sample by moving the fiber together with the objective along the waveguide. The measurement starts at $z = 150\,\mu\text{m}$ from the fiber tip to avoid any spurious effects due to the evanescent field from the fiber or light not coupled to the waveguide mode. Details of the experimental setup are discussed in Appendix E.2.

Fig. 5.4a shows a single disorder realization measurement of the scattered light intensity versus the distance from the fiber tip, z, in the high-density of states regime ($\lambda = 916\,\text{nm}$). We did not induce any additional disorder in the photonic crystal waveguide ($\delta = 0\,\%$) and the sample is only affected by intrinsic unavoidable disorder induced by the fabrication process. The strong fluctuations in the light intensity correspond to speckles that originate from multiple scattering. The spectrum of the scattered light intensity, shown in Fig. 5.4b, proves that the fluctuations are restricted to the vicinity of the mode

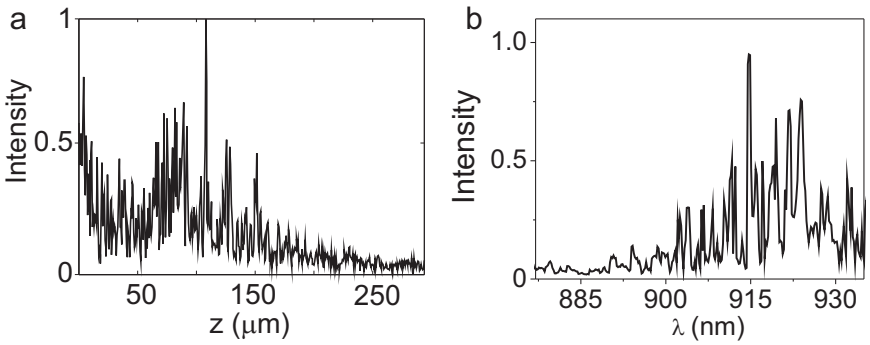

Figure 5.4: **a**, *Measured intensity fluctuations in the high-density of states regime depending on the distance form the light source for* $\lambda = 915\,nm$. **b**, *Spectrum of the light intensity, recorded at a fixed distance,* $z_0 = 150\,\mu m$, *from the fiber tip. Large fluctuations are observed close to the calculated mode band edge at* $\lambda = 915\,nm$.

cut-off where multiple scattering of light is pronounced. The strong random fluctuations in the light intensity are a signature of one-dimensional Anderson localization. Since our waveguides do not have an abrupt termination (the wafer is not cleaved), these resonances are not Fabry-Perot-like. The modes appear to be spatially and spectrally separated, which constitutes a criterion for Anderson localization [88].

5.2.2 Ensemble-averaged measurements

In the Anderson-localized regime the fluctuating light transmission, $T(L)$, decays exponentially after ensemble averaging versus sample length L with (Chapter 4.2) $\langle \ln T(L) \rangle = -L/\xi$. We assume that the scattered out-of-plane light intensity at a given position of the waveguide, I, is proportional to the total light transmission at the same position, i.e., that there is no significant spatial dependence of the out-of-plane scattering process. Any loss mechanisms of the light trapped in a photonic crystal waveguide influences the measured decay length. In the presence of losses, we have $\langle \ln(I(z)) \rangle = -z/\ell_e$, where the

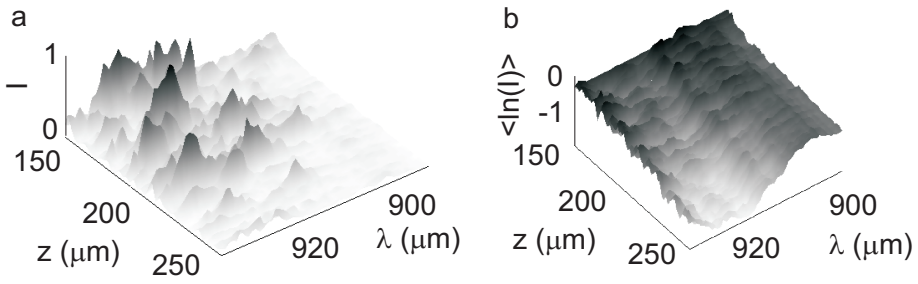

Figure 5.5: **a**, *Recorded intensity fluctuations from a single measurement along the photonic crystal waveguide depending on wavelength and distance from the light source. The intensity is normalized to its maximum value.* **b**, *Ensemble-averaged light intensity, obtained after repeating the experiment at eight different regions of the samples.*

extinction mean free path, ℓ_e, for a single-mode waveguide is defined as

$$\ell_\mathrm{e}{}^{-1} = \xi^{-1} + l_\mathrm{out}{}^{-1} + l_\mathrm{i}{}^{-1}. \tag{5.2}$$

l_i is the material inelastic absorption length and l_out is the loss length associated with out-of-plane losses. A further parameter can be important is the suppression of light propagation due to the bandgap of the photonic crystal and can be expressed by the imaginary part of the wave number $\Im(k_0^{-1})$. However, we argue that this term does not dominate for investigations of Anderson localization at the band edge of the waveguide mode where we have a non-vanishing density of state but should be considered for experiments deep inside the bandgap.

To prove Anderson localization ($\xi < L$), we measure the ensemble-averaged light leakage intensity from top of the waveguide versus z and wavelength (Figs. 5.5a and b). A single disorder realization measurement in our setup configuration consists of a scan of $I(z)$ for $150\,\mu\mathrm{m} < z < 280\,\mu\mathrm{m}$. The number of different disorder realizations that we can perform without adding repeated statistics to the ensemble average is limited by the sample length, $L = 1\,\mathrm{mm}$. For a detailed investigation of the localization length, we estimate the slope z/ℓ_e separately for all wavelengths within a restricted region of 1 nm. Figure 5.6 shows the linear fit of $\langle \ln I \rangle$, along the waveguide with $\delta = 0$ % for two

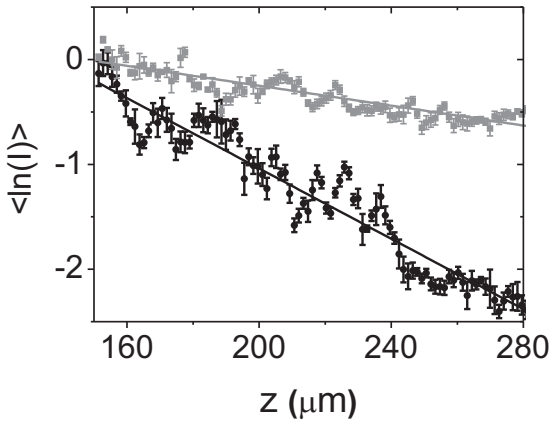

Figure 5.6: Fit of the ensemble-averaged light intensity in a photonic crystal waveguide with $\delta = 0$ % as a function of the distance from the source for two wavelengths: $\lambda_1 = 890$ nm (gray squares) and $\lambda_2 = 916$ nm (black circles). The spectral resolution is 1 nm and the slope of the fitted lines equals to the inverse of the extinction mean free path.

different wavelengths $\lambda_1 = 890\,\mathrm{nm}$ and $\lambda_1 = 916\,\mathrm{nm}$ (gray and black plot, respectively). The wavelength corresponds to the low- and high-density of states regime (DOS $\propto n_\mathrm{g}$, cf. Fig. 5.2b). For these spectral positions we extract the extinction mean free path $\ell_\mathrm{e}(\lambda_1) = (161 \pm 16)\,\mu\mathrm{m}$ and $\ell_\mathrm{e}(\lambda_2) = (30 \pm 2)\ \mu\mathrm{m}$.

The fluctuations in the experimental data originate from not fully ensemble-averaged speckles. To test the degree of convergence of the ensemble average to $\langle \ln I(z) \rangle = -z/\ell_e$, we measured the goodness of the fits by performing a χ^2 - analysis [106] depending on the number of disorder realizations. Figure 5.7 shows that the χ^2 - value decreases as the realizations increases, confirming an improved fit quality. The goodness of the fit does not seem to level off at the optimum value $\chi^2 = 1$ that would prove that the single-exponential model is correct. Deviations from perfect verticality of the side walls of the air holes can break the symmetry in the out-of-plane direction and couple TE- and TM-polarized waveguide modes [95]. This polarization mixing mechanism may lead to multi-exponential decay of the ensemble-averaged transmission which is not resolved in the present experiment.

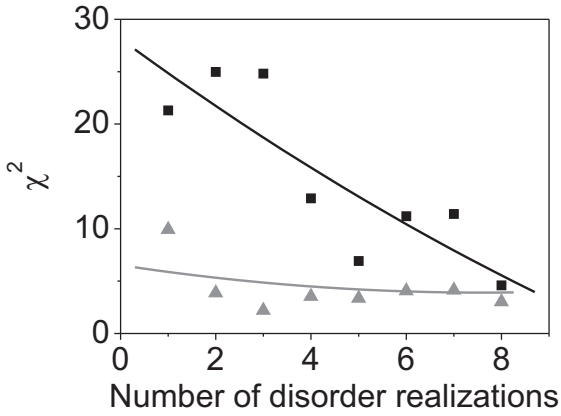

Figure 5.7: Plot of the fit-goodness, χ^2, that $\langle \ln(I(z)) \rangle = -z/\ell_e$ represents the ensemble-averaged light transmission versus number of disorder realizations for the same wavelengths, λ_1 and λ_2, used in Fig. 5.6 (same color code). The curves are guides-to-the-eye.

The dispersive behavior of the measured extinction mean free path after ensemble averaging is presented in Fig. 5.8 (black empty circles). We observe a 5-fold variation in ℓ_e with wavelength. For low-density of states, numerical simulations of Bloch-mode scattering in photonic crystal waveguides predict that out-of-plane losses dominate over backscattering losses [86]. Thus, we assume that in this spectral range l_{out} becomes comparable to ξ and affects the measured extinction mean free path significantly. This is confirmed by the fact that we cannot observe pronounced intensity fluctuations for $\lambda < 900\,\text{nm}$ (see Fig. 5.4b). For high-density of states ($\lambda > 900\,\text{nm}$) the backscattering process is expected to dominate and we attribute the variation in ℓ_e to a dispersive localization length. By assuming $\ell_\text{e} \cong \xi$ in the high-density of states regime, we observe that the localization length reaches its minimum value of $\sim 27 \pm 1\,\mu\text{m}$ and becomes much smaller than the sample length, giving rise to strongly confined modes. The dispersive behavior of the localization length gives directly control over the extension of the modes, that can be varied by tuning the wavelength. We can also carefully control the frequency range of the localized-modes just by varying the fabrication parameters (typically a and f), thus, tuning the waveguide mode.

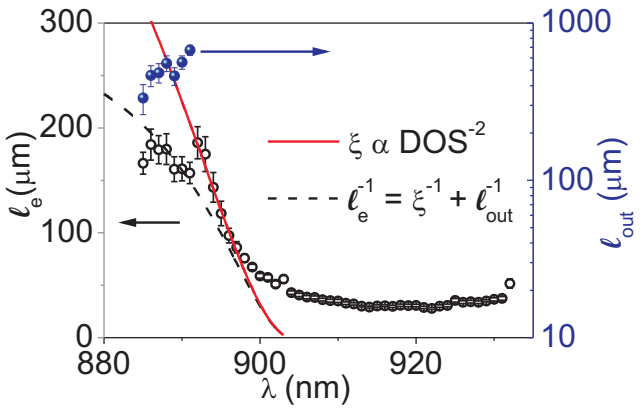

Figure 5.8: Plot of the extinction mean free path, ℓ_e, of the photonic crystal waveguide with $\delta = 0\%$ as a function of the wavelength (black empty circles). The extinction mean free path is found to be strongly dispersive and reaches a minimum for high-density of states ($\lambda > 900\,nm$). Losses mainly affect the extinction mean free path for very low-density of states ($\lambda < 890\,nm$). Here, the length, l_{out}, associated to out-of-plane losses (blue points) is comparable to the localization length. For higher-density of states, we can model the extinction mean free path with $\xi \propto DOS^{-2}$ (red curve). The dashed black curve is the fit to the data including wavelength-independent out-of-plane losses in the model and assuming the same waveguide mode band edge as for the solid curve.

Next, we compare our predictions $\xi(\mathrm{DOS}) \propto \mathrm{DOS}^{-2}$ (Eq. (5.1)) with the experimental results. The red curve in Fig. 5.8 represents the best fit to our data using the calculated density of states of the ideal photonic crystal structure (Fig. 5.2b). In the fit, we varied the waveguide mode band edge wavelength, λ_b, and the number of experimental data points that are included in the fit. In particular, the theory is predicted to deviate from Eq. (5.1) for high-density of states and for very low-density of states (discussed below). For each λ_b and number of considered data points, we can estimate the goodness of the fit. The corresponding χ^2 distribution depending on λ_b and the upper limit of density of the states for which the model can be applied is shown in Fig. 5.9. For this particular sample the mode band edge is found to be $\lambda_b = 902\,\mathrm{nm}$, being in agreement to the calculated mode band edge of $915 \pm 15\,\mathrm{nm}$. The theoretical

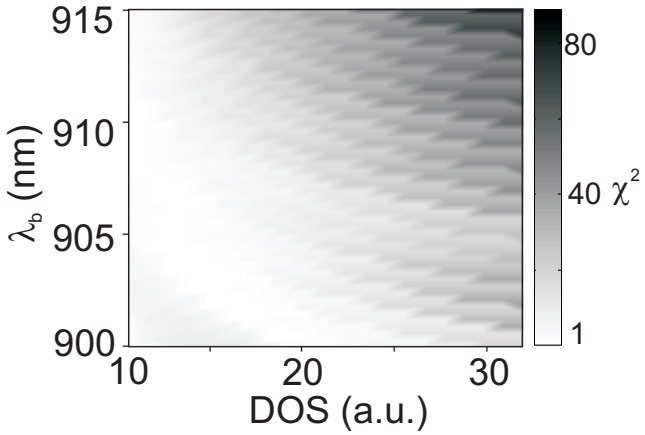

Figure 5.9: Fit of the spectral mode band edge wavelength, λ_b. Measured goodness, χ^2, that the function $\ell_e \propto DOS^{-2}$ represents the experimental data ($\delta = 0\,\%$). The goodness is shown depending on the upper limit of the density of states for which the model is assumed to break down. The fit quality improves as χ^2 decreases.

accuracy is limited by the uncertainties of the fabrication parameter. From the measured extinction mean free path (Fig. 5.8) we observe that the model breaks down deep in the Anderson localization regime ($\lambda > 900\,\mathrm{nm}$) where recurrent scattering occurs and the independent-scattering approximation is not valid anymore. The breakdown of our model may also be related to the fact that it is based on the calculated density of states of the ideal structure without disorder, which is modified in real structures [107].

The experimental data also depart from the model for very low-density of states, which we attribute to non-negligible out-of-plane losses. The sample material, gallium arsenide, has a very low optical absorption coefficient ($< 100\,\mathrm{cm}^{-1}$ at a wavelength of $\lambda = 915\,\mathrm{nm}$) corresponding to $l_\mathrm{i} > 1\,\mathrm{m}$. This value might be reduced by surface effects at the holes of the photonic crystal, but is still expected to be much larger than the sample length. Thus, absorbtion effects in the sample can be ignored. Therefore, we assume that the attenuation of the light transmission is due to out-of-plane scattering and light localization. Using Eq. (5.2), we extract l_out from the difference between the modeled ξ (red curve in Fig. 5.8) and the measured ℓ_e. Surprisingly, we observe an increase

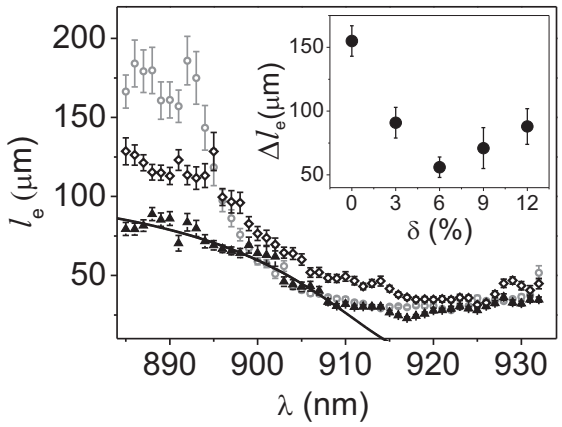

Figure 5.10: Extinction mean free path, ℓ_e, depending on the wavelength measured in photonic crystal waveguides with various amounts of disorder $\delta = 0\%$ (gray ∘), 6% (black ▲), and 12% (black ⋄). The solid curve is a fit to the data of $\delta = 6\,\%$ assuming a constant loss length of $l_{out} = 260\,\mu m$. The inset shows the difference between the maximum and minimum ℓ_e as a function of δ.

of l_{out} with increasing density of states (blue points in Fig. 5.8), which is in contrast to recent predictions [86]. Using the estimated parameter from the lossless model (red line) and including a constant out-of-plane extinction length as a free parameter, we fit the experimental data (black dashed line in Fig. 5.8). From the fit we obtain $l_{\text{out}} \sim 550 \pm 150\,\mu\text{m}$, which is indeed comparable to our estimation of the localization length in the very low-density of states regime. The model including a constant l_{out} is not found to be in good agreement to the data indicating a dispersive behavior in the out-of-plane loss length.

The effect of disorder on the extinction mean free path is plotted in Fig. 5.10 showing the measurement of ℓ_{e} in samples with increasing amount of disorder. The inset displays the difference between the maximum and minimum extinction mean free path ($\triangle\ell_{\text{e}}$) that occurs in the low- and high-density of states regime, respectively. $\triangle\ell_{\text{e}}$ decreases with disorder, reaches a minimum for $\delta = 6\%$ and increases for $\delta > 6\%$. We explain the decrease of $\triangle\ell_{\text{e}}$ for weak disorder by an increase of the out-of-plane light losses [86]. The increase for $\delta > 6\%$ is surprising and reflects the complex interplay between dispersive out-of-plane losses and the disorder induced in the photonic crystal waveguide. A

similar behavior has been found in numerical simulations of disordered three-dimensional photonic crystals in the absence of losses where the localization length reaches a minimum for an optimum amount of disorder [108]. This confirms the non-trivial relation between localization and disorder in photonic crystals.

5.2.3 Out-of-plane scattered intensity probability distributions

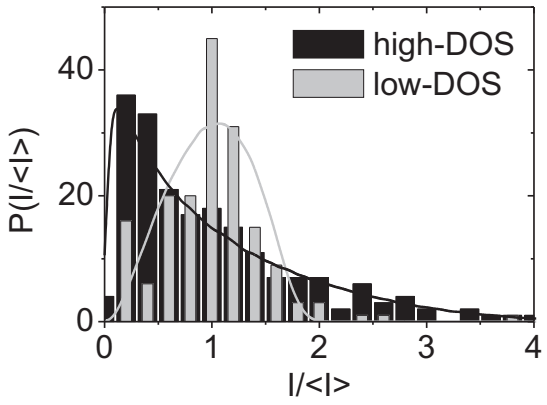

Figure 5.11: Distributions of out-of-plane scattered light intensity in the photonic crystal waveguide with $\delta = 6\%$ for low- and high-density of states (gray and black histograms). The black curve and gray curve show the calculated one-dimensional transmission probability distributions applying the transfer matrix theory using sample a length of $L_0 = 250\,\mu m$, a out-of-plane loss length of $l_{out} = 260\,\mu m$ and a localization length of $\xi = 90\,\mu m$ (high-density of states) and $\xi = 230\,\mu m$ (low-density of states), respectively.

A further approach to confirm Anderson localization is to investigate the transmission probability distributions (Chapter 4.3). Figure 5.11 compares the distributions of the out-of-plane scattered light intensity in a photonic crystal waveguide ($\delta = 6\%$) for low- and high-density of states (gray and black histogram), respectively. The normalized out-of-plane scattered light intensity,

$I/\langle I\rangle$, is measured at a fixed distance from the fiber tip ($z_0 = 250\,\mu\text{m}$) for 8 different disorder realizations. In order to increase the statistics, we collect $I/\langle I\rangle$ at different wavelengths, $\lambda = (885 \pm 10)\,\text{nm}$, and $\lambda = (915 \pm 10)\,\text{nm}$. For low-density of states, we measure a Gaussian-like intensity distribution centered around $I/\langle I\rangle = 1$. This behaviour is expected for the transmission probability distribution in one-dimensional samples when the out-of-plane extinction length is comparable to the localization length and to the sample length, i.e., the measurement distance z_0 (Chapter 4.3). On the contrary, for high-density of states, the distribution broadens and the deviation from a Gaussian is pronounced. This behavior can only be explained with a localization length that is much shorter than z_0 and l_{out}. The difference between the distributions for low- and high-density of states is a clear proof of a reduction in the localization length as the density of states increases. To confirm this, we model our experimental distributions using a transfer matrix theory formalism including losses (cf. Chapter 4). We obtain a good agreement by fitting our experimental distributions with one-dimensional transmission probability distributions. The constant loss length included in the calculations, $l_{\text{out}} = 260 \pm 100\,\mu\text{m}$, was determined by fitting the experimental data with ${\ell_e}^{-1} = A\xi^{-1} + {l_{\text{out}}}^{-1}$ (A represents a fitting constant). The rather large error in the loss length arises from the fact that the fit is sensitive to λ_b. The corresponding fitting curve is shown as a black line in Fig. 5.10. A good agreement between the theoretical transmission distributions and the experimental intensity distributions in Fig. 5.11 supports our approximation that the out-of-plane scattered intensity is proportional to the transmission through the photonic crystal waveguides. Furthermore it emphasizes that the light confinement in photonic crystal waveguides can be attributed to one-dimensional Anderson localization. We note that the intensity probability distributions do not provide a very precise way to distinguish between different values of the localization length and the out-of-plane extinction length since different sets of (ξ, l_{out}) can give rise to very similar distributions (see Figs. 4.5, 4.7). The experimental data are limited by finite statistics.

5.3 Conclusion

In conclusion, we have demonstrated the close relation between Anderson localization of light and the photonic density of states in photonic crystal waveguides, which was predicted but not yet demonstrated experimentally. The close relationship between the localization length and the density of states allowed us to control accurately the optical properties of Anderson-localized modes appearing in the high-density of states regime of photonic crystal waveguides. This is of fundamental importance since it imposes limitations for traditional slow-light devices based on photonic crystal waveguides such as single-photon sources [105]. At the contrary the strongly confined Anderson-localized cavities with tailored properties open a new route to explore cavity quantum electrodynamics or random lasing.

The presented experiments utilized disorder in the first three rows next to the waveguide while the remaining photonic crystal was unperturbed. It would certainly be interesting to investigate Anderson localization in photonic crystal waveguides depending on the number of rows that are disordered. Another promising experiment in the Anderson-localized regime could be a study of broader waveguides by omitting several rows in the periodic lattice. This might create a few spatial modes and additional intensity correlations could arise, for example very pronounced long range correlations. Furthermore, two-dimensional disordered photonic crystal membranes offer the possibility to investigate two-dimensional Anderson-localization of light.

Chapter 6

Probing Anderson localization with quantum emitters

6.1 Introduction

So far, Anderson localization has been experimentally probed by placing a light source outside of a disordered medium and analyzing its transmission properties. Most experiments investigated spatial, spectral, or temporal transmission properties of disordered media [17, 76, 82]. In Chapter 5, the localization length in disordered photonic crystal waveguides was determined from transmission experiments by measuring the extinction mean free path, ℓ_e. In the high-density of states regime, ℓ_e was attributed to the localization length. Confirming Anderson localization in transmission measurements is recurrently debated since the light losses strongly influence the measurement of the extinction mean free path. So far, no experiments have been presented where the localization length and the loss length have been quantified simultaneously using a direct measurement method.

In this chapter, a new approach is demonstrated by employing the light emission from quantum dots embedded inside disordered photonic crystal waveguides. Thereby, we access experimentally unexplored signatures of Anderson localization. The quantum dots excite very efficiently Anderson-localized modes in the high-density of states regime as opposed to transmission measurements where only a poor coupling to Anderson-localized modes is achieved. Internal emitters are therefore very promising to investigate statistical properties of Anderson localization. As proposed in Chapter 4, we compare the Q factor distributions of Anderson-localized modes our calculations and estimate the localization length, ξ, and the loss length, l. The obtained results confirm unambiguously Anderson localization in the investigated disordered photonic crystal waveguides. The spectral fluctuations in the quantum dot light intensity are compared to calculations of the light emission in one-dimensional media.

6.2 Light sources embedded inside disordered photonic crystal waveguides

6.2.1 Experimental setup

The statistical signatures of Anderson localization in disordered photonic crystal waveguides are probed in a confocal microscope setup, as illustrated in Fig. 6.1a. The design of the disordered photonic crystal waveguides is similar to those that have been used to study light propagation (Chapter 5). In addition, a layer of self-assembled indium arsenide quantum dots with a density of $\approx 80\,\mu\mathrm{m}^{-2}$ is grown in the center of the gallium arsenide membrane. The quantum dots emit light within a broad spectral range from $\lambda \approx 905\,\mathrm{nm}$ to $\lambda \approx 990\,\mathrm{nm}$. Anderson localization is expected to arise in the high-density of states regime around the vicinity of the mode band edge that is designed to be at $\lambda = 977\,\mathrm{nm}$. The membrane height is 150 nm, the lattice constant is $a = 260\,\mathrm{nm}$, the radius of the holes is $r = 78\,\mathrm{nm}$, and the samples have a length of $L = 100\,\mu\mathrm{m}$. As for the passive waveguides, the disorder is induced by varying randomly the hole positions in the first three rows above and be-

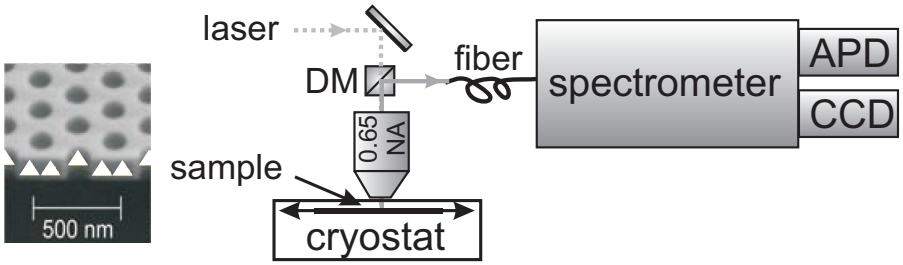

Figure 6.1: Experimental scheme to probe Anderson localization with quantum emitters. A laser (dashed gray line) is focussed onto a disordered photonic crystal waveguide under cryogenic conditions. Thereby, a layer of quantum dots is excited in a diffraction limited region around the waveguide. The quantum dots are illustrated by white triangles in the scanning electron microscope image of the photonic crystal waveguide membrane (left panel). The quantum dot photoluminescence (solid gray line) is recorded using a confocal microscope setup with a dichroic mirror (DM), spatially filtered with a fiber, and spectrally filtered with a spectrometer. The signal can be either recorded with a charged-coupled device camera (CCD) or with a avalanche photo detector (APD).

low the waveguide with a standard deviation of $\delta = 0, 1, \ldots, 6\,\%$ relative to the ideal lattice. The photonic crystal waveguides are placed in a Helium flow cryostat and cooled down to a temperature of $T = 10\,\mathrm{K}$. Light merging from a continuous wave Ti:Sapphire laser ($\lambda = 850\,\mathrm{nm}$) is focussed through a microscope objective (NA = 0.65) onto the photonic crystal waveguide exciting locally the embedded quantum dots above saturation. The emitted light from the quantum dots radiated out-of-the photonic structure is collected through the same microscope objective and separated from the reflected excitation light using a dichroic mirror. Afterwards the photoluminescence is spatially filtered restricting the collecting spot to a small region around the waveguide with a diameter of $1.4\,\mu\mathrm{m}$. The intensity is spectrally filtered with a spectrometer (spectral resolution 50 pm) and recorded with a charged-coupled device camera or a single photon detector, respectively. The sample position is controlled with nano-stages to change the excitation position along the waveguide (spatial scan resolution of $0.3\,\mu\mathrm{m}$). Further details of the experimental setup can be found in Ref. [105].

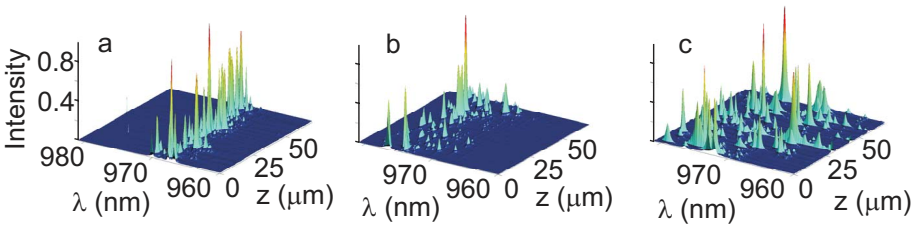

Figure 6.2: Measured intensity that is emitted from the quantum dots, while scanning along the waveguide for three different amount of disorder induced in the photonic crystal waveguide. From left to right: **a**, $\delta = 1\,\%$, **b**, $\delta = 3\,\%$, **c**, $\delta = 6\,\%$. *The quantum dot photoluminescence in the high-density of states regime exhibits large fluctuations which is a strong indication of a coupling to Anderson-localized modes.*

Fig. 6.2 displays the recorded spectral photoluminescence from quantum dot ensembles, while scanning along a photonic crystal waveguide for different amount of disorder ($\delta = 1, 3, 6\,\%$). In agreement with transmission measurements (Chapter 5), we observe close to the calculated waveguide mode band edge (high-density of states regime) spectrally separated Anderson-localized modes. These confined modes appear at random spectral and spatial positions along the waveguide. The intensity exhibits large fluctuations and varies over three orders of magnitudes as predicted for the localized regime [3]. While the spatial extension of the individual localized modes varies, the average extension is determined by the localization length. The spectral range of the modes is found to be dependent on δ. For a low amount of disorder Anderson-localized modes appear in a spectral region of only $\Delta\lambda = 5\,\text{nm}$. On the contrary, strong intensity fluctuations are observed within $\Delta\lambda = 15\,\text{nm}$ for $\delta = 6\,\%$. This might be explained by a disorder dependent breakdown of the dispersion relation.

6.2.2 Probing Anderson localization via intensity fluctuations

A well-established method to investigate Anderson localization is to study the normalized fluctuations in the sample transmittance for many different real-

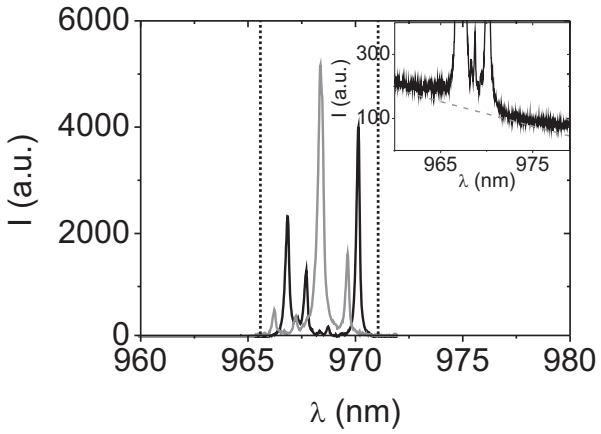

Figure 6.3: Spectral signatures of Anderson-localized modes. Photoluminescence spectra of two different spatial positions (black and gray, $\delta = 1\,\%$). Several Anderson-localized modes appear at each spatial position and are found to be spectrally well-separated. The entire spatial range consists of 350 recorded spectra. The vertical black dashed lines represent the lower and upper limit (λ_{min} and λ_{max}) where the intensity fluctuations occur. The inset shows the recorded raw data with pronounced background light originating from the light emission of the quantum dots that do not couple to the photonic crystal waveguide mode. The dashed line in the inset is a linear fit to the data.

izations of disorder [109]. The corresponding total transmission distribution changes significantly as the localized regime is approached (cf. Fig. 4.5 in Chapter 4). Instead of measuring the transmission, we study in the present experiment the normalized fluctuations and distributions of the quantum dot photoluminescence. Since the localization length is strongly dispersive, the analysis is restricted to the narrow spectral region where Anderson-localized modes can be observed. All recorded spectra that belong to a single spatial scan along the waveguide are cropped to the same spectral region, defined by the range of pronounced intensity fluctuations (dashed lines, Fig. 6.3). To account for the inhomogeneous broadened light emission of the quantum dots, we fit the spectra with a linear function and subtract it from the signal (inset Fig. 6.3).

Once the spectra a preprocessed, the photoluminescence probability distribution can be extracted, as presented in Fig. 6.4a, b. The intensity probability distribution $P(I/\langle I\rangle)$ is obtained by measuring the wavelength dependent intensities $I_{\lambda,z}$ at all spatial positions z. For each position the spectrally ensemble-averaged intensity $\langle I_z\rangle$ is calculated. In very good agreement to our calculations, the individual distributions $P(I_{\lambda,z}/\langle I_z\rangle)$ do not show a pronounced dependence on z. For a better signal to noise ratio we incorporate all measured intensities $I_{\lambda,z}/\langle I_z\rangle$, normalized to their position z. Thus, we get $P(I/\langle I\rangle)$ with $I\epsilon\{I_{\lambda,z}/\langle I_z\rangle\,|\lambda_{\min}\leq\lambda\leq\lambda_{\max}, 0\leq z\leq L\}$.

The fluctuations in the emitted light intensity provide an important statistical property characterizing Anderson localization of light. A detailed study of the measured intensity distributions are displayed in Fig. 6.4 for two different degrees of disorder. The recorded intensity probability distributions (Fig. 6.4) display large fluctuations that are more than 20 times above and 10 times below the average intensity, respectively. Under high excitation powers the emission rates of the excited QDs are strongly influenced by the local density of states of the photonic crystal waveguide, resulting in a so-called Purcell-enhanced photoluminescence intensity [110]. The local density of states at the position of an emitter determines its decay rate by counting the electromagnetic modes projected along the emitter dipole orientation. The experimental data are fitted with the spatially averaged local density of states probability distribution of a lossless disordered medium having the localization length as the only free parameter (red curves in Fig. 6.4). Due to the high density of quantum dots (density $\approx 80\,\mu\mathrm{m}^{-2}$), the diffraction limited excitation spot ($\approx\lambda$) excites an ensemble of quantum dots. In a disordered medium the environment of the emitter normally changes on length scales much smaller than our excitation area and thus our theoretical model resembles the spatial average of the local density of states on the length scale of λ which is also called mesoscopic local density of states [85], as outlined in Chapter 4. The comparison of experiment and theory was performed by calculating the fit goodness, $\chi^2(\xi)$, of the theoretical distribution, $P_T(I/\langle I\rangle)$ and the experimental distribution, $P_E(I/\langle I\rangle)$, depending on the localization length[1]: $\chi^2(\xi)=\sum_{I/\langle I\rangle}\left[|\log(P_T(I/\langle I\rangle))-\log(P_E(I/\langle I\rangle))|^2\right]$ [106]. We are interested in fitting the tail of the distribution and investigate

[1] $\chi^2(\xi)$ is not weighted with the experimental error, that is set to $\Delta P_E(s)=1$. The error might be overestimated resulting in $\chi^2(\xi)<1$.

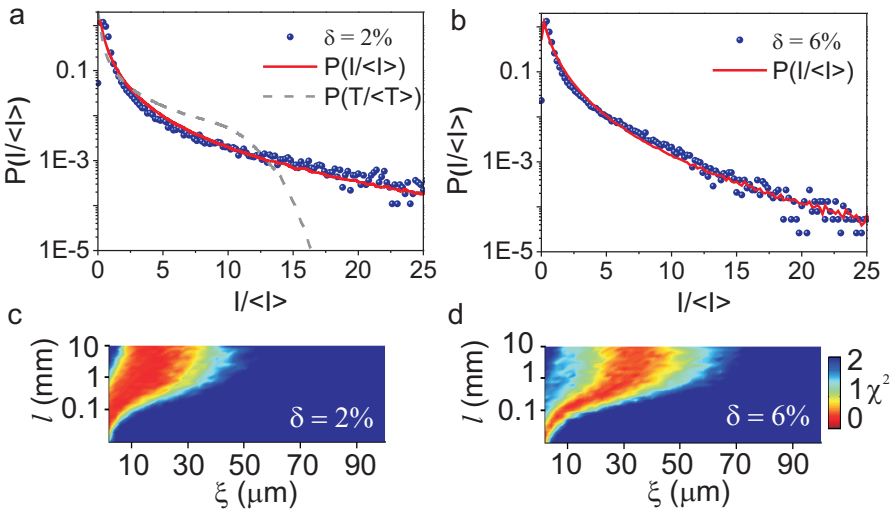

Figure 6.4: Measured intensity probability distribution in the Anderson-localized regime for **a**, $\delta = 2\,\%$ *and* **b**, $\delta = 6\,\%$. *The intensity, I, is normalized to the average intensity, $\langle I \rangle$. The red curves represent the fitted spatially averaged local density of states probability distribution (averaged over λ). The theoretical predictions are obtained from calculations in absence of losses with ξ as the only free parameter (***a**, $\xi = 19\,\mu m$, **b**, $\xi = 23\,\mu m$). *For comparison, the transmission probability distribution is plotted for the same localization length ($\delta = 2\,\%$: gray dashed line with $\xi = 19\,\mu m$). **c**, **d**, Measured fit goodness, χ^2, depending on localization length and loss length. For each pair, (ξ, l), the corresponding spatially averaged local density of states distribution is compared with the experimental data. A lower χ^2 results in a better fit.*

the logarithm of the functions. Remarkably, the long tails of all investigated experimental distributions ($I > \langle I \rangle$) follow the trend of the theoretical predicted spatially averaged local density of states supporting that the photonic crystal waveguide behaves as a 1D system. We would like to underline that an improvement of the fit to the experimental data is expected by employing a full 3D far-field calculation of the photonic crystal waveguide, taking into account the modulation of the light intensity emitted by the QDs embedded in the photonic crystal when radiated out of the structure. Our results reveal the complex interplay between the intensity fluctuations and the local density of

states fluctuations [85] in the Anderson-localized regime. Very recently, local density of states fluctuations have been studied in disordered media and variations of a factor of two have been measured in the the diffusive regime [111, 112]. Our calculations show that the fluctuations are much more pronounced in the localized regime which could possibly open a new route to investigate how the local density of states fluctuations manifest themselves in spatial intensity correlations in the far field [80]. We note that the corresponding transmission distributions do not show an agreement with the experimental data (dashed curve in Fig. 6.4a), highlighting the fundamental difference between our experiments and prior statistical analysis of Anderson localization carried out with light sources positioned outside the disordered medium [17, 3, 23, 82].

Including losses in the calculations, the measure of the fit goodness, $\chi^2(\xi, l)$, can be estimated for different loss and localization lengths, as displayed in Figs. 6.4c and d. It is clearly visible that we obtain a good agreement between theory and experiment over the entire range in l. The emitted intensity probability distributions are therefore not suitable to distinguish between ξ and l (see Chapter 4.3). A fit of the experimental data with the spatially averaged local density of states distribution in a lossless medium shows an increase in the localization length versus δ. A longer localization length results in less fluctuations in the intensity of Anderson-localized modes which reduces the probability to observe very high intensities ($I \gg \langle I \rangle$). This behaviour can be experimentally observed (Figs. 6.4a and b). The corresponding normalized variances in the quantum photoluminescence, $\mathrm{var}(I/\langle I \rangle)$, of all samples are found to be larger than one (Chapter 4.3.1), proving Anderson localization in the disordered photonic crystal waveguides with $\delta = 0, 1, \ldots, 6\,\%$.

6.2.3 Quality factors of Anderson-localized modes

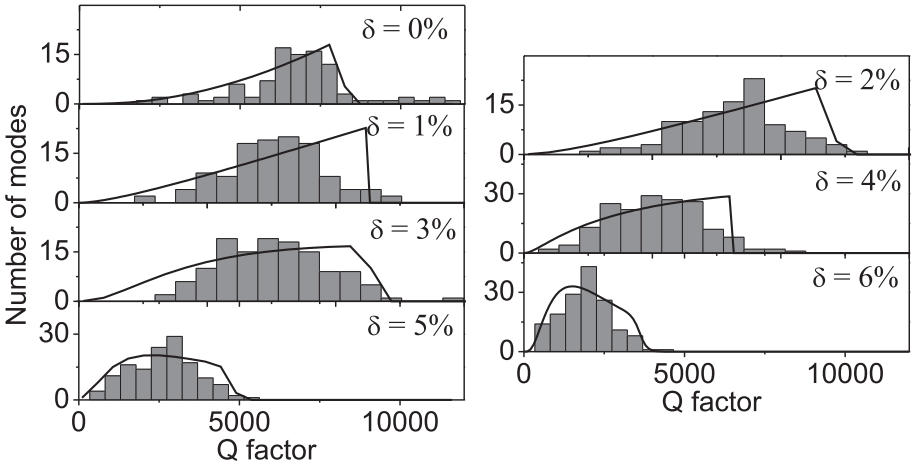

Figure 6.5: Experimental Q factor distributions of the Anderson-localized modes depending on the amount of disorder in the crystal (gray bars). The black curves are calculations and represent the best fit to the experimental data using a one-dimensional model including losses, as presented in Chapter 4.4.

An important parameter of an Anderson-localized mode is the mode quality factor, Q. The Anderson-localized modes appear as peaks in photoluminescence spectrum excited by the (inhomogeneously broadened) quantum dot ensemble. The linewidths of the peaks reflect the mode quality factors in the high excitation power limit [110]. To investigate the individual modes in our samples, the photoluminescence spectra are analyzed along the waveguide (see Fig. 6.2, Appendix E.3). The evaluated Q factor distributions appear very broad and values ranging from $Q = 200$ to $Q = 13,000$ have been measured. The recorded Q factor distributions are shown in Fig. 6.5. We observe a strong dependence of the width and the average value of the distributions on the disorder parameter δ. This feature can be attributed to changes in the localization length and loss length (see below). We highlight that Q factors have been measured ($Q \approx 13,000$) that are comparable to state-of-the-art nano cavities in ordered photonic crystals with embedded quantum dots [92].

The Q factor distribution allows us to determine ξ and l by comparing ex-

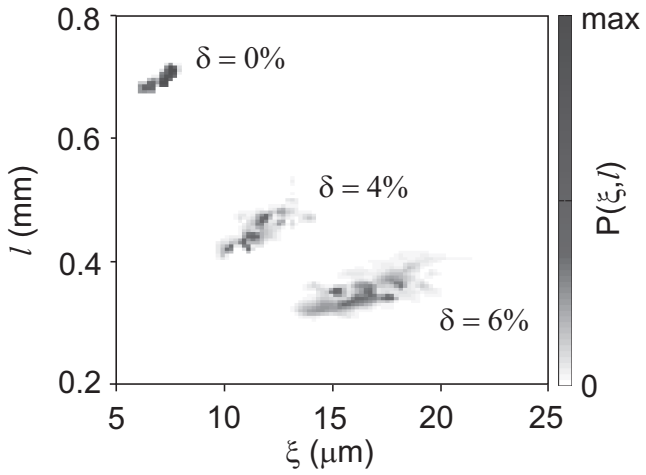

Figure 6.6: Probability, $P(\xi, l)$, that the predicted Q factor distributions (depending on ξ and l) represent the experimental distributions (Fig. 6.5). For visibility we plot the separately calculated probabilities exemplarily for $\delta = 0\,\%$, $\delta = 4\,\%$ and $\delta = 6\,\%$ that is scaled by a factor of two. $P(\xi, l)$ is shown on a linear scale.

periment with theory. In particular, we estimate the probability, $P(\xi, l)$, that a predicted distribution (Chapter 4.4), models the experimental data. For that purpose, we compare the number of observed Anderson-localized modes, N_j, within a specific Q factor range, Q_j, with the theoretical calculations. The size of the Q factor range of bin j is determined by the bin size of the histogram, cf. Fig. 6.5. In accordance with the Bayer's theorem [113], we define the likelihood function, $P(N_1, \ldots, N_{j_{\max}}|\xi, l) = \prod_{j=1}^{j_{\max}} p_j(N_j|N_j^{(T)}(\xi, l))$ conditional on ξ and l. p_j is a Poissonian probability density function. It represents the likelihood that the number of measured Anderson localized modes, N_j, of bin j can be described by a Poissonian distribution having a mean value $N_j^{(T)}(\xi, l)$. Here, $N_j^{(T)}(\xi, l)$ belongs to the calculated probability distribution of bin j for a specific set of (ξ, l). The results of the evaluated probabilities, $P(\xi, l)$, depending on ξ and l, are presented for $\delta = 0\%, 4\%$ and $6\,\%$ in Fig. 6.6. We observe large probabilities only in a very restricted range of ξ and l. Furthermore, the probabilities are found to depend strongly on the disorder induced in the photonic crystal waveguide. This can be explained by the presence of losses

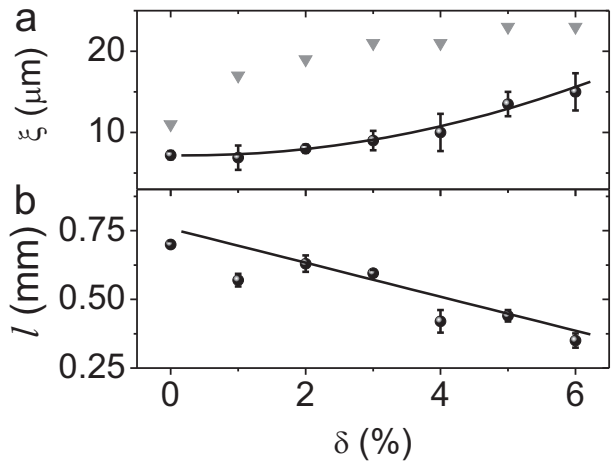

Figure 6.7: Localization lengths and loss lengths in disordered photonic crystal waveguides. **a**, *Estimated localization lengths from the Q factor measurements, plotted as a function of δ (black circles). The gray triangles are determined from the emitted intensity distributions (Fig. 6.4), applying a theoretical model without losses.* **b**, *Estimated loss lengths from Q factor distributions versus disorder. The error bars represent the standard deviation in the probabilities. The black curves are guides-to-the-eye.*

that suppress long scattering paths and thereby truncate the long tails of the Q factor distributions. As a result we obtain very unique distributions. The calculated Q factor distributions corresponding to the largest value of $P(\xi, l)$ are in good agreement with the measurements (solid curves in Fig. 6.5). To confirm the results, a χ^2 - analysis is performed, where all calculated distributions are fitted to the experimental distributions yielding the same ξ and l. These results display that the average value of the Q factor distributions increase and their widths broaden as the localization length shortens and the loss length increases.

Fig. 6.7a displays the localization length as a function of δ. The estimated localization lengths, ranging from $\xi = 6.9 \pm 1.5\,\mu$m ($\delta = 1\,\%$) to $15 \pm 2.3\,\mu$m ($\delta = 1\,\%$), are found to be much smaller than the sample length of $L = 100\,\mu$m, confirming the one-dimensional criterion for Anderson localization. As we vary

δ from 0% to 6%, we observe a significant increase in ξ by a factor of two. We attribute this to a smearing of the local density of states at the waveguide mode band edge [101]. Thus, the group velocity increases and light becomes less sensitive to multiple scattering. This demonstrates a fundamental difference of Anderson localization in slightly disordered periodic structures [25, 108] as compared to entirely random samples where ξ decreases with increasing disorder [17]. Furthermore, we plot the localization lengths estimated from the the measured intensity distributions (Fig. 6.7b, gray triangles). The trend of ξ versus δ is similar to the observed trend from the Q factor distributions supporting the results with an independent method. The estimated localization lengths are not expected to match since the intensity distributions are compared to calculations in a lossless medium. We also observed similar localization lengths in the high density of states regime in disordered photonic crystal waveguides without embedded quantum dots ($\xi \approx 30\,\mu$m, cf. Chapter 5). Our estimated values are slightly lower which might be explained by extra scattering contribution of the quantum dots.

The loss length depending on δ is plotted in Fig. 6.7b (black circles). We find that l exceeds ξ by factors between 30 and 80 and that the loss length is reduced when the disorder increases. Recent simulations predict a change in the loss length l of more than one order of magnitude between $\delta = 0\,\%$ and $\delta = 6\,\%$ considering light scattering out of the disordered photonic crystal membrane [86]. In contrast, we only measure a factor of three, indicating the presence of additional losses that dominate over light leakage for small δ. Such loss contributions could be absorbing surface states at the membrane and reabsorption or scattering from quantum dots. For $\delta = 0\,\%$ the loss length is predicted to be much larger ($l_{\mathrm{theo}} = 5000\,\mu$m). Remarkably, as the disorder increases, we obtain a good agreement with the predicted out-of-plane losses yielding $l_{\mathrm{theo}} < 500\,\mu$m for $\delta = 6\,\%$ (see Appendix E.3.2). The estimated loss lengths are confirmed by transmission measurements on waveguides without embedded emitter where a fit to the measured extinction mean free path yield loss lengths that are of the same size (Chapter 5.2). We find that it is crucial to include losses in our model since we only obtain a poor agreement with the experimental Q factor distributions if losses are neglected.

We want to emphasize that the Q factor distributions are much more robust

against additional experimental fluctuations in the collected photoluminescence and therefore a sensitive probe of Anderson localization of light. For low density of states we found a strong dispersion of the localization length (Chapter 5) which might be also present in the localized regime and is not covered by our calculations. This, however, is experimentally not observed within the investigated spectral region. In particular, we do not find any Q factor dependence on the wavelength and thus, approximate the dispersion-free analytical calculations to the experiment.

6.2.4 Coupling of quantum dots to Anderson-localized modes

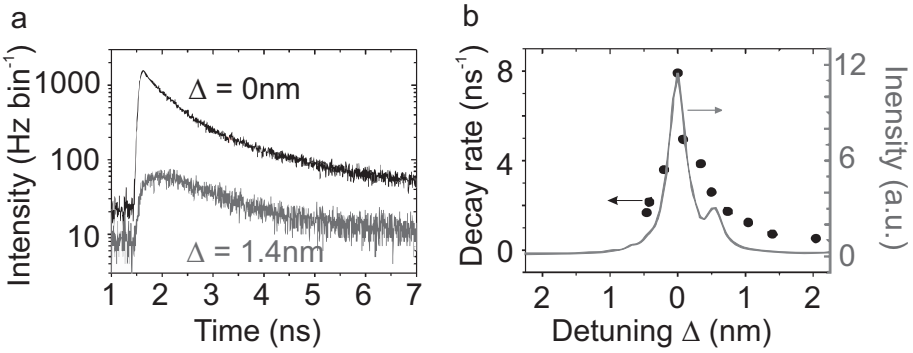

Figure 6.8: Spectral detuning, Δ, of a single quantum dot relative to an Anderson-localized mode. **a**, *Quantum dot decay curves in resonance (black) and out of resonance with the localized mode (gray).* **b**, *Decay rates versus detuning of a single quantum dot (black) and mode emission spectrum (gray) that has been measured by exciting quantum dots ensembles above saturation. These measurements have been carried out by Luca Sapienza and Henri Thyrrestrup.*

Fluctuations in the local density of states can be measured directly via time-resolved photoluminescence spectroscopy. For that purpose we use the same setup, as sketched in Fig. 6.1 and generate picosecond pulses with the Ti:Sapphire laser ($\lambda = 850\,\mathrm{nm}$, pulse length: 2 ps, repetition rate: 75 MHz). A single quantum dot is repeatedly excited below its saturation at a certain

position of the waveguide and the emission time is recorded. Collecting many single-photon events allows us to record a decay curve representing a histogram of detection events versus time. Two examples of decay curves for a single quantum dot tuned on- and off-resonance with an Anderson-localized mode are presented in Fig. 6.8a. We tune the quantum emission frequency relative to the Anderson-localized mode by varying the temperature of the sample. The quantum dot decay rates are extracted by fitting the measured decay curves with several exponential functions. The fastest component extracted from the fit corresponds to the rate of the quantum dot, which is most efficiently coupled to the optical mode and is directly proportional to the local density of states. The slower decay components are due to residual quantum dot recombination processes, e.g., dark excitons. Off resonance, the quantum dot decay rate is inhibited due to the two-dimensional photonic band gap leading to an emission rate of $0.5\,\mathrm{ns}^{-1}$. On resonance, a decay rate of $7.9\,\mathrm{ns}^{-1}$ is measured that originates from the high local density of states created by Anderson localization. Quantum dots that are far detuned from an Anderson-localized mode can couple to the slowly propagating mode of the photonic crystal waveguide [104, 105].

Fig. 6.8b shows the detailed tuning of a single quantum dot through the spectral profile of an Anderson-localized mode. Here, we extract at maximum a 15 fold enhancement in the quantum dot day rate. It proves that the local photonic environment changes significantly over a small spectral range and supports strongly the observed fluctuations in the quantum dot photoluminescence. The enhancement is mainly restricted to the linewidth of the optical mode. This is a further indicator that we can directly probe the local density of states in the Anderson-localized regime with intensity fluctuations emitted from quantum dot ensembles.

6.3 Conclusion and outlook

In conclusion, we probed statistical properties of Anderson localization by placing emitters inside a multiple scattering medium. We observed large fluctuations in the emitted intensity from quantum dots embedded in disordered

photonic crystal waveguides and attributed them to rapid changes in the local density of states in the localized regime. The Q factors of Anderson-localized modes were found to vary over three orders of magnitudes and were used to estimate the localization length and loss length. The Q factor distributions depended strongly on ξ and l, and were controlled by changing the disorder in the structure. All experimental data were found to be consistent with the calculations proving that the investigated waveguides behave as a one-dimensional system in the localized regime. We believe that the results will pave a new route to test fundamental questions in the realm of Anderson localization and form a basis for studies on disorder-induced cavity quantum electrodynamics experiments [91].

A further experiment could be the investigation of a recently proposed type of spatial intensity correlation [114]. B. Shapiro showed that the so-called $C^{(0)}$ correlation function originates from a light source embedded inside a multiple scattering medium and can dominate over all other spatial intensity correlations (see Eq. (2.4)). A scattering process close to the source generates a secondary wave that propagates together with the primary wave along two different directions via a diffusion process. Thus, the far field points are correlated. It has been predicted that the $C^{(0)}$ correlation equals the local density of states fluctuations [80, 115]. So far, $C^{(0)}$ correlations have been studied experimentally inside three-dimensional random media probing individual emission rates of embedded emitters. A promising medium to observe $C^{(0)}$ correlations could be a photonic crystal. While in random powders the measured local density of states fluctuations are rather weak [111], photonic bandgap materials exhibit very strong local density of states fluctuations. We suggest that embedded emitters in two-dimensional photon crystal membranes might be a good candidate to study the $C^{(0)}$ correlation function, in particular in the realm of Anderson localization of light.

Chapter 7

Conclusion

Multiple scattering in the realm of quantum optics enables the investigation of fundamentally new phenomena that cannot be explained classically. This thesis reported on experiments that are of purely quantum origin and are found to be in very good agreement with the developed theoretical predictions. In the second part of this thesis, Anderson localization of light was investigated in disordered photonic crystal waveguides. The localization length, a key parameter to quantify Anderson localization, was probed via the light propagation in transmission-like experiments and via the photoluminescence of quantum dots embedded inside photonic crystal waveguides.

Photon fluctuations are an important property to characterize the quantum state of light. A squeezed light source was established allowing a continuous tuning from a classical to a nonclassical light source. Experimentally recorded photon fluctuations of multiply scattered light proved directly that nonclassical properties of light survive the complex stochastic process of multiple scattering even after ensemble averaging over different realizations of disorder. Quantum noise measurements as well as photon-coincidence measurements revealed spatial quantum correlations that are induced by multiple scattering of light and of purely quantum origin. As predicted by the developed continuous mode quantum theory of multiple scattering, both positive and negative spatial quantum correlations were observed when varying the quantum state of the squeezed

light source. Angular-resolved measurements with single photon counting detectors explored the photon probability distribution of multiply scattered light in the time domain. This method showed that the spatial quantum correlation function is infinite in range and the strength of the correlations can be controlled by the number of the incident photons.

When interference effects survive the statistical ensemble average over all realizations of disorder, the light transport shows deviations from the diffusive regime such as in the coherent backscattering cone. Within this Ph.D. project, the quantum properties of light in the coherent backscattering regime were addressed experimentally. Using a spontaneous down-conversion light source, the backscattering cone was investigated in the few photon regime. Recording the photon probability distributions, the enhancement factor in the photon fluctuations were found to be larger than two which is the classical limit of the intensity enhancement. The presented experiments on spatial quantum correlations and photon fluctuations of multiply scattered light are essential for a fundamental understanding of multiple scattering in the realm of quantum optics and form the basis for new theoretical predictions. Randomly disordered media might open a new route to enhance the information capacity beyond the classical limit. These results depict the multitude of new phenomena encoded in the quantum optical properties of multiply scattered light and might inspire new experiments on, e.g., quantum entanglement of multiply scattered photons.

When multiple scattering becomes very pronounced, light can localize in disordered media. This interference phenomenon was demonstrated in disordered photonic crystal waveguides. Transmission measurements showed that the extinction length is strongly dispersive and can be identified with the localization length in the high-density of states regime of the waveguide mode allowing the control of one-dimensional Anderson localization of light. So far, Anderson localization was probed by placing a light source outside a disordered medium and analyzing the transmission properties. In this thesis an alternative approach was studied by embedding light sources inside a multiple scattering medium in form of quantum dots in disordered photonic crystal waveguides. From the photoluminescence of the quantum dots, the spectral distribution of Anderson-localized modes was determined. The Q factors of Anderson-localized modes resulted in very broad Q factor distributions that were found

to depend strongly on the localization length and loss length. A comparison of the experimental results with analytical calculations of one-dimensional disordered structures determined the localization length and loss length. The losses and the localization length were found to increase as the disorder in the photonic structures increases. All experimental data are found to be consistent with developed analytical calculations proving that the investigated waveguides behaved as a one dimensional system in the localized regime. The results demonstrated a new approach to test fundamental questions in the realm of Anderson localization. Improving the fabrication process might result in photonic crystal waveguides with less imperfections and hence less losses, enabling experiments on disorder-induced cavity quantum electrodynamics in the regime of strong coupling.

Appendix A

Details on the quantum theory of multiple scattering

This appendix provides details to derive the variance in the photon number after multiple scattering of light within the framework of a continuous-mode quantum theory. A light source couples to the input mode a of a multiple scattering medium and the multiply scattered light exits the medium along different directions b_0, b_1. In order to calculate the variance in the transmitted photon fluctuations and the spatial quantum correlations, we need to evaluate the term $\langle \hat{n}_{b_0}(\omega_x)\hat{n}_{b_1}(\omega_y)\rangle$. Using $\langle \hat{n}_{a'\neq a}\rangle = 0 \wedge \langle \hat{n}_b\rangle = 0$ two terms contribute to the result,

$$\begin{aligned}\langle \hat{n}_{b_0}(\omega_x)\hat{n}_{b_1}(\omega_y)\rangle & \\ = \sum_{a',a'',a''',a''''} & t^*_{a'b_0}t_{a''b_0}t^*_{a'''b_1}t_{a''''b_1}\langle \hat{a}^\dagger_{a'}(\omega_x)\hat{a}_{a''}(\omega_x)\hat{a}^\dagger_{a'''}(\omega_y)\hat{a}_{a''''}(\omega_y)\rangle \\ + \sum_{a',b',b'',a''} & t^*_{a'b_0}r_{b'b_0}r^*_{b''b_1}t_{a''b_1}\langle \hat{a}^\dagger_{a'}(\omega_x)\hat{a}_{b'}(\omega_x)\hat{a}^\dagger_{b''}(\omega_y)\hat{a}_{a''}(\omega_y)\rangle.\end{aligned} \tag{A.1}$$

The first non-vanishing term in the last expression is given by

$$\begin{aligned} & \langle \hat{a}^{\dagger}_{a'}(\omega_x)\hat{a}_{a''}(\omega_x)\hat{a}^{\dagger}_{a'''}(\omega_y)\hat{a}_{a''''}(\omega_y)\rangle \\ = \; & \delta_{a',a}\delta_{a'''',a}\Big(\langle \hat{n}(\omega_x)\rangle\delta(\omega_x-\omega_y)\delta_{a'',a'''} \\ & +\left(\langle \hat{n}_a(\omega_x)\hat{n}_a(\omega_y)\rangle - \langle \hat{n}(\omega_x)\rangle\delta(\omega_x-\omega_y)\right)\delta_{a'',a}\delta_{a''',a}\Big), \end{aligned} \tag{A.2}$$

where $\delta(\omega_x-\omega_y)$ describes the result of the continuous-mode commutation relation in the frequency domain. The second non-vanishing term of $\langle \hat{n}_{b_0}(\omega_x)\hat{n}_{b_1}(\omega_y)\rangle$ results in

$$\begin{aligned} & \langle \hat{a}^{\dagger}_{a'}(\omega_x)\hat{a}_{b'}(\omega_x)\hat{a}^{\dagger}_{b''}(\omega_y)\hat{a}_{a''}(\omega_y)\rangle \\ = \; & \langle \hat{a}^{\dagger}_{a'}(\omega_x)\left(\delta(\omega_x-\omega_y)\delta_{b',b''}+\hat{a}^{\dagger}_{b''}(\omega_y)\hat{a}_{b'}(\omega_x)\right)\hat{a}_{a''}(\omega_y)\rangle \\ = \; & \langle \hat{a}^{\dagger}_{a'}(\omega_x)\hat{a}_{a''}(\omega_y)\rangle\delta(\omega_x-\omega_y)\delta_{b',b''}+\langle \hat{a}^{\dagger}_{a'}(\omega_x)\hat{a}^{\dagger}_{b''}(\omega_y)a_{b'}(\omega_x)\hat{a}_{a''}(\omega_y)\rangle \\ = \; & \langle \hat{n}_a(\omega_x)\rangle\delta(\omega_x-\omega_y)\delta_{b',b''}\delta_{a',a}\delta_{a'',a}+\langle \hat{a}^{\dagger}_{a'}(\omega_x)\hat{a}_{a''}(\omega_y)\rangle\langle \hat{a}^{\dagger}_{b''}(\omega_y)a_{b'}(\omega_x)\rangle \\ = \; & \langle \hat{n}_a(\omega_x)\rangle\delta(\omega_x-\omega_y)\delta_{a',a}\delta_{a'',a}\delta_{b',b''}\,. \end{aligned} \tag{A.3}$$

Thus, we get

$$\begin{aligned} & \langle \hat{n}_{b_0}(\omega_x)\hat{n}_{b_1}(\omega_y)\rangle \\ = \; & t^*_{ab_0}t_{ab_1}\langle \hat{n}_a(\omega_y)\rangle\delta(\omega_x-\omega_y)\left(\sum_{a''}t_{a''b_0}t^*_{a''b_1}+\sum_{b'}r_{b'b_0}r^*_{b'b_1}\right) \\ & +|t_{ab_0}|^2|t_{ab_1}|^2\left(\langle \hat{n}_a(\omega_x)\hat{n}_a(\omega_y)\rangle-\langle \hat{n}_a(\omega_x)\rangle\delta(\omega_x-\omega_y)\right) \\ = \; & t^*_{ab_0}t_{ab_1}\langle \hat{n}_a(\omega_x)\rangle\delta(\omega_x-\omega_y)\delta_{b_0,b_1} \\ & +T_{ab_0}T_{ab_1}\left(\langle \hat{n}_a(\omega_x)\hat{n}_a(\omega_y)\rangle-\langle \hat{n}_a(\omega_x)\rangle\delta(\omega_x-\omega_y)\right). \end{aligned} \tag{A.4}$$

The last expression is a very important result since it allows us to calculate the spatial quantum correlation function as well as transmitted and reflected photon fluctuations. The equivalent result using normal ordered operators is $\langle :\hat{n}_{b_0}(\omega_x)\hat{n}_{b_1}(\omega_y):\rangle = T_{ab_0}T_{ab_1}\left(\langle \hat{n}_a(\omega_x)\hat{n}_a(\omega_y)\rangle-\langle \hat{n}_a(\omega_x)\rangle\delta(\omega_x-\omega_y)\right)$. Due the experimental detection scheme, we always measure normal ordered operators.

Next, we want to calculate the variance in the total transmitted photon

fluctuations. In accordance with Eq. (2.16), the variance is given by

$$\begin{aligned}\Delta\tilde{n}_T^2(\omega) &= \int_{\omega-\Delta\omega/2}^{\omega+\Delta\omega/2} d\omega_x \int_{\omega'-\Delta\omega/2}^{\omega'+\Delta\omega/2} d\omega_y \\ &\Big\{ \sum_b \left(\langle \hat{n}_b(\omega_x)\hat{n}_b(\omega_y)\rangle - \langle \hat{n}_b(\omega_x)\rangle\langle \hat{n}_b(\omega_y)\rangle\right) \\ &+ \sum_{b_0}\sum_{b_1\neq b_0} \left(\langle \hat{n}_{b_0}(\omega_x)\hat{n}_{b_1}(\omega_y)\rangle - \langle \hat{n}_{b_0}(\omega_x)\rangle\langle \hat{n}_{b_1}(\omega_y)\rangle\right)\Big\}. \end{aligned} \tag{A.5}$$

The two sums in the last equation can be evaluated separately. The first sum leads to (Eq. (A.4))

$$\begin{aligned}&\sum_b \left[\langle \hat{n}_b(\omega_x)\hat{n}_b(\omega_y)\rangle - \langle \hat{n}_b(\omega_x)\rangle\langle \hat{n}_b(\omega_y)\rangle\right] \\ =\ &\sum_b T_{ab}\langle \hat{n}_a(\omega_x)\rangle\delta(\omega_x-\omega_y) \\ &+ \sum_b T_{ab}^2 \left(\langle \hat{n}_a(\omega_x)\hat{n}_a(\omega_y)\rangle - \langle \hat{n}_a(\omega_x)\rangle\delta(\omega_x-\omega_y) - \langle \hat{n}_a(\omega_x)\rangle\langle \hat{n}_a(\omega_y)\rangle\right). \end{aligned} \tag{A.6}$$

The double sum that originates from the cross correlation in Eq. (A.5) gives

$$\begin{aligned}&\sum_{b_0}\sum_{b_1\neq b_0} \langle \hat{n}_{b_0}(\omega_x)\hat{n}_{b_1}(\omega_y)\rangle - \langle \hat{n}_{b_0}(\omega_x)\rangle\langle \hat{n}_{b_1}(\omega_y)\rangle \\ =\ &\sum_{b_0,b_1\neq b_0} T_{ab_0}T_{ab_1}\Big(\langle \hat{n}_a(\omega_x)\hat{n}_a(\omega_y)\rangle \\ &-\langle \hat{n}_a(\omega_x)\rangle\delta(\omega_x-\omega_y) - \langle \hat{n}_a(\omega_x)\rangle\langle \hat{n}_a(\omega_y)\rangle\Big). \end{aligned} \tag{A.7}$$

In the diffusive regime, the ensemble averaged second order transmission coefficient is given by $\overline{T_{ab_0}T_{ab_1}} \approx (1+\delta_{b_0}b_1)\,(1+4/3g) \approx \overline{T_{ab}}^2$ [15]. Furthermore, the ensemble averaged transmission through each channel can be approximated to be the same, $\overline{T} \approx N \times \overline{T_{ab}}$. As a result we get the ensemble average variance

in the total transmitted photon flux

$$
\begin{aligned}
& \overline{\langle \hat{n}_T(\omega_x)\hat{n}_T(\omega_y)\rangle - \langle \hat{n}_T(\omega_x)\rangle\langle \hat{n}_T(\omega_y)\rangle} \\
= \;& N \times \overline{T_{ab}}\langle \hat{n}_a(\omega_x)\rangle\delta(\omega_x-\omega_y) \\
& + N \times \overline{T_{ab}}^2 \left(\langle \hat{n}_a(\omega_x)\hat{n}_a(\omega_y)\rangle - \langle \hat{n}_a(\omega_x)\rangle\delta(\omega_x-\omega_y) - \langle \hat{n}_a(\omega_x)\rangle\langle \hat{n}_a(\omega_y)\rangle\right) \\
& + (N^2-N) \times \overline{T_{ab_0}T_{ab_1}} \\
& \times \Big(\langle \hat{n}_a(\omega_x)\hat{n}_a(\omega_y)\rangle - \langle \hat{n}_a(\omega_x)\rangle\delta(\omega_x-\omega_y) - \langle \hat{n}_a(\omega_x)\rangle^2\Big) \\
= \;& \overline{T}\langle \hat{n}_a(\omega_x)\rangle\delta(\omega_x-\omega_y) \\
& + \overline{T}^2 \left(\langle \hat{n}_a(\omega_x)\hat{n}_a(\omega_y)\rangle - \langle \hat{n}_a(\omega_x)\rangle\delta(\omega_x-\omega_y) - \langle \hat{n}_a(\omega_x)\rangle\langle \hat{n}_a(\omega_y)\rangle\right) .
\end{aligned}
\tag{A.8}
$$

Using Eq. (A.5) and Eq. (A.8), we can calculate the integrated dimensionless variance in the photon fluctuations in the diffusive regime within the measurement bandwidth $\Delta\omega$

$$
\overline{\Delta\tilde{n}_T^2(\omega)} \;=\; \overline{T}\langle \hat{n}_a(\omega)\rangle + \overline{T}^2\left(\Delta n_a^2(\omega) - \langle \hat{n}_a(\omega)\rangle\right), \tag{A.9}
$$

where the bars denote the ensemble average over all realizations of disorder.

Appendix B

Details on the spatial quantum correlation experiment

The following Appendix reviews details of the squeezed light source (Chapter 2) as well as details of the fabrication of titanium dioxide samples, and the detection efficiency of the setup to measure spatial quantum correlations. Furthermore, the light source is discussed that is used to carry out angular-resolved measurements (Chapter 3.2).

B.1 Nonclassical light source

As a nonclassical resource we use vacuum squeezed light [41] generated through a periodically poled $KTiOPO_4$ (PPKTP) crystal implemented in a bow tie shaped optical parametric amplifier [116, 117], as shown in Fig. B.1. The nonlinear medium is pumped with a continuous wave laser (Diabolo, Innolight) at a wavelength of $\lambda = 532\,\mathrm{nm}$. The spontaneous parametric down-conversion process generates photon pairs that are in resonance with the cavity ($\lambda = 1064\,\mathrm{nm}$).

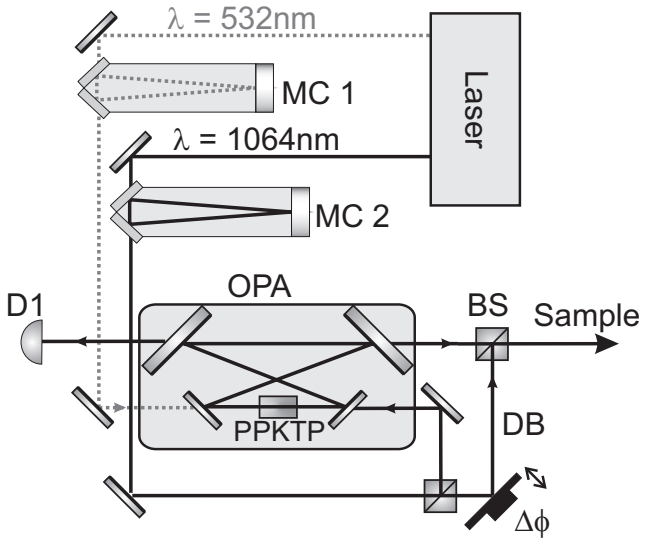

Figure B.1: Scheme of the experimental setup to generate quadrature squeezed light. MC: mode cleaning cavity, OPA: Optical parametric amplifier, PPKTP: periodically poled potassium titanyl phosphate nonlinear crystal, BS: 99:1 beam splitter, DB: displacement beam with a variable optical phase, $\Delta\phi$, relative to the squeezed vacuum, FM: flip mirror, D: photo diode.

The correlation between the photon pairs results in reduced photon fluctuations below the classical limit. A fraction of the cavity mode is coupled out at one mirror of the cavity, called vacuum squeezed light. One of the cavity mirrors is mounted on a pre-loaded mirror holder with a piezo-electric element to adjust the optical path length of the cavity. The optical parametric amplifier is stabilized over several hours with a counter-propagating beam ($\lambda = 1064\,\mathrm{nm}$) using the Pound-Drever-Hall locking technique that controls the piezo-electric element [118]. The first key parameter of the cavity is its Finesse that has to fulfill two requirements. On the one hand, the Finesse should be high to decrease the spectral bandwidth of the down-conversion process and to increase the number of round trips of the correlated photon pairs. On the other hand, many correlated photons should be coupled out. A measurement to estimate the Finesse of our cavity is shown in Fig. B.2a. We scan the mirror (mounted on a piezo-electric element) and record the transmission through the cavity on

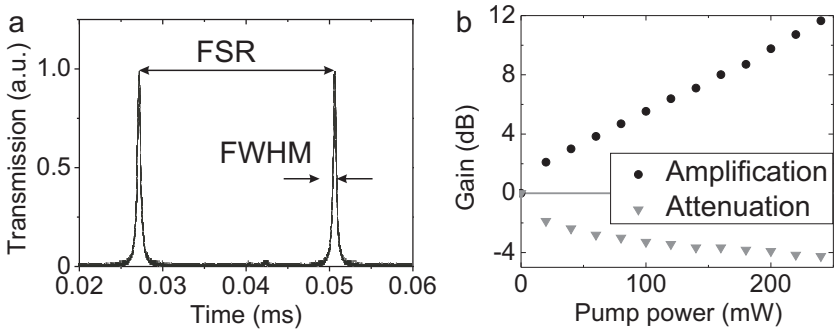

Figure B.2: **a**, *Transmission through the cavity while slowly scanning the optical path length of the cavity. From the full width half maximum (FWHM) and the free spectral range (FSR) the Finesse of the cavity can be calculated.* **b**, *Amplification (black circles) and attenuation (gray triangles) of the electric field inside the optical parametric amplifier depending on the pump power and using a seed laser.*

detector D1. The Finesse yields $\mathfrak{F} = 52$ having a cavity linewidth of 10.5 MHz. A second important parameter is the amplification and attenuation of the electric field in the cavity at $\lambda = 1064\,\text{nm}$ generated by the spontaneous parametric down-conversion depending on the pump power. To amplify or attenuate the cavity field, a laser with $\lambda = 1064\,\text{nm}$ is coupled into the fundamental cavity mode and co-propagates with the pump beam inside the cavity. This seed laser is varied in phase with respect to the pump beam causing a amplification (attenuation) of the electric field in the cavity. An attenuation of $-3.8\,\text{dB}$ is observed determining the maximum vacuum squeezing (Fig. B.2b). Note that the seed beam is blocked when the vacuum squeezed light is generated. Therefore, the seed laser is not included in the setup (Fig. B.1). Further details are discussed in Ref. [119].

The bright squeezed light source is generated by overlapping the vacuum squeezing with a second laser beam ($\lambda = 1064\,\text{nm}$) on a beam splitter. The second laser beam is called displacement beam since its phase $\Delta\phi$ can be varied with respect to the vacuum squeezing. Note that a gaussian mode profile is required to mode match the light beams on the beam splitter. Thus, the pump

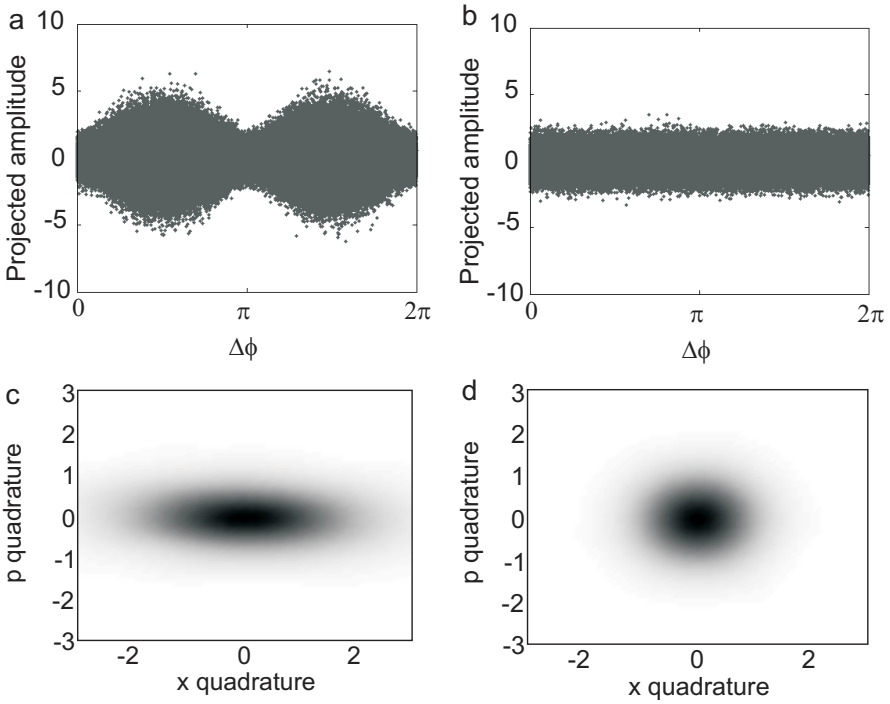

Figure B.3: **a**, *Measured photon fluctuations in the time domain of the quadrature squeezed light source depending on the phase* $\Delta\phi$ *of the bright displacement beam. For comparison the measured photon fluctuations of a coherent displacement beam is plotted in* **b**. *The plots contain approximately 5.5M data points linearly distributed over a phase variation between the signal mode and the displacement beam from 0 to* 2π. **c**, *Corresponding reconstructed Wigner function of the measured quadrature squeezed light source and* **d**, *the coherent beam. The Wigner function is obtained from the time resolved measurements using a homodyne setup.*

laser, lock laser, and displacement beam propagate through a high finesse cavity first, denoted by MC1 and MC2. A further advantage of the mode cleaning cavities is that they suppress any excess noise providing a shot noise limited beam at very low sideband frequencies.

The vacuum squeezed state is characterized by the technique of quantum to-

mography where the Wigner function is reconstructed based on phase-sensitive measurements of the quantum fluctuations in the time domain, see Fig. B.3a. The time resolved signal is down mixed at a frequency of 3.93 MHz and low pass filtered with a bandwidth of 150 kHz. Afterwards the Wigner function is reconstructed using an iterative maximum-likelihood reconstruction algorithm [120]. The Wigner function is a quasi probability distribution that quantifies the fundamental uncertainties in the real and imaginary part of the quantized electric field, which we refer to as x and p, respectively. From Fig. B.3c we observe that the vacuum squeezed state has strongly reduced fluctuations in the x amplitude at the expense of enhanced fluctuations in the p amplitude [121]. The fluctuations of the x amplitude are reduced below the classical limit set by the noise of a coherent state. These nonclassical fluctuations are mapped onto a bright squeezed quantum state containing many photons due to interference of the vacuum squeezed state with light from a laser (displacement beam) on a beam splitter, see Fig. B.1. For comparison, we plot in Figs. B.3b and d the time dependent photon fluctuations and the Wigner function of a coherent light source, respectively. It is clearly visible that the Wigner function does not show reduced fluctuations in the x and p quadrature and the variance in both quadrature is one. In accordance with the Heisenberg uncertainty principle, this represents the classical limit.

B.2 Detector calibration

The multiple scattering sample is illuminated by the squeezed light as explained in the main text. The total transmission (reflection) is detected with a highly sensitive InGaAs-resonance detector (photo diode: ETX 500T, Epitaxx). An electrical spectrum analyzer is used to measure the variance in the photocurrent that is proportional to the photon number fluctuations at the detector resonance frequency of 3.93 MHz. The detector has a bandwidth of 315 kHz as shown in Fig. B.4a. We ensure that the detector has a linear response by measuring the direct (DC) and alternating (AC) voltage of the photodiode (the photo current of the diode is converted into a voltage with a transimpedance amplifier) versus power of the coherent laser beam. Fig. B.4b displays a linear dependence of the DC voltage as function of the laser intensity that is recorded

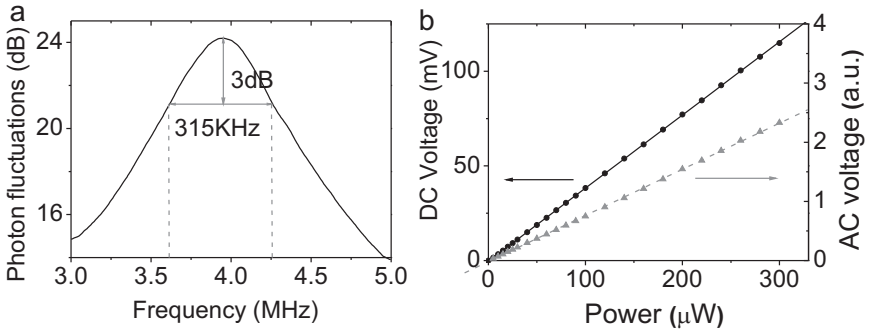

Figure B.4: **a**, *Detector response to a shot noise limited laser that exhibit frequency independent photon fluctuations. The highest sensitivity of the detector is at* 3.9 *MHz. The bandwidth is given by a* 3 *dB decrease in the detector sensitivity and estimated to be* 315 *kHz.* **b**, *DC voltage and AC voltage response of the detector depending on the incident light intensity measured with a voltmeter and a spectrum analyzer at a frequency of* 3.9 *MHz, respectively. The straight lines are a fit to the experimental data.*

independently with a power meter. The alternating voltage represents the variance in the photon fluctuations of the laser beam showing a linear dependence versus laser power, too. This is expected since the intensity of a coherent laser beam scales linear with the variance in the photon fluctuations, i.e., $\langle n \rangle = \Delta n^2$ proving that the laser indeed emits a coherent state and that the detector works in its linear regime. The experiments are performed with optical powers of the light source larger than $P = 5\,\mu$W where signal is 6.5 dB larger than the dark noise level of the detector.

B.3 Fabrication of titanium dioxide samples

The multiple scattering samples are prepared by spreading suspensions of titanium dioxide particles on microscope cover glasses resulting in a typical sample size of 35 mm x 18 mm. A typical scanning electron microscope picture of the sample with nano particles is shown in Fig. B.5a. After evaporation of the liquid, the thicknesses of the samples are measured by scanning each sample using

the tip of a micrometer-screw. The statistics in the thickness determination is obtained by probing 20 different positions on the samples. The central area of each sample is left untouched to avoid damage using this contact technique (Fig. B.5b). We restricted our measurements to a small central area of each sample. Note also that all thickness measurements are carried out far from the sample border where surface tension of the suspension will lead to large variations in the sample thickness. The average thicknesses of the samples are displayed in Fig. B.5c. All samples exhibit a smooth variation in thickness across the sample. The errorbars should therefore be considered as an upper boundary since they are obtained by characterizing inhomogeneities of the whole sample rather than the small area used for optical characterization.

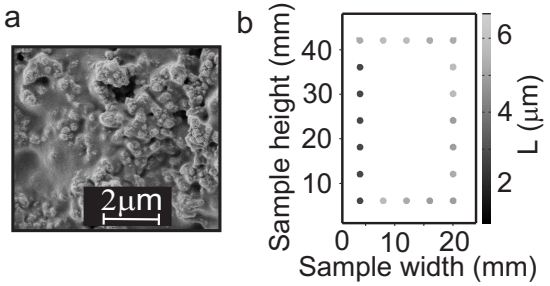

c

Sample	L (μm)	ΔL (μm)
1	5.9	1.8
2	16	4
3	20	5
4	13	3
5	15	3
6	14	3

Figure B.5: **a**, *Scanning electron microscope image of the multiple scattering medium consisting of titanium dioxide that has been grounded into strongly scattering particles with a typical size of* 200 nm. *The samples were fabricated by E. G. van Putten, I. M. Vellekoop, and A. P. Mosk at the University of Twente.* **b**, *Scanning of a sample at different positions with the tip of a micrometer screw to obtain the average sample thickness. A thickness of* $L = (6 \pm 2)\,\mu m$ *is measured for the illustrated sample. c, Overview of the measured thicknesses for all samples that have been used in the experiment.*

B.4 Detection efficiency of the experimental setup

A crucial issue in the estimation of the spatial quantum correlation function is to detect a large amount of transmitted or reflected photons in order to observe any nonclassical effects. In order to compare our experiments to theory an independent measurement of the overall detection efficiency, η, is needed. η is defined as the ratio of the intensity of the multiply scattered light imaged onto the squeezing detector $\overline{I_{\mathrm{det}}}$ relative to the intensity transmitted through the sample $\overline{T} \times I_0$

$$\eta = \frac{\overline{I_{\mathrm{det}}}}{\overline{T} \times I_0}. \tag{B.1}$$

An integrating sphere is used to detect the total sample transmission $\overline{T} = T_{\mathrm{surf}}(\theta)\,\overline{T_{\mathrm{s}}}$ which is the product of surface transmission, for an angle of incidence θ, and the transmission through the multiple scattering medium. $T_{\mathrm{surf}}(\theta)$ describes the interface reflection and can be estimated from the Fresnel relations. Using an effective refractive index of $n = 2.0 \pm 0.4$, as obtained from the total transmission measurements, we get $T_{\mathrm{surf}}(0°) \approx 94\,\%$ after averaging over two independent polarizations and for illumination of the glass side of the sample.

In the reflection geometry, it is desirable to remove direct reflections due to single-scattering events from the multiply scattered distribution of light. To achieve this, the multiple scattering surface of the sample is illuminated under a steep angle of $\theta = 69°$, whereby the direct reflection does not pass through the collection microscope objective. The fraction of the incident light that is multiply scattered into the reflection is therefore $\overline{R} = T_{\mathrm{surf}}(\theta)\overline{R_s}$, where $T_{\mathrm{surf}}(69°) \approx 72\,\%$ is calculated from the Fresnel relations and $\overline{R_s} = 1 - \overline{T_s}$ is obtained from the total transmission measurements with the integrating sphere. The detection efficiency for reflection measurements is given by $\eta = \overline{I_{\mathrm{det}}} / \left(I_0\,\overline{R}\right)$. The measured detection efficiencies for the transmission and reflection experiments are presented in Fig. B.6. It is found to vary with the thickness of the sample since the diffuse light exiting the random medium is collected with different efficiencies depending on the extent of the diffusion process.

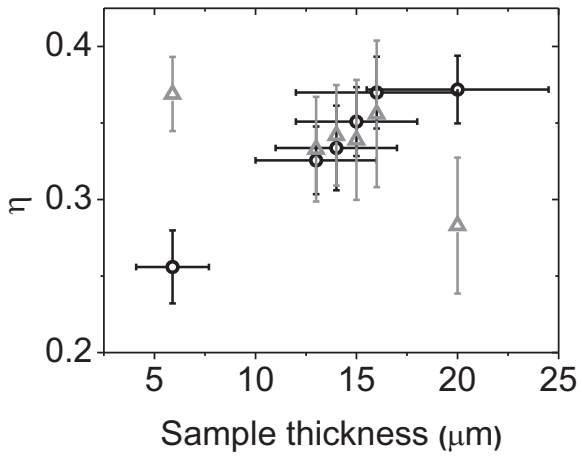

Figure B.6: Separately measured overall detection efficiency η for each sample thickness in transmission (gray triangles) an reflection geometry (black circles). The error bars on the sample thickness are plotted only once.

B.5 Generation of classical photon fluctuations

Chapter. 3.2 discusses the angular-resolved measurement of the spatial photon correlation function. To observe any correlations different from one (uncorrelated photons), it is important that the Fano factor of the light source, $F(\Delta t) = \Delta n^2(\Delta t)/\langle n(\Delta t)^2\rangle$, differs from one. For that purpose a continuous wave Ti:Sapphire laser is used that is focussed onto a slowly rotating ground glass plate (Thorlabs, 600 grit polishes). Afterwards, only a spatial fraction of the light transmitted through the glass plate is collected (cf. Fig. 3.2). The ground glass plate causes large fluctuation in the light transmission scrambling the coherence of the light source. In order to characterize this so-called pseudo thermal light source [58, 59], the number of photons are investigated that arrive within a time interval, Δt, using a single photon counting detector. Repeating the measurement for many time intervals, we find that the number of photons varies between the measurements. A coherent light source with $F(\Delta t) = 1$ shows a Poissonian distribution in the number of detected photons while classical light sources exhibit Super-Poissonian distributions. The mean of the

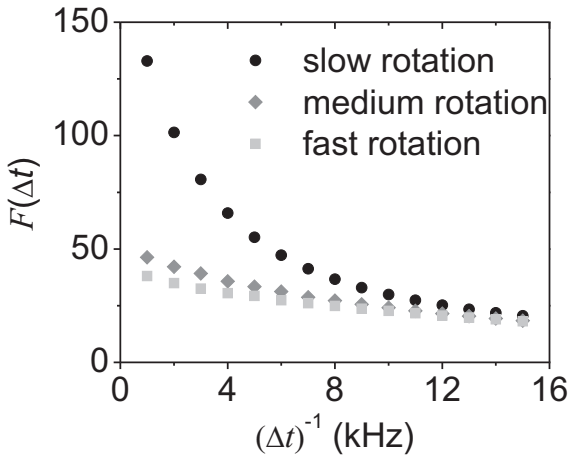

Figure B.7: Measured Fano factor, $F(\Delta t)$, of our classical light source depending on $(\Delta t)^{-1}$. The light source consists of a rotating ground glass plate that is positioned inside a coherent laser beam. $F(t)_{\Delta t}$ is plotted for different rotation speeds of the ground glass plate.

distribution equals $\langle n(\Delta t)\rangle$ and its variance is defined by $\Delta n^2(\Delta t)$. Fig. B.7 displays the Fano factor depending on $(\Delta t)^{-1}$ showing that the Fano factor increases as Δt decreases. The photon fluctuations can be further tuned by changing the rotation speed of the ground glass plate. Slower rotations cause larger fluctuations in the light intensity between different time intervals while a fast rotation leads to intensity fluctuations within Δt. In the experiment, the rotation speed is kept constant and Δt is varied to change the Fano factor.

Appendix C

Details on the coherent backscattering experiment

C.1 Type-II parametric down-conversion light source

An experimental realization of entangled photons has been carried out by P. G. Kwiat et al in 1995 [68] using two overlapping rings of correlated photon pairs that are generated by a non-linear beta-barium borate (BBO) crystal. The polarization of the photons emitted in the different rings is orthogonal to each other and at the intersection of the rings the photons are inherently entangled. This light source is called type-II spontaneous parametric down-conversion (SPDC) source and differs from a type-I SPDC source that generates photon pairs with the same polarization. The underlying physical principle is the spontaneous down-conversion process where a single photon generates two orthogonal polarized photons of lower energy emerging in an ordinary ray and extraordinary ray, respectively. We note that a squeezed light source as it has been described in Appendix B.1 is based on the type-I SPDC process.

Fig. C.1a shows the experimental setup to establish a SPDC source. In

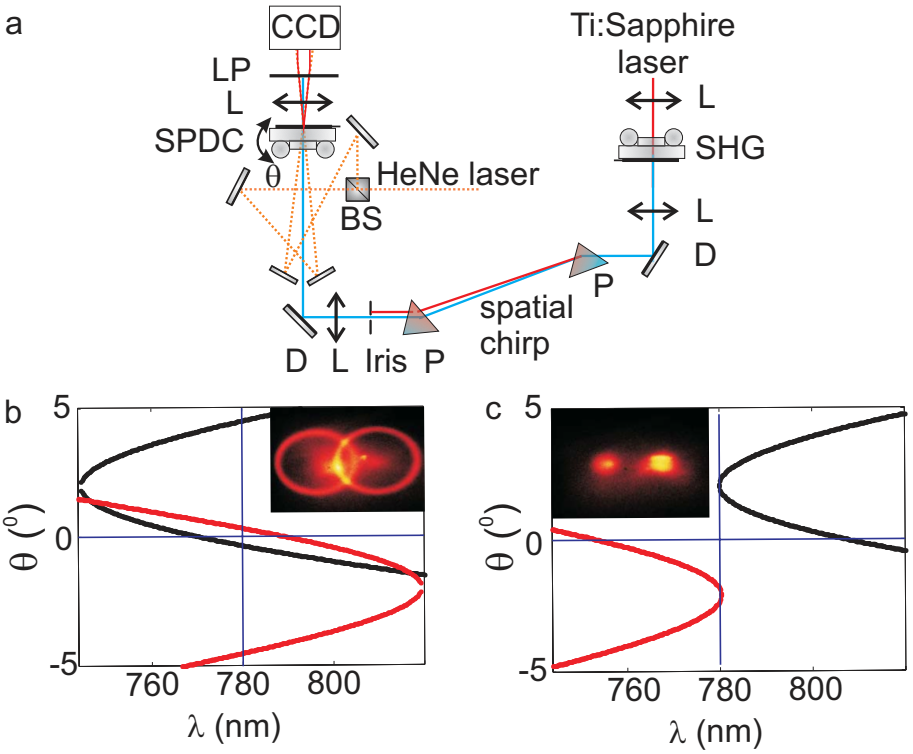

Figure C.1: **a**, *Scheme of the experimental setup to generate photons in a spontaneous parametric down-conversion process. BS: beam splitter, D: dichroic mirror L: lens, LP: long pass 550 nm P: prism, SHG: second harmonic generation.* **b**, *Calculated tuning curves for a type-II SPDC using a pump wavelength of $\lambda = 390\,nm$. The black curve indicates the idler beam the red curve indicated the signal beam. The angle between optical axis of the crystal and pump beam ($\theta = 43.9°$) results in two rings of emitted photons illustrated by four intersections at $\lambda = 780nm$. Inset: Recorded photon rings with the CCD camera around $\lambda = 780\,nm$. The opening angle of the rings is $\Delta\alpha = 4.9°$.* **c**, *Calculated tuning curves for beamlike type-II SPDC using a pump wavelength of $\lambda = 390\,nm$. Inset: Recorded collinear photon beams with the CCD camera that originate from the SPDC source around $\lambda = 780\,nm$. The angle between optical axis of the crystal and pump beam is $\theta = 42.7°$. The angle between the collinear beams is $\Delta\alpha = 4.2°$.*

the first ultraviolet light is generated: A femto-second Ti:Sappire laser ($\lambda = 780\,\text{nm}$, repetition rate 80 MHz) is focussed on a type-I BBO crystal (Ekspla) plate to generate photons at 390 nm in the second harmonic process. The polarization of the generated photons is vertical with respect to the optical board and orthogonal to the incident photons. The power of the Ti:Sappire laser can be continuously varied with a polarizing beam splitter and a $\lambda/2$-wave plate. To avoid any stray light, the co-propagating light of the Ti:Sapphire laser has to be filtered out with dichroic mirrors. In addition, two dispersive prisms separate spatially light beams of different wavelengths. The remaining near infrared light is blocked with an iris. In the second part of the experiment, the SPDC source is realized: The ultraviolet light is weakly focussed (focal length 300 mm) onto another type-II BBO-crystal (United-Crystal) with an anti-reflection coating on both sides and dimensions of $6 \times 6 \times 2\,\text{mm}$ (width $\times$ height $\times$ thickness). The optical axis of the second crystal is aligned to be parallel to the optical board and exhibit an angle of 45° to the front surface of the crystal. Changing the angle θ between the incident pump beam and the optical axis by rotating the crystal results in a different phase-matching condition in the parametric down-conversion process.

To investigate the spatial emission pattern of the down-converted photons depending on θ, the tuning curves are calculated that fulfill the phase-matching condition [122]

$$\begin{aligned} \omega_p &= \omega_s + \omega_i, \\ \vec{k_p} &= \vec{k_s} + \vec{k_i}. \end{aligned} \tag{C.1}$$

Here, ω defines the angular frequency, $\vec{k}$ the wave vector, and the subscripts represent the ultraviolet pump photon, p, and the down-converted near infrared signal, s, and idler, i, photon with ordinary and extraordinary polarization. Fig. C.1b shows the so-called tuning curves that plot the signal and idler wavelength and the corresponding emission angle α between pump photon and the photon pair. The degenerated case $\omega_s = \omega_i = \omega_p$ is very important since it required to create entangled photons (vertical line at 780 nm in Fig. C.1b). The horizontal line represents the emission angle $\alpha = 0°$ when the emitted photons co-propagate with the pump photon. From the Figure we can see that the idler photon and the signal photon both exhibit two solutions at $\lambda = 780\,\text{nm}$ to fulfill Eq. (C.1). This solutions corresponds to two overlapping circles of

idler and signal beams. We verify experimentally the calculations by aligning the BBO crystal to an angle of $\theta = 43.9°$ and placing a highly sensitive EM-CCD camera behind the crystal. The inset in Fig. C.1b shows the recorded rings of the down-converted photons. The agreement between theory and the measured emission angle α is very good. At the intersection of the two rings, the photons are entangled to each other. A drawback of this configuration is that only a small fraction of the emitted photon pairs can actually be used in an entanglement experiment. Decreasing the angle between pump beam and optical axis leads to a change in the phase-matching condition, i.e., the tuning curves move away from each other. Fig. C.1c illustrates a special case where the two tuning curves are tangent to each other. For the degenerated case only one solution fulfills Eq. (C.1) and the photon pairs are emitted in a twin-beam configuration [69, 70]. The divergence of the beams is less than 1° (calculated 0.3°) which allows us to obtain a high collection efficiency of the signal and the idler photons. The inset of Fig. C.1c plots the the experimental measurement of the twin-beam configuration being in good agreement to the predictions. These beams could be overlapped on a beam splitter to create entangled photon pairs [70]. The efficiency of the down-conversion process is extremely low (typically 10^{-10}). A Helium-Neon (HeNe) laser is used to align the experimental setups by overlapping it with the signal and idler beam as shown in Fig. C.1a [123].

C.1.1 Characterization of the light source

For a detailed analysis of our SPDC light source two single photon counting detectors (Perkin Elmer, SPCM/AQRH/13) are placed at a distance of 100 cm behind the nonlinear crystal (inset, Fig. C.2a). A histogram of the recorded coincidence counts depending on the time delay between both detectors is displayed in Fig. C.2a. The plot shows a pulsed spectrum with a pulse period of 14 ns that originates from the repetition rate of the laser. Each time the Ti:Sappire laser sends out a pulse, photons are created in the SHG process. Down-converted photons can be created spontaneously. In an ideal system coincidence events are only expected at $\tau = 0$ time-delay. We detect uncorrelated photon coincidences from different laser pulses that originates from a limited detection efficiency of the detectors. The background counts have to be subtracted to extract the correct number of detected correlated photon pairs. To

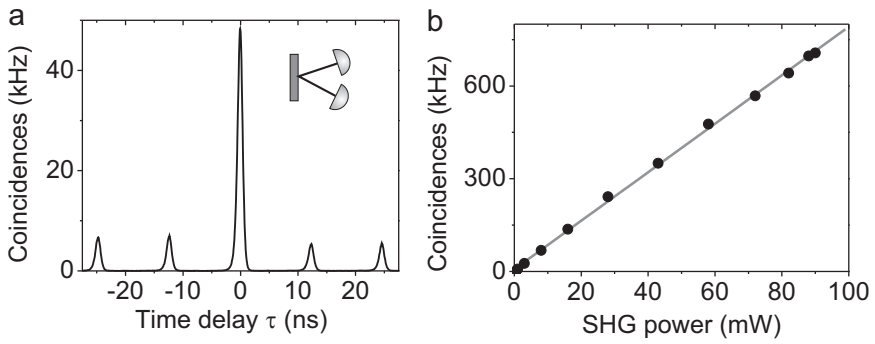

Figure C.2: Characterization of the established twin-beam SPDC source. **a**, *Histogram of detected coincidences between signal and idler beam. The coincidence events at zero time delay originate from the correlated photon pairs that are generated simultaneously. Inset: Experimental setup to measure the coincidences using two single photon counting detectors positioned behind the crystal in the twin-beam rays. Two interference filter are positioned in front of the detectors* $\lambda = 780 \pm 10\,nm$. **b**, *Number of photons created in the down-conversion process as function of the optical power of the pump light. The straight line illustrates the linear dependence of this process indicating that only single photon pairs are created.*

ensure that we only create a single photon pair per laser pulse, we investigate the coincidence counts depending on the pump power of the SHG and observe a linear dependence (Fig. C.2b). A saturation in the signal would indicate that more than one photon pair is generated within the dead time of the single photon detectors. The light source can be potentially used as a triggered single photon source. When an idler photon is recorded and a signal photon is detected simultaneously, it is a single photon because each laser pulse only generates one photon pair [124].

C.2 Angular-resolved photon statistics

In the main text, we described a coherent backscattering experiment in the few photon regime using the parametric down-conversion light source (cf. Chap-

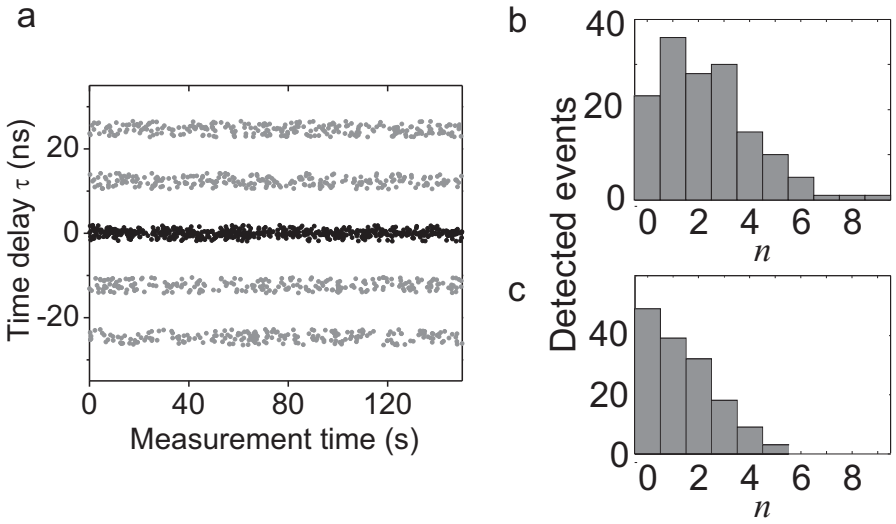

Figure C.3: **a**, *Time-resolved coincidence counts of backscattered photons from a multiple scattering medium for the same polarization as the light source. The backscattering angle is* $\Theta_s = 0°$ *and the angular resolution is* $\Delta\Theta_s = 3.4°$. **b**, *From the time-resolved measurements it is possible to create a photon statistics of the multiply scattered signal photons. The plotted photon statistic is measured for the same polarization as the incident the signal photons. c, Photon statistics recorded under the same conditions as in b but measured in the cross polarization.*

ter 3.3.2). Detector D_1 records the idler photons while the signal photons are directed onto the sample. The backscattered photons are collected in an angular-resolved measurement with a detector D_2. Fig. C.3a displays the recorded photon coincidences between idler and multiply scattered signal photons depending on the total measurement time T. The coincidences at zero time delay mainly originate from correlated photon pairs (black data) plus some additional background coincidence that are also present at non-zero time delays (gray data). In Fig. C.3b the corresponding photon statistic of the backscattered photons is plotted, dividing the total measurement time in time intervals of $\Delta t = 1\,\mathrm{s}$. For each time interval of the measurement time, the number of background-free coincidences is calculated, i.e., the number of coincidences within $\tau = 0 \pm 1.9\,\mathrm{ns}$ minus the average number of coincidences of uncorrelated

photon pairs at non zero time delay. While the light source exhibits a count rate 700 kHz (Fig. C.2b), the average number of photons in Fig. C.3b is 2.75 Hz. Due to the coherent backscattering effect, the backscattered average number of photons for the incident polarization is higher (Fig. C.3b) than for the cross polarization (Fig. C.3c, average count rate: 1.5 Hz).

C.3 Fit to the coherent backscattering cone

We fit the enhanced backscattering cone following the theoretical description presented in Ref. [63]. The incident angle, Θ_i, of the light beam is assumed to be normal to the sample surface, i.e., $\mu_i = \cos\Theta_i = 1$. The line shape of the cone can be calculated for all scattering angles, Θ_s ($\mu_s = \cos\Theta_s$), of the multiply scattered light by superimposing the reflected light that originates from a bell-shaped diffusive background, $\gamma_l(\mu_s)$, and a triangular peak from the constructive interference of counter propagating light paths, $\gamma_e(\mu_s)$ [125]. The latter contribution only arises for multiply scattered light with the same polarization as the incident light. The cross polarization shows a diffusive background which is calculated to be

$$\gamma_l(\mu_s) = 3\mu_s \left(\tau_e + \frac{\mu_s \mu_i}{\mu_s + \mu_i} \right), \tag{C.2}$$

with $\tau_e \equiv z_e/\ell$. The extrapolation length of the sample is defined as z_e and ℓ is the transport mean free path. The triangular peak is given by

$$\gamma_c(\mu_s) = \frac{3(\varepsilon - 1)}{2\,\mu_i\, v} \times \frac{1}{(a+v)^2 + u^2} \times \left(1 + \frac{2\,v\,\tau_e}{1 + \tau_e\, a} \right), \tag{C.3}$$

where we substituted following parameter

$$v \equiv \frac{1}{2}\left(\frac{1}{\mu_s} + \frac{1}{\mu_i} \right), \quad u \equiv k_0\,\ell(\mu_i - \mu_s), \quad a \equiv k_0\,\ell\,|\sin\theta_s|. \tag{C.4}$$

The enhancement factor, ε, describes the backscatter intensity in the exact backscatter direction, ($\Theta_s = 0$), i.e., $\varepsilon \equiv (\gamma_l + \gamma_e)/\gamma_l$. In an ideal system $\varepsilon = 2$ but this value can be reduced due to a limited experimental resolution, absorption, and single scattering events. The total shape of the backscatter cone is defined as $(\gamma_l(\mu_s) + \gamma_e(\mu_s))/\gamma_l(\mu_s)$. The width of the cone describes the scattering strength of the sample and is given by $k_0\ell$.

Appendix D

Local density of states in a one-dimensional medium

D.1 Local density of states in a homogeneous medium

The projected local density of states in direction $\vec{e_z}$ is a classical property of the electromagnetic field and is calculated as the sum over all electromagnetic modes in the system [83]

$$\rho(\omega, r) = \sum_{\vec{k},j} |\vec{e_z} \cdot f_{\vec{k},j}(\vec{r})|^2 \delta(\omega - \omega_{\vec{k},j}). \tag{D.1}$$

The eigenfrequencies are given by $\omega_{\vec{k},j}$. $f_{\vec{k},j}$ denotes the eigenfunctions for the polarization, j, and wave vector, $\vec{k}$, respectively. In one dimension, of concern here, the normalized eigenfunction can be written as

$$f_{k,j}(z) = \frac{e^{ikz}}{n\sqrt{L}} \vec{e}_{k,j}, \tag{D.2}$$

where n is the refractive index and L the system length. The projection is chosen in such a way that one polarization of electric field is orthogonal to

$\vec{e_z}$ and does not contribute to the projected local density of states. Eq. (D.1) can be evaluated by transforming the sum into an integral. For a homogenous medium we get

$$\begin{aligned}\rho(\omega) &= \frac{L}{2\pi}\int_{-\infty}^{\infty} dk\,|\vec{e_z}\cdot\vec{e}_k|^2\left|\frac{e^{ikz}}{n\sqrt{L}}\right|^2\delta(\omega-\omega_k)\\ &= \frac{1}{2\pi\,n^2}\int_{-\infty}^{\infty} d\omega\,\frac{n}{c}|\vec{e_z}\cdot\vec{e}_k|^2\delta(\omega-\omega_k)\\ &= \frac{1}{2\pi\,c\,n}.\end{aligned} \tag{D.3}$$

Here, we used the relation $dk = (n/c)\,d\omega$ and that the wave vector of the electric field in one dimension always points in the same direction as the system extension $\vec{e_z}\cdot\vec{e}_k \equiv 1$. The last result is related to the imaginary part of $G(z_0, z_0, \omega)$ (Eq. (4.11)). Note that for a one-dimensional medium the spontaneous decay rate cannot be derived from Fermi's golden rule [126]. This quantity is only defined in a three-dimensional medium

$$\gamma(\omega) = \frac{2\pi}{\hbar^2}\sum_{k,j}|\vec{e}_{k,j}\cdot\vec{d}(\omega)|^2\frac{\hbar\omega_k}{2\epsilon\epsilon_0 L}\delta(\omega_k-\omega), \tag{D.4}$$

with $\vec{d}$ being the dipole moment.

D.2 Green's function in a disordered medium

Here, we outline the analytical solution of the Greens function in a one-dimensional disordered medium. A possibility to account for all multiple scattering events coherently and self-consistently is to solve the Lippmann-Schwinger equation [83, 84]. A point source is positioned at z_0 in a host layer (layer length L_p) that is embedded between two interfaces to the left and to the right with reflection coefficients r_L and r_R. We have calculated the full

Green's function in the host layer as

$$a_1 = \frac{\exp(i\,\beta\,|z_0 - z|)}{1 - r_L\,r_R\,\exp\left(i\,\beta\,2\,L_p\right)}, \tag{D.5}$$

$$a_2 = \frac{r_R\,\exp\left(i\,\beta\,(2\,L_p - z_0 - z)\right)}{1 - r_L\,r_R\,\exp(i\,\beta\,2\,L_p)}, \tag{D.6}$$

$$a_3 = \frac{r_L\,\exp\left(i\,\beta\,(z_0 + z)\right)}{1 - r_L\,r_R\,\exp(i\,\beta\,2\,L_p)}, \tag{D.7}$$

$$a_4 = \frac{r_L\,r_R\,\exp\left(i\,\beta\,(2\,L_p - |z_0 - z|)\right)}{1 - r_L\,r_R\,\exp(i\,\beta\,2\,L_p)}, \tag{D.8}$$

$$G(z, z_0, \omega) = \frac{i}{2\,\beta} \times (a_1 + a_2 + a_3 + a_4)\,. \tag{D.9}$$

Two of the four terms describe a forward propagating wave and two of the terms describe a backward propagating wave (explained below). The structure of the terms $a_1, \ldots, a_4$ represents a geometric series which can be understood intuitively. Starting from a point source at z_0, a forward propagating wave $\propto \exp(i\,\beta\,|z - z_0|)$ is radiated in both directions. When we calculate the Green's function in the host layer, $G(z, z_0, \omega)$ is given by a sum of waves that are reflected repeatedly from both interfaces of the host layer to z. Here, we discuss $a1$ (Eq. (D.5)) as an example: the wave propagates from z_0 to $z > z_0$ and changes its phase by $|z - z_0|$. The plane wave propagates further to the right interface, is partly reflected back (r_R), propagates to the left interface, is again partly reflected (r_L) and propagates to z. Thereby, it collects an additional optical path phase shift of $2\,L_p$ and it superimposes with its original wave to $\exp(i\,\beta\,|z - z_0|)\,[1 + r_R\,r_L\,\exp(i\,\beta\,2\,L_p)]$. Both waves are continuously reflected at the interfaces as they travel through the layer and we get

$$\begin{aligned} a_1 &= e^{i\,\beta\,|z_0 - z|}\left[1 + r_R\,r_L\,e^{i\,\beta\,2\,L_p} + (r_R\,r_L\,e^{i\,\beta\,2\,L_p})^2 + \ldots\right] \\ &= \frac{e^{i\,\beta\,|z_0 - z|}}{1 - r_L\,r_R\,e^{i\,\beta\,2\,L_p}}. \end{aligned} \tag{D.10}$$

The other terms a_2, a_3, and a_4 can be explained with a similar argumentation. The forward propagating wave to the right side of the structure consist of $A_R = a_1 + a_3$ and the backward propagating wave is $B_R = a_2 + a_4$. To apply the transfer matrix theory to the left side of the host particle, we define $A_L = a_1 + a_2$ and consequently $B_L = a_3 + a_4$ (c.f Chapter 4.2.2).

Fig. D.1b shows the calculated Green's function for a very simple structure, where the reflections at the interfaces causes the irregular pattern. When the

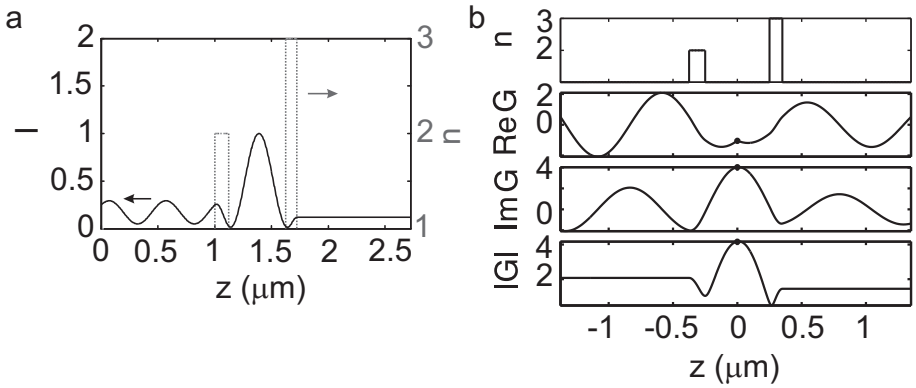

Figure D.1: **a**, *Intensity profile in a structure with varying refractive indices, n, in absence of losses. The light wave is incident from left outside of the medium (at $z = 0$) and the the plotted distribution has been calculated with transfer matrix theory.* **b**, *Spatial refractive index profile, real part, imaginary part, and absolute value of the Green's function, having a point light source inside the structure at $z = 0$ (indicated by the black circle). For visibility is the Green's function scaled by a factor of 10^7.*

light source is placed outside of the structure, the transfer matrix theory can be applied to calculate the intensity distribution as plotted in Fig. D.1a.

Appendix E

Light localization in photonic crystal waveguides

E.1 Fabrication of photonic crystal waveguides

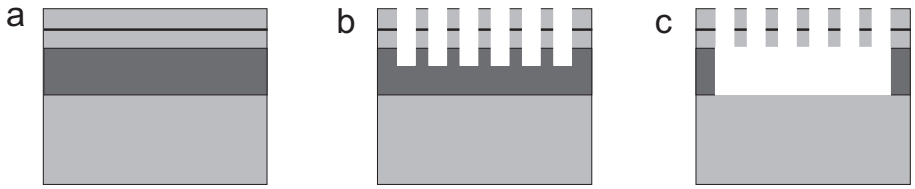

Figure E.1: Scheme of the photonic crystal fabrication. **a**, *unprocessed waver consisting of GaAs (light gray), InGaAs quantum dots (black line), and a AlGaAs stop layer (gray).* **b**, *After electronic beam lithography the dry etching process creates the desired hole pattern. c, In the final process step wet-etching is applied to remove the AlGaAs and to release the membrane. The dimensions are not to scale.*

Two-dimensional photonic crystal membranes have many advantages compared to three-dimensional structures because the fabrication process can be carried out with well-established planar III-V semiconductor technologies. The

samples used in this theses have been fabricated by S. Stobbe and a detailed description can be found in his thesis [127]. Here, a simplified scheme of the process is presented. The unprocessed waver consists of from top to bottom of: 77 nm gallium arsenide (GaAs) followed by a single layer of InGaAs quantum dots (in case of the active structures), and another layer of 77 nm GaAs. The density of the grown quantum dots is approximately $80\,\mu\mathrm{m}^{-2}$. These layers form the membrane and are separated from the GaAs substrate by a stop-layer of $1.6\,\mu$m AlGaAs (see Fig. E.1a). First, the hole pattern is written by electron beam lithography onto the waver. The precision of the hole positions is limited by the electon beam and lies within a few nanometer. Then, dry-etching is applied to the waver to create vertical holes in the waver. The etch-rate ensures that the holes penetrate into the AlGaAs stop layer. Side-wall tilts of the holes are minimized by using a chemical assisted ion beam etching with ions that propagate highly directional. Finally wet-etching removes the AlGaAs stop-layer and releases the membrane.

The final membrane height of the active (passive) photonic crystals is 150 nm (160 nm). The lattice constant is $a = 260\,\mathrm{nm}$ ($a = 240\,\mathrm{nm}$), the hole radius is $r = 78\,\mathrm{nm}$ ($r = 79\,\mathrm{nm}$). We used these values because calculations showed that the corresponding filling fraction yields the largest bandgap. A one-dimensional photonic crystal waveguide is created by leaving out a row of holes during the electronic beam lithography process. The length of the active photonic crystal waveguides is $L = 100\,\mu$m. The passive samples are with $L = 1\,\mathrm{mm}$ very long because we wanted to perform position dependent transmission measurements along the waveguide and an ensemble average of the recorded transmission in different spatial regions of the waveguide. The calculated spectral band edge of the waveguide mode is found to be $\lambda = 977\,\mathrm{nm}$ in the sample with embedded quantum dots and $\lambda = 915\,\mathrm{nm}$ in the sample without the quantum dots containing an error of 5 % due to intrinsic uncertainties in the fabrication parameters.

The scanning electron microscope images in Fig. E.2a-c show photonic crystal waveguides with different amount of disorder by randomly varying the hole positions relative to the ideal lattice for the first three rows below and above the waveguide. The disorder is defined by the standard deviation, δ, of the hole positions relative to the lattice constant, a. For the experiments

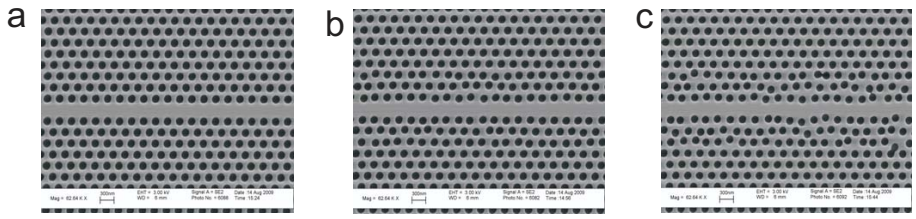

Figure E.2: Scanning electron pictures of photonic crystal waveguides with following disorder parameter **a**, $\delta = 0\,\%$, **b**, $\delta = 6\,\%$, *and* **c**, $\delta = 12\,\%$.

different samples have been fabricated with engineered disorder ranging from $\Delta = 0, 1, \ldots, 6, 9, 12\,\%$. To compare the samples with and without embedded quantum dots the fabrication process was the same.

E.2 Measurement of the out-of-plane scattered intensity

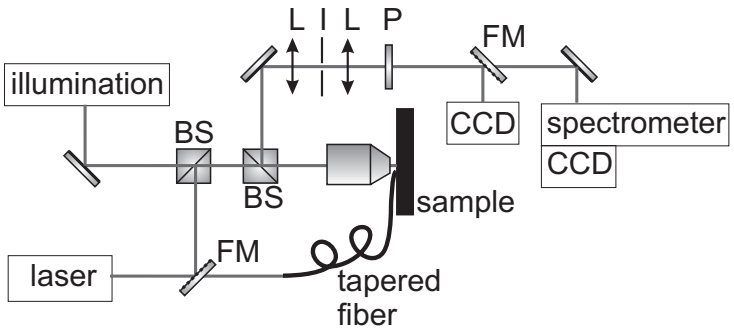

Figure E.3: Experimental setup to measure light transport in photonic crystal waveguides. BS: beam splitter, CCD: charged coupling device camera, FM: flip mirror, spatial filter consisting of two lenses (L) and an iris (I), P: polarizer.

The light propagation in disordered photonic crystal waveguides without embedded quantum dots has been investigated under ambient conditions. An illustration of the experimental setup is shown in Fig. E.3. For alignment purposes the sample can be illuminated with a light bulb and imaged onto a camera

in the detection path. Light can be coupled into the waveguide either from the top or evanescently with a tapered fiber. As a light source we use a tunable continuous wave Ti:Sapphire laser (motorized tuning range $\lambda = 700-1000\,\mathrm{nm}$). We use a microscope objective with a high numerical aperture (NA= 0.8) to collect the out-of-plane scattered light from top of the waveguide. The microscope objective is positioned on a motorized three-dimensional translation stage with a spatial accuracy of 40 nm. This allows us to measure the light transport through the photonic crystal waveguide as function of distance from the fiber tip. A spatial filter in the collection path ensures that we only collect light in a diffraction limited region around the waveguide. The detected light is spectrally filtered with a spectrograph (spectral resolution 0.1 nm) and imaged on a camera. The setup is fully automated, i.e., the excitation wavelength is tuned, the microscope objective is moved and the detected light is spectrally filtered and recorded. Different regions of the photonic crystal waveguide are probed by moving the sample manually with a another three-dimensional translation stage.

As a near field scanning probe to couple light into the waveguide, a tapered fiber has been used. The applied fabrication method for the fiber is called tube-etching [128] and is performed by cleaving a conventional single mode fiber with a design wavelength of 800 nm. Afterwards, the fiber is dipped into hydrofluoric acid for two hours. The cladding around the inner fiber glass core reduces the surface roughness significantly as compared to conventional fiber etching. Fiber tips are achieved with a high reproducibility and diameters of $\approx 500\,\mathrm{nm}$. An alternative method is heating the fiber and pulling it simultaneously, but it turned out that the quality of the tip and its thickness is lower.

E.3 Anderson-localized modes in active photonic crystal waveguides

E.3.1 Spectral analysis

In order to obtain the Q factor distribution of Anderson-localized modes, we embed quantum dot light sources in a disordered photonic crystal waveguide.

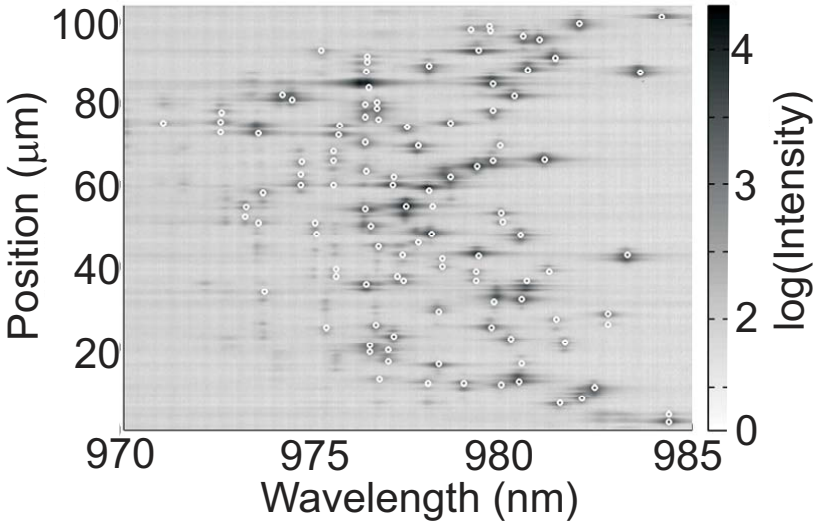

Figure E.4: Spatial and spectral intensity profile recorded from top of a disordered photonic crystal waveguide ($\delta = 2\,\%$). The white circles show the position that have been identified as peaks by the postprocessing algorithm.

Ensembles of the quantum dots are excited well above saturation revealing the spectral distribution of the modes. Fig. E.4 displays the spectra while scanning along the waveguide. The samples have a length of $L = 100\,\mu$m and we recorded 350 equally separated spectra. To account for the spectral resolution of the spectrometer, the spectra are deconvoluted with the measured instrument response function. Afterwards a computer algorithm finds the Anderson-localized peaks in each spectrum and fit them with a multi-Lorentzian fit. From the fit we can calculate the Q factor of each mode. By setting a lower limit on the spectral linewidth ($Q > 200$) and on the intensity of the peak ($I > 0.01\,I_{\mathrm{max}}$) we ensure that no background noise is fitted. I_{max} represents the maximum recorded intensity. Multiply counting of the Q factors of an Anderson-localized mode needs to be avoided since its screws the distribution. We therefore postprocess the analyzed peaks and only count one peak within a certain spectral range over a defined distance. The resulting identified peaks are marked as white circles in Fig. E.4. The Figure reveals another property, a spectral shift of the Anderson-localized modes as the spatial region approaches end facets

of the sample ($z \to 0$, $z \to 100$). It might be be explained by a change in the bandgap center wavelength of the two-dimensional photonic crystal at the ends of the sample. The spatial region for the analysis is limited accordingly ($10\,\mu\text{m} < z < 90\,\mu\text{m}$), when the emitted intensity probability distributions are evaluated.

E.3.2 Predicted out-of-plane losses

In the following the measured loss lengths (Fig. 6.7) are compared with theoretical predictions presented in Ref. [86]. The minimum measured localization length in the disordered photonic crystal waveguide is $\xi = 10\,\mu\text{m}$ and the maximum measured localization length is $\xi = 15\,\mu\text{m}$, respectively. These values correspond to an average back reflection at the elementary unit cell, given by the lattice constant $a = 260\,\text{nm}$, of $\langle R_u \rangle = 0.009$ and $\langle R_u \rangle = 0.005$ (cf. Fig. 4.2b). Furthermore it is important to characterize the disorder in the samples. The perturbations in the hole positions are $\approx 1\,\text{nm}$ for $\delta = 0\,\%$ and $\approx 0.06 \cdot 260\,\text{nm} = 15.6\,\text{nm}$ for $\delta = 6\,\%$. Assuming that a disorder in the hole positions results in similar properties of Anderson localization as changing the hole sizes, the perturbations can be related to the disorder parameter, $\gamma = 1.6$ and $\gamma = 25.2$, respectively (used in Ref. [86]). Thus, the group indices of our disordered photonic crystal waveguide in the investigated spectral region are extrapolated to be $n_\text{g} \approx 80$ for $\delta = 0\%$ and $n_\text{g} < 50$ for $\delta = 6\%$ (cf. Fig. 2a in Ref. [86]). These results can now be applied to give a rough estimation of the out-of plane loss L_u that we identify with our measured loss length $1 - L_u = \exp -a/l$. If no additional disorder is induced in the photonic crystal waveguide, the Bloch mode scattering formalism predicts a loss length $l \approx 5000\,\mu\text{m}$ ($L_u = 5 \cdot 10^{-5}$). On the contrary, for $\delta = 6\,\%$ the loss length decreases but is out of the range in Fig. 2b in Ref. [86]. Here, we only can give an extrapolated upper bound that is $l < 500\,\mu\text{m}$ ($L_u = 5 \cdot 10^{-4}$). Thus, the loss length is predicted to vary over more than one order of magnitude.

Bibliography

[1] P. Barthelemy, J. Bertolotti, & D. S. Wiersma, A Levy flight for light, *Nature* **453**, 495–498 (2008).

[2] I. M. Vellekoop, A. Lagendijk, & A. P. Mosk, Exploiting disorder for perfect focusing, *Nature Photonics* **4**, 320–322 (2010).

[3] A. A. Chabanov, M. Stoytchev, & A. Z. Genack, Statistical signatures of photon localization, *Nature* **404**, 850–853 (2000).

[4] A. Derode, *et al.*, Taking advantage of multiple scattering to communicate with time-reversal antennas, *Phys. Rev. Lett.* **90**, 014301 (2003).

[5] E. Larose, L. Margerin, B. A. van Tiggelen, & M. Campillo, Weak localization of seismic waves, *Phys. Rev. Lett.* **93**, 048501 (2004).

[6] A. L. Moustakas, H. U. Baranger, L. Balents, A. M. Sengupta, & S. H. Simon, Communication through a diffusive medium: coherence and capacity, *Science* **287**, 287 (2000).

[7] M. R. Andrews, P. P. Mitra, & R. deCarvalho, Tripling the capacity of wireless communications using electromagnetic polarization, *Nature* **409**, 316–318 (2001).

[8] H. J. Kimble, The quantum internet, *Nature* **453**, 1023–1030 (2008).

[9] S. Hughes, L. Ramunno, J. F. Young, & J. E. Sipe, Extrinsic optical scattering loss in photonic crystal waveguides: Role of fabrication disorder and photon group velocity, *Phys. Rev. Lett.* **94**, 033903 (2005).

[10] S. I. Bozhevolnyi, V. S. Volkov, & K. Leosson, Localization and waveguiding of surface plasmon polaritons in random nanostructures, *Phys. Rev. Lett.* **89**, 186801 (2002).

[11] C. W. J. Beenakker, Thermal radiation and amplified spontaneous emission from a random medium, *Phys. Rev. Lett.* **81**, 1829–1832 (1998).

[12] P. Lodahl, A. P. Mosk, & A. Lagendijk, Spatial quantum correlations in multiple scattered light, *Phys. Rev. Lett.* **95**, 173901 (2005).

[13] M. Patra & C. W. J. Beenakker, Propagation of squeezed radiation through amplifying or absorbing random media, *Phys. Rev. A* **61**, 063805 (2000).

[14] P. Lodahl, Quantum correlations induced by multiple scattering of quadrature squeezed light, *Optics Express* **14**, 6919–6929 (2006).

[15] M. C. W. van Rossum & T. M. Nieuwenhuizen, Multiple scattering of classical waves: microscopy, mesoscopy, and diffusion, *Rev. Mod. Phys.* **71**, 313–371 (1999).

[16] M. Störzer, P. Gross, C. M. Aegerter, & G. Maret, Observation of the critical regime near Anderson localization of light, *Phys. Rev. Lett.* **96**, 063904 (2006).

[17] D. S. Wiersma, P. Bartolini, A. Lagendijk, & R. Righini, Localization of light in a disordered medium, *Nature* **390**, 671–673 (1997).

[18] D. Bouwmeester, *et al.*, Experimental quantum teleportation, *Nature* **390**, 575–579 (1997).

[19] A. Wallraff, *et al.*, Strong coupling of a single photon to a superconducting qubit using circuit quantum electrodynamics, *Nature* **431**, 162–167 (2004).

[20] Y. Akahane, T. Asano, B.-S. Song, & S. Noda, High-Q photonic nanocavity in a two-dimensional photonic crystal, *Nature* **425**, 944–947 (2003).

[21] P. W. Anderson, Absence of diffusion in certain random lattices, *Phys. Rev.* **109**, 1492–1505 (1958).

[22] T. Schwartz, G. Bartal, S. Fishman, & M. Segev, Transport and Anderson localization in disordered two-dimensional photonic lattices, *Nature* **446**, 52–55 (2007).

[23] H. Hu, A. Strybulevych, J. H. Page, S. E. Skipetrov, & B. A. van Tiggelen, Localization of ultrasound in a three-dimensional elastic network, *Nature Physics* **4**, 945–948 (2008).

[24] J. Billy, *et al.*, Direct observation of Anderson localization of matter waves in a controlled disorder, *Nature* **453**, 891–894 (2008).

[25] S. John, Strong localization of photons in certain disordered dielectric superlattices, *Phys. Rev. Lett.* **58**, 2486–2489 (1987).

[26] F. Scheffold, R. Lenke, R. Tweer, & G. Maret, Localization or classical diffusion of light?, *Nature* **398**, 206–207 (1999).

[27] D. S. Wiersma, J. G. Rivas, P. Bartolini, A. Lagendijk, & R. Righini, Localization or classical diffusion of light? (Reply), *Nature* **398**, 207 (1999).

[28] P. Lodahl & A. Lagendijk, Transport of quantum noise through random media, *Phys. Rev. Lett.* **94**, 153905 (2005).

[29] S. Balog, P. Zakharov, F. Scheffold, & S. E. Skipetrov, Photocount statistics in mesoscopic optics, *Phys. Rev. Lett.* **97**, 103901 (2006).

[30] S. Smolka, A. Huck, U. L. Andersen, A. Lagendijk, & P. Lodahl, Observation of spatial quantum correlations induced by multiple scattering of nonclassical light, *Phys. Rev. Lett.* **102**, 193901 (2009).

[31] W. H. Peeters, J. J. D. Moerman, & M. P. van Exter, Observation of Two-Photon Speckle Patterns, *Phys. Rev. Lett.* **104**, 173601 (2010).

[32] P. Lodahl, Quantum noise frequency correlations of multiply scattered light, *Opt. Lett.* **31**, 110–112 (2006).

[33] S. E. Skipetrov, Quantum theory of dynamic multiple light scattering in fluctuating disordered media, *Phys. Rev. A* **75**, 053808 (2007).

[34] D. J. Durian, Influence of boundary reflection and refraction on diffusive photon transport, *Phys. Rev. E* **50**, 857–866 (1994).

[35] J. X. Zhu, D. J. Pine, & D. A. Weitz, Internal reflection of diffusive light in random media, *Phys. Rev. A* **44**, 3948–3959 (1991).

[36] J. Gómez Rivas, R. Sprik, C. M. Soukoulis, K. Busch, & A. Lagendijk, Optical transmission through strong scattering and highly polydisperse media, *Europhys. Lett.* **48**, 22–28 (1999).

[37] R. Berkovits & S. Feng, Correlations in coherent multiple scattering, *Physics Reports* **238**, 135–172 (1994).

[38] F. Scheffold & G. Maret, Universal conductance fluctuations of light, *Phys. Rev. Lett.* **81**, 5800–5803 (1998).

[39] M. Scully & M. Zubairy, *Quantum optics* (Cambridge University Press, 1997).

[40] H. J. Kimble, M. Dagenais, & L. Mandel, Photon antibunching in resonance fluorescence, *Phys. Rev. Lett.* **39**, 691–695 (1977).

[41] L.-A. Wu, H. J. Kimble, J. L. Hall, & H. Wu, Generation of squeezed states by parametric down conversion, *Phys. Rev. Lett.* **57**, 2520–2523 (1986).

[42] R. Loudon, *The quantum theory of light* (Oxford University Press, 2000).

[43] D. J. Pine, D. A. Weitz, P. M. Chaikin, & E. Herbolzheimer, Diffusing wave spectroscopy, *Phys. Rev. Lett.* **60**, 1134–1137 (1988).

[44] J. Tworzydło & C. W. J. Beenakker, Quantum optical communication rates through an amplifying random medium, *Phys. Rev. Lett.* **89**, 043902 (2002).

[45] R. Lord, *Proc. London Math. Soc.* **3**, 267 (1871).

[46] J. W. Goodman, Some fundamental properties of speckle, *J. Opt. Soc. Am.* **66**, 1145–1150 (1976).

[47] M. Stoytchev & A. Z. Genack, Observations of non-Rayleigh statistics in the approach to photon localization, *Opt. Lett.* **24**, 262–264 (1999).

[48] J. F. de Boer, M. C. W. van Rossum, M. P. van Albada, T. M. Nieuwenhuizen, & A. Lagendijk, Probability distribution of multiple scattered light measured in total transmission, *Phys. Rev. Lett.* **73**, 2567–2570 (1994).

[49] P. A. Lee, Universal conducatance fluctuations in disordered metals, *Physica* **140A**, 169 (1986).

[50] E. Kogan, M. Kaveh, R. Baumgartner, & R. Berkovits, Statistics of waves propagating in a random medium, *Phys. Rev. B* **48**, 9404–9410 (1993).

[51] T. M. Nieuwenhuizen & M. C. W. van Rossum, Intensity distributions of waves transmitted through a multiple scattering medium, *Phys. Rev. Lett.* **74**, 2674–2677 (1995).

[52] O. L. Muskens, *et al.*, Large photonic strength of highly tunable resonant nanowire materials, *Nano Letters* **9**, 930–934 (2009).

[53] Y. Lahini, Y. Bromberg, D. Christodoulides, & Y. Silberberg, Quantum correlations in Anderson localization of indistinguishable particles, *arXiv:1003.3657v1* (2010).

[54] J. R. Ott, N. A. Mortensen, & P. Lodahl, Quantum Interference and Entanglement Induced by Multiple Scattering of Light, *Phys. Rev. Lett.* **105**, 090501 (2010).

[55] R. Hanbury Brown & R. Twiss, Correlation between photons in two coherent beams of light, *Nature* **177**, 27 (1956).

[56] M. P. V. Albada & A. Lagendijk, Observation of weak localization of light in a random medium, *Phys. Rev. Lett.* **55**, 2692–2695 (1985).

[57] P.-E. Wolf & G. Maret, Weak localization and coherent backscattering of photons in disordered media, *Phys. Rev. Lett.* **55**, 2696–2699 (1985).

[58] F. T. Arecchi, Measurement of the statistical distribution of Gaussian and laser sources, *Phys. Rev. Lett.* **15**, 912–916 (1965).

[59] G. Scarcelli, A. Valencia, & Y. Shih, Two-photon interference with thermal light, *Europhys. Lett.* **68**, 618–624 (2004).

[60] O. L. Muskens & A. Lagendijk, Broadband enhanced backscattering spectroscopy of strongly scattering media, *Optics Express* **16** (2008).

[61] O. L. Muskens & A. Lagendijk, Method for broadband spectroscopy of light transport through opaque scattering media, *Opt. Letters* **34**, 395–397 (2009).

[62] A. F. Koenderink, *Emission and transport of light in photonic crystals* (Ph.D. thesis, Universiteit van Amsterdam, The Netherlands, 2003).

[63] E. Akkermans, P. E. Wolf, & R. Maynard, Coherent backscattering of light by disordered media: Analysis of the peak line shape, *Phys. Rev. Lett.* **56**, 1471–1474 (1986).

[64] F. J. Schuurmans, D. Vanmaekelbergh, J. van de Lagemaat, & A. Lagendijk, Strongly photonic macroporous gallium phosphide networks, *Science* **284**, 141–143 (1999).

[65] A. Fedrizzi, T. Herbst, A. Poppe, T. Jennewein, & A. Zeilinger, A wavelength-tunable fiber-coupled source of narrowband entangled photons, *Opt. Express* **15**, 15377–15386 (2007).

[66] C. K. Hong, Z. Y. Ou, & L. Mandel, Measurement of subpicosecond time intervals between two photons by interference, *Phys. Rev. Lett.* **59**, 2044–2046 (1987).

[67] T. Jennewein, C. Simon, G. Weihs, H. Weinfurter, & A. Zeilinger, Quantum cryptography with entangled photons, *Phys. Rev. Lett.* **84**, 4729–4732 (2000).

[68] P. G. Kwiat, *et al.*, New high-intensity source of polarization-entangled photon pairs, *Phys. Rev. Lett.* **75**, 4337–4341 (1995).

[69] S. Takeuchi, Beamlike twin-photon generation by use of type II parametric downconversion, *Opt. Lett.* **26**, 843–845 (2001).

[70] Y.-H. Kim, Quantum interference with beamlike type-II spontaneous parametric down-conversion, *Phys. Rev. A* **68**, 013804 (2003).

[71] C. W. J. Beenakker, J. W. F. Venderbos, & M. P. van Exter, Two-photon speckle as a probe of multi-dimensional entanglement, *Phys. Rev. Lett.* **102**, 193601 (2009).

[72] C. W. J. Beenakker, Random-matrix theory of quantum transport, *Rev. Mod. Phys.* **69**, 731–808 (1997).

[73] H. Schomerus & C. W. J. Beenakker, Search for two-scale localization in disordered wires in a magnetic field, *Phys. Rev. Lett.* **84**, 3927–3929 (2000).

[74] P. Sheng, *Introduction to wave scattering, localization, and mesoscopic phenomena* (Academic Press, 1995).

[75] A. F. Ioffe & A. R. Regel, Non-cristalline, amorphous, and liquid electronic semiconductors, *Prog. Semicond.* **4**, 237 (1960).

[76] A. Z. Genack & A. A. Chabanov, Signatures of photon localization, *Journal of Physics A: Mathematical and General* **38**, 10465 (2005).

[77] L. S. Froufe-Pérez, M. Yépez, P. A. Mello, & J. J. Sáenz, Statistical scattering of waves in disordered waveguides: From microscopic potentials to limiting macroscopic statistics, *Phys. Rev. E* **75**, 031113 (2007).

[78] C.-T. Tai, *Dyadic Green's functions in electromagnetic theory* (IEEE Press, Piscataway, New Jersey,, 1994).

[79] L. Novotny & B. Hecht, *Principles of nano-optics* (Cambridge University Press, Cambridge, 2006).

[80] B. A. van Tiggelen & S. E. Skipetrov, Fluctuations of local density of states and C speckle correlations are equal, *Phys. Rev. E* **73**, 045601 (2006).

[81] D. J. Griffiths, *Introduction to electromagnetics* (Prentice Hall, 1999).

[82] J. Bertolotti, S. Gottardo, D. S. Wiersma, M. Ghulinyan, & L. Pavesi, Optical necklace states in Anderson localized 1D systems, *Phys. Rev. Lett.* **94**, 113903 (2005).

[83] P. T. Kristensen, *Light-matter interaction in nanostructured materials* (Ph.D. thesis, Technical University of Denmark, 2009).

[84] O. J. F. Martin & N. B. Piller, Electromagnetic scattering in polarizable backgrounds, *Phys. Rev. E* **58**, 3909–3915 (1998).

[85] H. Schomerus, M. Titov, P. W. Brouwer, & C. W. J. Beenakker, Microscopic versus mesoscopic local density of states in one-dimensional localization, *Phys. Rev. B* **65**, 121101 (2002).

[86] S. Mazoyer, J. P. Hugonin, & P. Lalanne, Disorder-induced multiple scattering in photonic-crystal waveguides, *Phys. Rev. Lett.* **103**, 063903 (2009).

[87] S. A. van Langen, P. W. Brouwer, & C. W. J. Beenakker, Nonperturbative calculation of the probability distribution of plane-wave transmission through a disordered waveguide, *Phys. Rev. E* **53**, R1344–R1347 (1996).

[88] D. J. Thouless, Maximum metallic resistance in thin wires, *Phys. Rev. Lett.* **39**, 1167–1169 (1977).

[89] F. A. Pinheiro, Statistics of quality factors in three-dimensional disordered magneto-optical systems and its applications to random lasers, *Phys. Rev. A* **78**, 023812 (2008).

[90] M. Weiss, J. A. Méndez-Bermúdez, & T. Kottos, Resonance width distribution for high-dimensional random media, *Phys. Rev. B* **73**, 045103 (2006).

[91] L. Sapienza, *et al.*, Cavity quantum electrodynamics with Anderson-localized modes, *Science* **327**, 352 (2010).

[92] K. Hennessy, *et al.*, Quantum nature of a strongly coupled single quantum dot - cavity system, *Nature* **445**, 896–899 (2007).

[93] S. Zhang, J. Park, V. Milner, & A. Z. Genack, Photon delocalization transition in dimensional crossover in layered media, *Phys. Rev. Lett.* **101**, 183901 (2008).

[94] J. D. Joannopoulos, S. G. Johnson, J. N. Winn, & R. D. Meade, *Photonic crystals: molding the flow of light* (Princton University Press, Princton, 2008).

[95] J. Topolancik, B. Ilic, & F. Vollmer, Experimental observation of strong photon localization in disordered photonic crystal waveguides, *Phys. Rev. Lett.* **99**, 253901 (2007).

[96] M. Patterson, *et al.*, Disorder-induced coherent scattering in slow-light photonic crystal waveguides, *Phys. Rev. Lett.* **102**, 253903 (2009).

[97] N. Le Thomas, *et al.*, Light transport regimes in slow light photonic crystal waveguides, *Phys. Rev. B* **80**, 125332 (2009).

[98] R. J. P. Engelen, D. Mori, T. Baba, & L. Kuipers, Two regimes of slow-light losses revealed by adiabatic reduction of group velocity, *Phys. Rev. Lett.* **101**, 103901 (2008).

[99] L. O'Faolain, *et al.*, Dependence of extrinsic loss on group velocity in photonic crystal waveguides, *Opt. Express* **15**, 13129–13138 (2007).

[100] S. G. Johnson & J. D. Joannopoulos, *MIT Photonic-Bands Package* (http://ab-initio.mit.edu/mpb/, 2010).

[101] J. G. Pedersen, S. Xiao, & N. A. Mortensen, Limits of slow light in photonic crystals, *Phys. Rev. B* **78**, 153101 (2008).

[102] A. García-Martín & J. J. Sáenz, Universal conductance distributions in the crossover between diffusive and localization regimes, *Phys. Rev. Lett.* **87**, 116603 (2001).

[103] R. C. McPhedran, *et al.*, Density of states functions for photonic crystals, *Phys. Rev. E* **69**, 016609 (2004).

[104] V. S. C. Manga Rao & S. Hughes, Single quantum-dot Purcell factor and β factor in a photonic crystal waveguide, *Phys. Rev. B* **75**, 205437 (2007).

[105] T. Lund-Hansen, *et al.*, Experimental realization of highly efficient broadband coupling of single quantum dots to a photonic crystal waveguide, *Phys. Rev. Lett.* **101**, 113903 (2008).

[106] J. R. Taylor, *Error analyis* (University Science Books, Sauslito, California, 1997).

[107] H. Thyrrestrup, L. Sapienza, & P. Lodahl, Extraction of the beta-factor for single quantum dots coupled to a photonic crystal waveguide, *Applied Physics Letters* **96**, 231106 (2010).

[108] C. Conti & A. Fratalocchi, Dynamic light diffusion, three-dimensional Anderson localization and lasing in inverted opals, *Nature Physics* **4**, 794 – 798 (2008).

[109] N. Garcia & A. Z. Genack, Crossover to strong intensity correlation for microwave radiation in random media, *Phys. Rev. Lett.* **63**, 1678–1681 (1989).

[110] B. Gayral & J. M. Gérard, Photoluminescence experiment on quantum dots embedded in a large Purcell-factor microcavity, *Phys. Rev. B* **78**, 235306 (2008).

[111] M. D. Birowosuto, S. E. Skipetrov, W. L. Vos, & A. P. Mosk, Observation of spatial fluctuations of the local density of states in random photonic media, *Phys. Rev. Lett.* **105**, 013904 (2010).

[112] P. V. Ruijgrok, R. Wüest, A. A. Rebane, A. Renn, & V. Sandoghdar, Spontaneous emission of a nanoscopic emitter in a strongly scattering disordered medium, *Optics Express* **18**, 6360–6365 (2010).

[113] P. Gregory, *Bayesian logical data analysis for the physical sciences* (Cambridge University Press, Cambridge, 2005).

[114] B. Shapiro, New type of intensity correlation in random media, *Phys. Rev. Lett.* **83**, 4733–4735 (1999).

[115] A. Mirlin, Statistics of energy levels and eigenfunctions in disordered systems, *Phys. Rep.* **326**, 259 (2000).

[116] S. Suzuki, H. Yonezawa, F. Kannari, M. Sasaki, & A. Furusawa, 7 dB quadrature squeezing at 860 nm with periodically poled KTiOPO4, *Applied Physics Letters* **89**, 061116 (2006).

[117] Y. Takeno, M. Yukawa, H. Yonezawa, & A. Furusawa, Observation of -9 dB quadrature squeezing with improvement of phasestability in homodyne measurement, *Opt. Express* **15**, 4321–4327 (2007).

[118] R. W. P. Drever, *et al.*, Laser phase and frequency stabilization using an optical resonator, *Applied Physics B* **31**, 97 (1983).

[119] A. Huck, *Generation and characterization of non-classical surface-plasmon-polaritons* (Ph.D. thesis, Technical University of Denmark, 2010).

[120] A. I. Lvovsky, Iterative maximum-likelihood reconstruction in quantum homodyne tomography, *Journal of Optics B: Quantum and Semiclassical Optics* **6**, S556 (2004).

[121] C. M. Caves, Quantum-mechanical noise in an interferometer, *Phys. Rev. D* **23**, 1693–1708 (1981).

[122] C. Kurtsiefer, M. Oberparleiter, & H. Weinfurter, Generation of correlated photon pairs in type-II parametric down conversion-revisited, *Journal of Modern Optics* **48**, 1997–2007 (2001).

[123] E. Galvez, *et al.*, Interference with correlated photons: Five quantum mechanics experiments for undergraduates, *Am. J. Phys* **73**, 127–140 (2005).

[124] E. J. Galvez, Qubit quantum mechanics with correlated-photon experiments, *Am. J. Phys.* **78**, 510–519 (2010).

[125] B. Bret, *Multiple light scattering in porous gallium phosphide* (Ph.D. thesis, Universiteit van Amsterdam, The Netherlands, 2005).

[126] J. Johansen, *Decay dynamics of quantum dots in nanophotonic structures* (Ph.D. thesis, Technical University of Denmark, 2008).

[127] S. Stobbe, *Enhancement of light-matter interaction in semiconductor nanostructures* (Ph.D. thesis, Technical University of Denmark, 2009).

[128] R. Stöckle, *et al.*, High-quality near-field optical probes by tube etching, *Applied Physics Letters* **75**, 160–162 (1999).